Morphing study by integrated electroactive actuator-sensors for the optimization of aerodynamic performance

Mateus Carvalho Costa

THÈSE

En vue de l'obtention du

DOCTORAT DE L'UNIVERSITÉ DE TOULOUSE

Délivré par :

Institut National Polytechnique de Toulouse (Toulouse INP)

Discipline ou spécialité :

Génie Electrique

Présentée et soutenue par :

M. MATEUS CARVALHO COSTA

le jeudi 1 juillet 2021

Titre :

Morphing électroactif hybride par la conception d'actionneurs-capteurs intégrés pour l'augmentation des performances aérodynamiques - application aux ailes de l'Airbus A320.

Ecole doctorale :

Génie Electrique, Electronique, Télécommunications (GEETS)

Unité de recherche :

Laboratoire Plasma et Conversion d'Energie (LAPLACE)

Directeurs de Thèse :

M. JEAN FRANCOIS ROUCHON

MME MARIANNA BRAZA

Rapporteurs :

M. LIONEL PETIT, INSA LYON

Membres du jury :

M. YANNICK HOARAU, UNIVERSITE DE STRASBOURG, Président

M. DENIS DARRACQ, AIRBUS FRANCE, Membre

M. FRANK THIELE, TECHNISCHE UNIVERSITAT BERLIN, Membre

M. JEAN FRANCOIS ROUCHON, TOULOUSE INP, Membre

MME HENDA DJERIDI, INP GRENOBLE, Membre

MME MARIANNA BRAZA, CNRS TOULOUSE, Membre

Abstract

For the next 20 years, the quantity of air travelers in the world is expected to rise to almost the double of the current number. This growth is followed by the eminent increase of greenhouse gas emissions linked to climate change. Another obvious consequence is the higher operation cost for airline companies. These factors explain the need for better efficiency for modern aircrafts. Among these studies there is the Smart Morphing and Sensing European Project. The goal of the project is to design a system of electroactive actuators for two different time scales. Shape Memory Alloys (SMA) are used for low-frequency camber control of an A320 wing prototype at reduced scale, developed by LAPLACE, while piezoelectric based actuators are responsible for high frequency vibration of its trailing-edge. The experiments have been carried out in the S4 subsonic wind-tunnel at the IMFT facilities in Toulouse to analyze shear-layer dynamics. TR-PIV results were acquired at Reynolds Number of 700k and 1 million. In addition, lift and unsteady pressure measurements were obtained at different upstream velocities. Spectral analysis were computed to investigate the effects of morphing on vortices manipulation and turbulence reduction.

The present thesis is part of the H2020 N° 723402 SMS- "Smart Morphing and Sensing for aeronautical configurations, `http://www.smartwing.org/SMS/EU` coordinated by Toulouse INP (IMFT). The research carried out in the thesis concerns the Work Package 2 (WP2) of the project regarding the Reduced Scale, "RS" morphing A320 wing prototype. This research has been in strong collaboration with AIRBUS "Emerging Technologies and Concepts Toulouse"- ETCT, Endorser of the SMS project.

Acknowledgements

First of all, I thank my thesis directors Marianna Braza and Jean-François Rouchon for the opportunity to work on such a passionate subject. I am very grateful for all the experiences I have lived during the SMS project. I couldn't forget to mention my PhD colleagues from LAPLACE and IMFT who accompanied me on every work trip and conference including the daily company in the office and coffee breaks. Thanks to them these last years of doctorate have been a real pleasure.

Special thanks to Sébastien Cazin, Moïse Marchal, Frédéric Bergame and Hervé Ayroles from Signaux & Image, the IMFT is lucky to count on such competent professionals. Also to Clément Nadal and Dominique Harribey from LAPLACE who have always been there to help me when I needed.

I must include my dear friends who have always stood by me throughout this journey. Thank you very much for the support, the laughs, and the affection in difficult moments.

Here I ask the jury's permission to send a message to my family in Brazil.

Foi um caminho longo até aqui. A distância é dolorosa para todos nós, mas essa conquista é tão minha quanto de vocês. Muito obrigado por tudo, eu não teria chegado tão longe se não fosse pelos sacrifícios que vocês fizeram. Espero poder continuar retribuindo todos os esforços e deixá-los orgulhosos.

Contents

Chapter 1

State of the art

1.1 Introduction

For a long time, human beings have dreamed of flying. We know the story of Daedalus and his son Icarus from ancient Greece. Condemned to wander in the labyrinth of Crete built by Daedalus himself, the architect made wings from wax, wicker and bird feathers to escape from the island. Technological progress has allowed us to fully deploy flight technology. Later, aviation pioneers were inspired by nature to build the first airplanes, following the example of Daedalus. More than two thousand years after the myth of Icarus, Clément Ader built his famous Éole in 1890, which is considered the first heavier-than-air craft with the capacity to take off. The machine, unlike the wings designed by Daedalus, was inspired by the morphology of bats. Thus, nature always seemed to be the key to this human dream.

Figure 1.1: Clément Ader's Éole. Picture from the Musée des arts et métiers-Cnam/photo Michèle Favareille.

To develop aviation in Europe, the Aéro-Club de France has offered a prize to anyone who manages to build a motorized vehicle capable of making a flight of more than 25 meters in length. This prize was won in 1906 by Alberto Santos-Dumont, a Brazilian inventor who, with his 14-bis aircraft, flew 220 meters at 41.3 km/h and broke three world records in one go. It was the first controlled public flight of a motorized aircraft. He had already won, with an airship, a prize of one hundred thousand francs offered to the first flying machine capable of covering the round trip from Saint-Cloud to the Eiffel Tower in less than 30 minutes in 1901. Such feats were due to a change in design. The flying animal-inspired design was replaced by sturdier structures capable of withstanding greater loads. In the face of this innovation, the bio-inspired aspect was no longer considered essential, but this compromise produced good results. In the United States the famous Wright brothers had already understood this. Their first airplanes, the Flyer I and II, were already showing promising results, but thanks to the revolutionary 3-axis control system, the Flyer III became the most powerful aircraft created at the time. These innovations represented a real leap forward in aircraft development and gave birth to modern aviation.

Currently, the improvement in the performance of commercial aircraft is driven by the high level of competitiveness between manufacturers. Among these studies, bio-inspiration has come back to try to improve the aerody-

namic performance of aircraft wings using new intelligent materials. This is not exclusive to the aeronautics industry: we are seeing a strong trend in robotics for developing mechanisms that simulate the functioning of muscles and even the use of new biomaterials. We are relearning to look at nature in search for solutions to today's challenges.

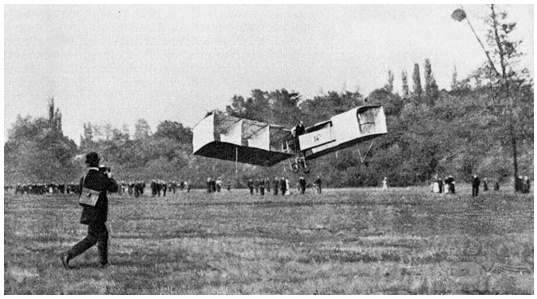

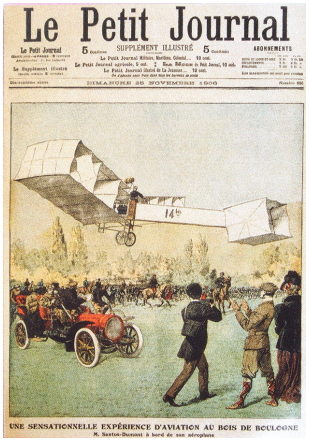

Figure 1.2: The 14-bis first flying over the Château de Bagatelle grounds.

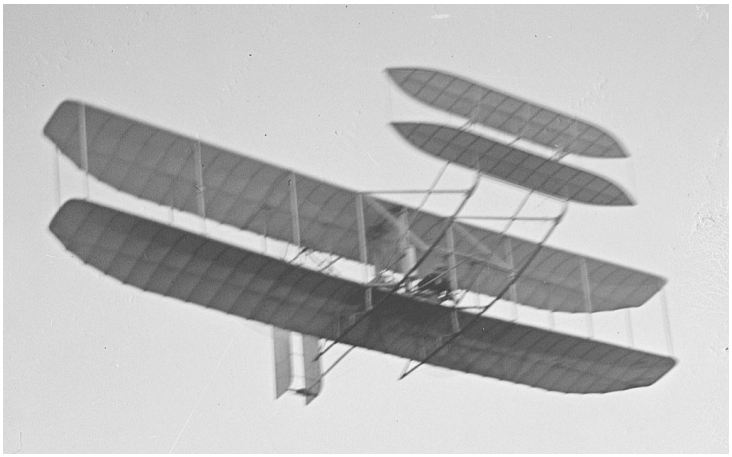

Figure 1.3: The Wright Brothers' Flyer III. Picture from wright-brothers.org.

1.2 Nature & Bio-inspiration

The main inspiration for this project is the nature. Bio inspiration is often confused with bio mimicry. Its aim is not to copy nature, since the scales of force and velocity are not comparable. Also, the presence of an engine provides the horizontal force required to generate lift and balance drag, avoiding the need to flap the wings, which is great. Despite these differences a closer look at the solutions provided over thousands of years of evolution proves itself to be useful. Wind-tunnel experiments have been used to study long flight performance in birds migration [1, 2]. The works of Tobalske [3] and Butler [4] describe how the bio mechanics of birds flight is adapted to reduced energy consumption without giving up on important properties as endurance and maneuverability. Owls, for example, have an unique mechanism to reduce noise during flight [5]. Scientific works have analyzed the flight mechanism of birds and bats with the aim of developing small unmanned drones [6]. For those who are curious, results from Particle Image Velocimetry (PIV) measurements show that birds outperform bats in terms of Lift-to-Drag ratio. Going even further, It has been proven that some species of fish are able to manipulate surrounding turbulence to reduce muscle activity [7]. Also, innovative designs have been created inspired by whales flippers to improve the performance of wing like structures such as fan blades in air turbines [8, 9]. Passive control has also been studied using similar flipper configuration [10]. Salguedeiro [11] provides an interesting review on bio inspired creative designs for enhancement of aerodynamic performances and flow control.

Figure 1.4: Wind-tunnel experiment for respiratory analysis of pigeon flight [4].

The flow dynamics around bluff bodies at moderate to high Reynolds numbers are well known and described in literature [12]. The difference of velocity across two flow interfaces in the wake of the wing result in Kelvin-Helmholtz vortex, also known as shear layer instabilities [13]. This interaction is often seen in flows involving two different fluids and in meteorology as Figure 1.5 shows. The presence of a wing like bodies in a fluid flow also causes vortex shedding. When this phenomenon takes place, coherent structures are created at the back of the body and detach periodically from its sides. This kind of vortex interaction called von Kármán instability generates drag forces due to the formation of low pressure zones in the wake flow [14]. The presence of von Kármán vortex in the wake flow of a wing can be seen in Figure 1.6.

Figure 1.5: Kelvin-Helmholtz vortex seen in clouds.

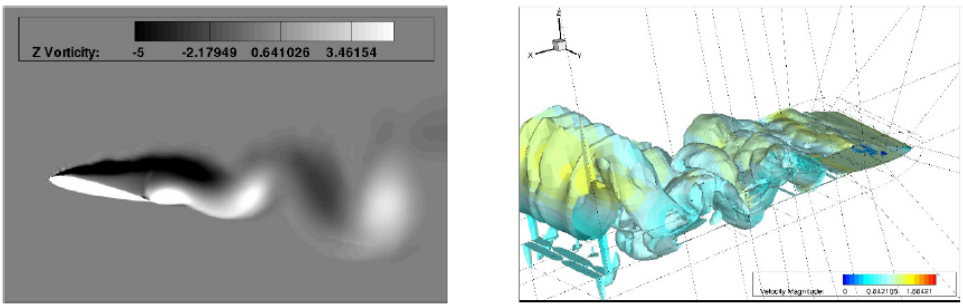

(a) 2D simulation of vorticity.

(b) 3D simulation of velocity magnitude.

Figure 1.6: Visualization of von Kármán instability around a wing by Martinat [15] with AoA = 12°.

Both phenomena described govern the turbulence aspect of the flow around the wings of real commercial airplanes in subsonic regime. The challenge is to combine elements from nature to control or eliminate damaging vortex that generate excessive drag and noise, but the task is not obvious since the flight conditions are far from being the same. Innovative concepts for manufacturing actuators must be employed to overcome this that issue. In association with the company FlexSys, NASA carried out a real flight test with a deformable wing in a test aircraft in 2015. The goal was to reduce fuel consumption by increasing the aerodynamic efficiency of the wing. The principle of such a system is the use of intelligent materials as the basis for the operation of a new generation of actuators.

Different industrial concepts over the last thirty years using different types of on-board systems have focused on improving the shape of aircraft (morphing). In this context, studies carried out within the multidisciplinary team composed of two research institutes in Toulouse, the IMFT and the LAPLACE, have been working since the beginning of 2005 until now to provide electro-actuated systems, allowing the optimization of the shape and vibratory behavior of bearing surfaces thanks to intelligent materials.

1.3 The Smart Morphing and Sensing (SMS) project for aeronautical configurations

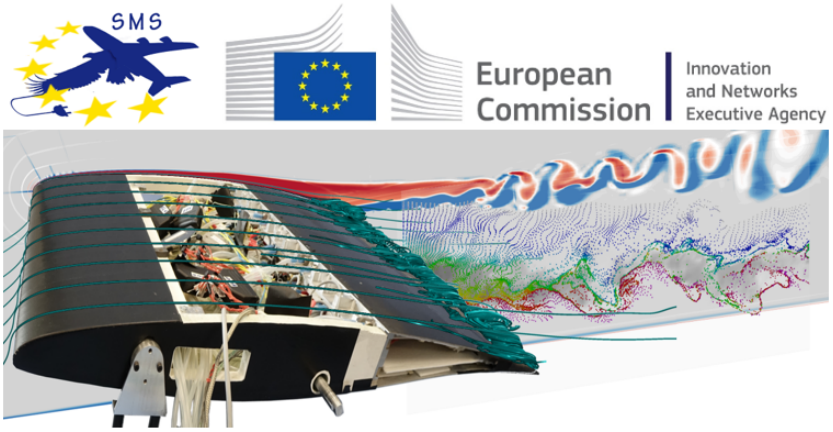

Figure 1.7: SMS European Project.

Aerodynamic studies of advanced concepts have been realized by IMFT over the years thanks to smart actuators designed by LAPLACE in a synergy coupling high fidelity simulations and modeling approaches with the properties of new intelligent electroactive materials. This multidisciplinary team has been supported over the last ten years by four projects and work sites of the STAE Foundation "Sciences and Technologies for Aeronautics and Space", the RTRA "Thematic Network for Advanced Research", by AIRBUS ETCT "Emerging Technologies and Concepts Toulouse" since 2015 and more recently, since 2017, by a federative European project of H2020, N° 723402: SMS - "Smart Morphing and Sensing for aeronautical configurations" coordinated by Toulouse INP by the IMFT-LAPLACE team. The CNRS Journal has dedicated a digital article to the activities of this multidisciplinary team, concerning the design of the bio-inspired wings of the future. The European SMS project is widely exploring innovative aerodynamic concepts capable of increasing performance well above other systems in progress by coupling these concepts with the potential of intelligent materials for the wings of the future. The idea is to modify the shape of aircraft wings and their camber at low frequency, of the order of 1 Hz, using Shape Memory Alloys (SMA) and to achieve higher frequency actuation frequencies (by the order of 500 Hz) but with small deformations of the order of a few millimeters towards the

rear part of the wing (trailing edge), using specific piezoelectric actuators. These facts are inspired by the large camber and simultaneous movements of large predatory birds feathers capable of simultaneously increasing their lift, reducing their wind resistance (drag) and the aerodynamic noise produced by the turbulence surrounding the trailing edge and present in the wake. As a result, with the help of electroactive morphing, we are able to optimize the ratio between lift and drag in relation to the flight phase, in addition to reducing noise. These facts are obtained by manipulating the turbulent vortex structures with the help of dynamic optimization of the wing shape and optimal vibrations generated near the trailing edge to act on the vortex at higher frequencies, as birds' feathers do. The IMFT-LAPLACE team has highlighted the concept of hybrid electroactive morphing and has demonstrated increased aerodynamic performance thanks to this concept. Within the SMS project, 10 European partners have joined together to carry out in synergy a series of experimental, numerical and modeling studies in all phases of flight, in subsonic (takeoff and landing) and transonic (cruise flight) regimes, demonstrating very high performances thanks to electroactive morphing.

Chapter 2

Smart Materials & Actuators

An important innovation of the project is the design of actuators based on smart materials instead of commonly used electromechanical actuators. Among the advantages of electroactive morphing we can mention its great possibilities to realize movements and vibrations of strategic parts of aircraft wings by bio-inspiration and the saving of weight and space dedicated to the integration of actuators while keeping the same performance of conventional systems. "Smart material" is a definition for a large number of metal alloys and ceramics that offers a wide combination of mechanical properties. Figure 2.1 shows an overview of its characteristics. This new technology opens several doors to numerous possibilities and different wing designs have been studied. Liebeck, for example, proposes an innovative design for subsonic airfoils [16]. Barbarino [17, 18] and Weisshaar [19] present an overview of different solutions created over the years.

In this chapter a brief description of the materials used in conception of the actuators is made. Also, a constitutive model for a push-push actuator based on Magnetic Shape Memory alloys (MSMA) is presented. Additionally, the prototype used in the experiments is introduced.

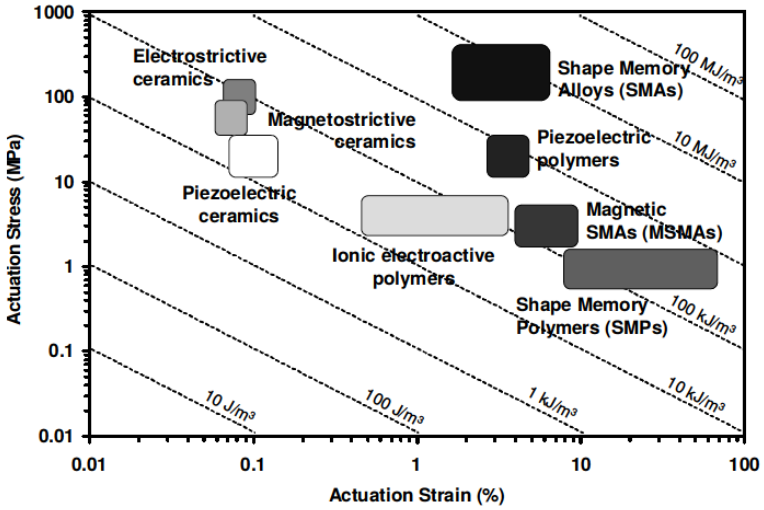

Figure 2.1: Stress x strain diagram for materials often used in actuator design. The transverse curves give us the values of strain energy density [20].

2.1 MSMA actuator

The initial part of this work was dedicated to the feasibility analysis of new smart materials for actuators design. Due to their high frequency aspect, the Magnetic Shape Memory alloys (MSMA) were studied to verify if they are suitable for trailing edge flapping. To do so, a constitutive model for a push-push actuator was created and a prototype was manufactured in LAPLACE facilities.

2.1.1 Constitutive model

Magnetic shape memory alloys are a new type of smart material that, after the application of a magnetic field, are able to deform between 6-12% of their initial length [21]. This indicates that they can be used as the basic principle of many electromagnetic devices such as sensors and actuators. The frequency band in which we can use MSMA is much higher than that of conventional SMA [22]. This difference can be explained by the deformation mechanism of AMFMs where there is no phase change between austenite and martensite.

Ni-Mn-Ga alloys are the most commonly found in the literature due to the

achieved strain values that are higher than those of piezoelectric materials and of the same order of magnitude as SMA. The shape of MSMA can be controlled using the application of a magnetic field and a compressive mechanical stress as explained by Schmidt [23]. MSMA allow us to design several different types of devices. In order to reduce the disadvantages caused by the hysteresis of the material, Gauthier [24] developed a push-pull actuator that reaches strain levels of 2%. Krevet [25] performed numerical simulations for a device that uses an MSMA film as the actuating principle, their results show out-of-plane deflections of 17%.

The model created from the constitutive equations of MSMA predicts the nonlinear behavior of the material as a function of the applied magnetic field and the mechanical stress in which it is subjected. It was developed by Kiefer [26]. Through the analysis of the material microstructure, the martensitic variant volume fraction ξ, the strain tensor due to reorientation ϵ_r the magnetic domain volume fraction α, and the angles between the magnetization vectors and the favorable magnetization axes θ_j were defined as internal state variables. To simplify the formulation of the equation, we consider the presence of only two martensite variants after the application of prestress.

The nomenclature of the MSMA structure is shown in Figure 12. The volume of variant 1, favored by the presence of the prestress, is represented by ξ. Then, we notice that the volume of variant 2, favored by the magnetic field, corresponds to $1-\xi$. Similarly, α is the volume fraction of domain 1, in which the favorable magnetization axis is oriented in the positive direction, and $1-\alpha$ is the volume fraction of domain 2 that has the opposite orientation.

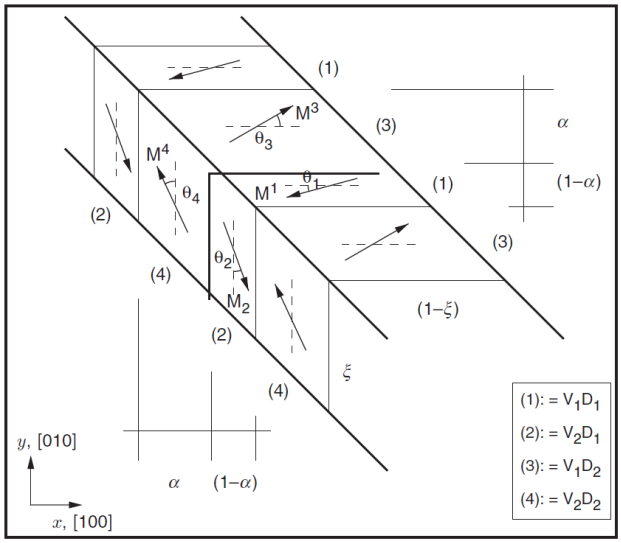

Figure 2.2: Magnetic domains and martensitic variants [26].

The total strain of MSMA is considered as the sum of the elastic component ε^e and the reorientation strain ε^r. Both are functions of the variant volume fraction:

$$\varepsilon = \varepsilon^e + \varepsilon^r \tag{2.1}$$

$$\varepsilon^e = S(\xi)\sigma \tag{2.2}$$

$$\varepsilon^r = \Lambda^r \xi \tag{2.3}$$

Where σ is the mechanical stress, $S(\xi)$ is the compliance tensor of the material and Λ^r is the reorientation tensor which represents the direction and magnitude of the maximum deformation that the material can reach. The key point to model MSMA behavior is to compute the non-linear variant evolution ξ_{12} and ξ_{21}. For this, a trigonometric function is chosen and supplied internal parameters of the material such as the magneto-crystalline anisotropy constant ρK_1, the saturation magnetization $\mathrm{M_{sat}}$ and the maximum reorientation strain $\varepsilon^{r,max}$ which is considered to have only one direction:

$$\Lambda^r_{xx} = -\Lambda^r_{yy} = \varepsilon^{r,max} \tag{2.4}$$

$$\Lambda^r_{zz} = \Lambda^r_{xy} = \Lambda^r_{xz} = \Lambda^r_{yy} = 0 \tag{2.5}$$

The model must be calibrated with external parameters estimated from the magnetization curve of the material: the magnetic field values $H_y^{s(1,2)}$, $H_y^{f(1,2)}$, $H_y^{s(2,1)}$ and $H_y^{f(2,1)}$, which denote the start and end fields of the variant reorientation process, must be specified for each pre-stressing level. We draw tangent lines to the test line to obtain an approximate value of these parameters. Figure 2.3 shows this technique. The calibration is done by adjusting the values to approximate the theoretical curve to the experimental result. A complete description of this MSMA modeling approach is found in the work of Kiefer and Lagoudas [27].

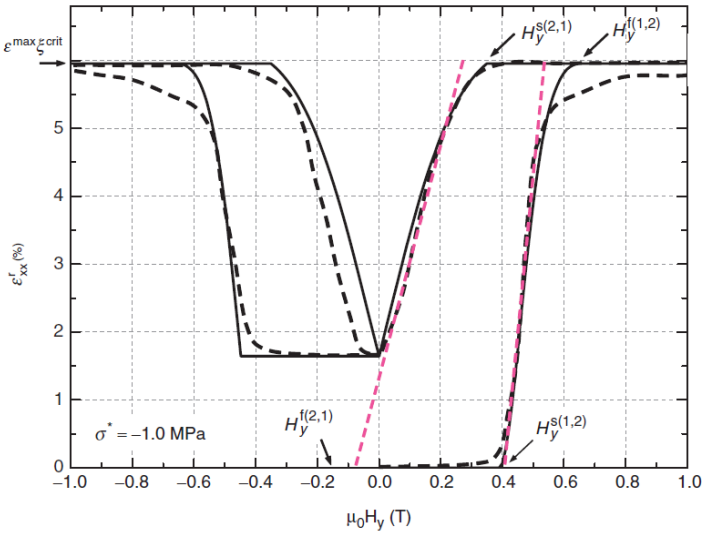

Figure 2.3: Calibration of the model parameters at 1 MPa prestress [27].

The implementation of this model requires a rigorous characterization campaign to obtain all the necessary parameters for variant evolution equations. It was then decided to use a simplified version of this model based on the interpolation of the magnetization curve. The set of parameters must be estimated for a fixed value of prestress σ^*. The equations that describe the variant evolution of martensite variants become:

$$\xi_{1,2}(H) = \xi^{crit}(\sigma^*)[1 - cos(\frac{H - H_y^{s(1,2)}}{H_y^{f(1,2)} - H_y^{s(1,2)}}\pi)] \tag{2.6}$$

$$\xi_{2,1}(H) = \xi^{crit}(\sigma^*) sin(\frac{H - H_y^{f(2,1)}}{H_y^{s(2,1)} - H_y^{f(2,1)}} \frac{\pi}{2}) \tag{2.7}$$

2.1.2 Actuator design

The chosen configuration for the trailing edge actuator is a push-push design. The trailing edge can oscillate around an axis of rotation, the vibration is generated by the action of two MSMA elements positioned with a center distance e shown in the Figure 2.4.

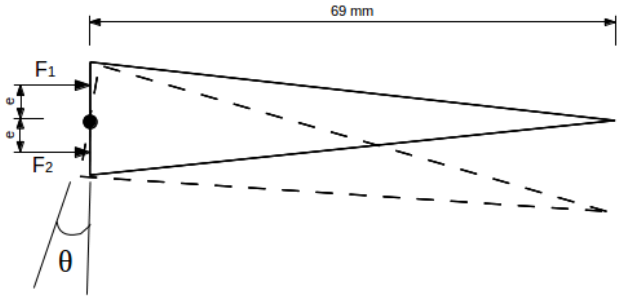

Figure 2.4: Simplified system schematic.

In order to generate the magnetic field to drive the deformation of MSMA, a magnetic circuit was made. This consists of a coil and a circuit of ferromagnetic material to conduct the magnetic field to the MSMA sample. The circuit has been dimensioned with the aim of establishing a homogeneous magnetic field throughout the shape memory material and capable of reaching its saturation region. Circuit parameters were set to ensure these characteristics, such as the magnitude of the magnetic field, the cross-section of the ferromagnetic material that conducts the field and the electric current supplied to the circuit, for example.

All the elements of the circuit were modeled with Autodesk Inventor software. Figure 2.5 shows the result of the 3D modelling and the assembled circuit. We find the core of the coil, without the wire, marked in red, the parts in blue are the mounting brackets of the ferromagnetic circuit. The latter is shown in gray. We notice the two threaded pieces that serve to hold the sample between the sections of the ferromagnetic circuit. These two elements are attached to the tensile/compression testing machine for the MSMA pre-stressing.

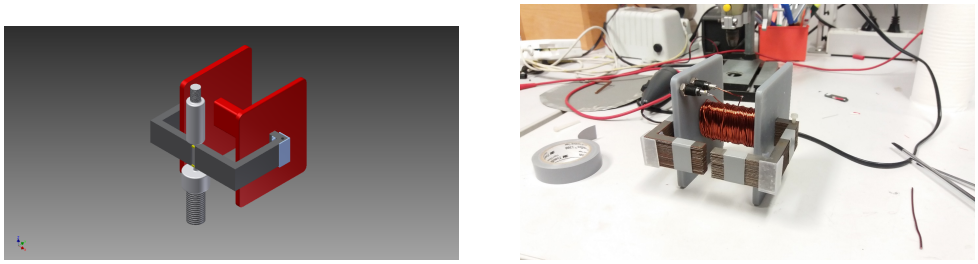

(a) 3D modelling. (b) Assembled circuit

Figure 2.5: Manufacturing of magnetic circuit.

Unfortunately, because of manufacturing reasons the home made circuit could not reach the expected magnetic field critical value. To achieve the specified magnitude according to the MSMA sample supplier, a company must be outsourced to this work. Besides its limitations, the circuit presents good response when excited by the external power source as the characterization curve in Figure 2.6 shows. The curve linearity is observed up to 4A and no hysteresis is detected. The low value of saturation is certainly caused by the discontinuity between the magnetic elements of the circuit that had to be assembled manually.

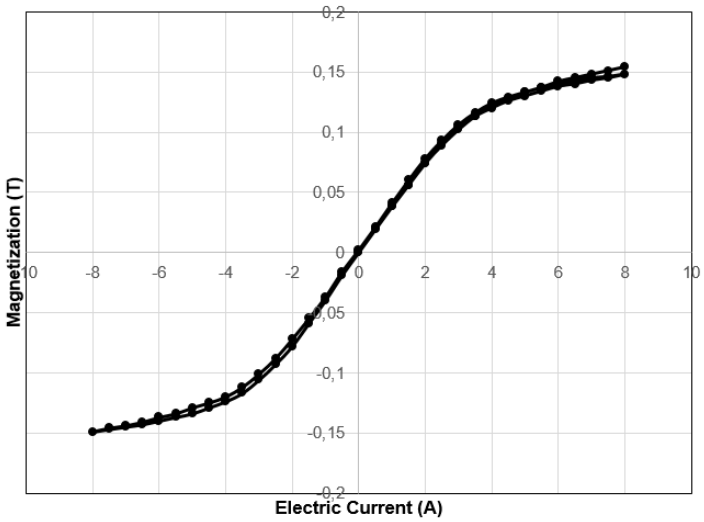

Figure 2.6: Characterization of magnetic circuit.

2.1.3 Simulation results and discussion

The complete model couples the MSMA elements to the trailing edge structure. The model architecture is seen in Figure 2.7. Simulink was used for the simulation. The external magnetic field is created with a signal generator. Two separated circuits are considered to actuate the magnetic elements alternately. The magnetic field triggers the variant evolution of the MSMA and generates a mechanical deformation that pushes the trailing edge up and downwards. Since martensite variant evolution depends on the mechanical stress applied to the element, these values must be updated at each interaction.

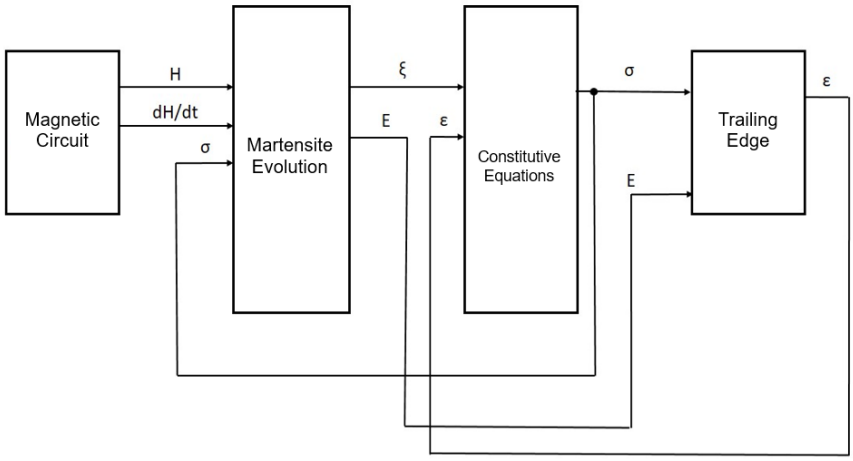

Figure 2.7: Complete model architecture.

Figure 2.8 shows the time series of the variant evolution for a sinusoidal magnetic field at 100 Hz. There is a phase shift of π between the two input signals to assure good alternation among the MSMA elements. One can see that each actuator reaches the maximum volume of the target martensite variant and restores the initial configuration before giving way to the other element. Like all mechanical systems, the vibration of the trailing edge is a function of the actuation frequency. The tip displacement goes up to 3 mm when excited at 100 Hz, but it loses in terms of amplitude when actuation frequency is higher. Figure 2.9 shows the results of two test cases at 100 Hz and 200 Hz. The trailing edge can be designed to place its natural mode of vibration at strategical frequencies.

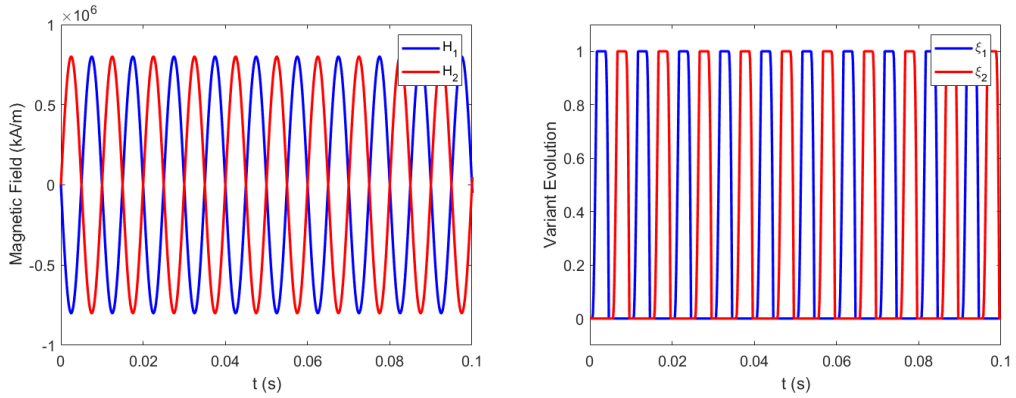

(a) External magnetic field. (b) Martensite variant evolution

Figure 2.8: Simulation results.

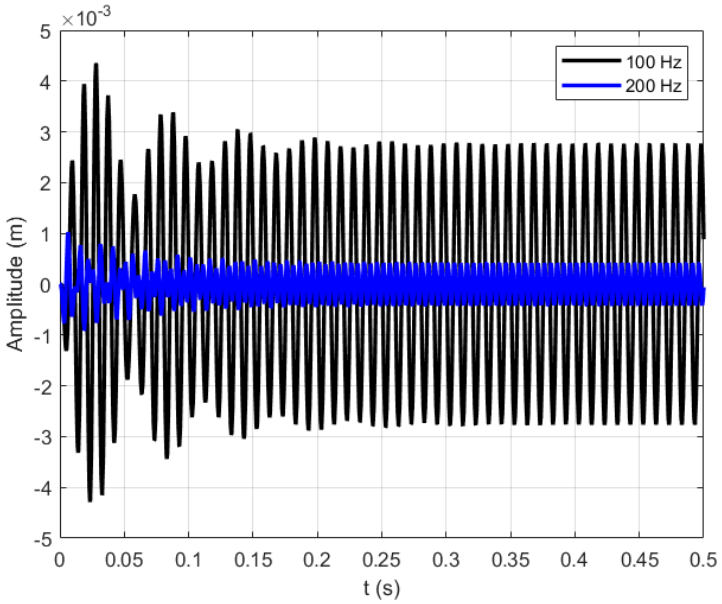

Figure 2.9: Tip displacement of the trailing edge actuator.

The model presents consistent results and simulation indicates good vibration amplitude in the trailing edge region, but it was decided not to continue the development of the magnetic actuator. Besides the satisfying performance, the system is not suitable for aerodynamic purposes because of its difficult integration. The magnetic circuit needed to actuate the MSMA demands too much space, so the task to embed it in a confined region of the wing is virtually impossible. Nevertheless, this model architecture was created in such way that its adaptation to diversified applications is relatively simple. Therefore, the MSMA remain an interesting solution for high frequency and precise operations. The procedure for the magnetic circuit sizing and the properties of the MSMA sample used in the actuator model are found in Appendix A and B respectively.

2.2 Smart materials for actuators design

In this section the materials chosen for the design of the morphing actuators are presented. In order to actuate the trailing edge at high frequency, the MSMA have given way to piezoelectric materials while Shape Memory Alloys are employed to perform camber control.

2.2.1 Piezoelectric materials

Thanks to their versatility, piezoelectric materials are largely used for several industrial applications in the fields of actuators and sensors. The piezoelectric effect was discovered in 1880 by the brothers Paul-Jacques and Pierre. This effect is the capacity of certain materials to convert mechanical stress into electrical charge and vice and versa. These materials must go through a magnetization process to obtain the piezoelectric characteristics [22]. It generates the reorientation of the dipoles of the material as it is shown in Figure 2.10. When the field is interrupted, the alloys retain their polarization.

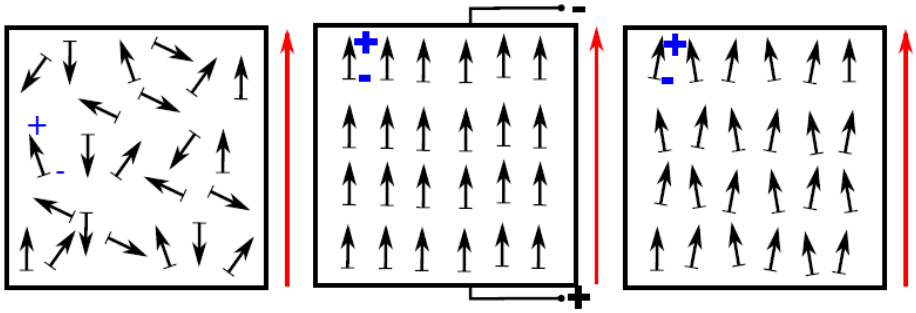

Figure 2.10: Polarization of a piezoelectric ceramic (polarization axis indicated by red arrow) [22].

There are many types of piezoelectric materials, each one has its specificities. Piezoelectric ceramics can be easily integrated and are suitable from low to very high actuation frequencies, but temperature range is a limitation [28, 29]. Piezoelectric polymers are flexible which also facilitates the integration, but they present lower electromechanical coupling if compared with piezoelectric ceramics [30]. This variety of materials makes possible the design of different types of actuators. Piezoelectric multilayer stack actuators represent an interesting way to increase the deformation of piezoelectric elements. This is achieved by bonding piezoelectric actuators of opposite polarity separated by a thin electrode together. Piezoelectric stacks have been used as linear push-push actuators to morph the edge of a plate [22] and the trailing edge of a NACA0012 wing for wind-tunnel experiments [31]. Another concept was designed using piezoelectric macro fiber composites (MFC) actuators [32]. This configuration allows the trailing edge to have more degrees of freedom as it is directly integrated to the morphing structure. This concept was chosen for the design of the reduced scale prototype of this work.

2.2.2 Shape Memory Alloys (SMA)

The shape memory effect is the ability of some metal alloys to recover an initial shape via thermal stimulus. The deformation mechanism is based on the phase change between internal crystalline phases. SMA are nickel-titanium alloys and, depending on the proportion of each element, its characteristics can change. At high temperature the SMA alloys are found in the form of austenite. After cooling, the phase changes to martensite. In order to be used

as an actuator, SMA must be ”trained” by applying a pre-strain before the integration. At room temperature, the mechanical stress exceeds the yield limit of the martensite generating a permanent deformation. After heating, in autenite phase, the material returns to its elastic regime and recovers the initial shape as it is seen in Figure 2.11. The textbook of Lexcellent [33] provides an extensive overview of SMA properties. As drawbacks we can cite the low actuation frequency and the reduced number of actuation cycles for large strain and stress operating conditions. But SMA present elevated specific actuation energy and they can reach up to 8% of deformation. Applications are found in aeronautics [34] and have already been tested in wind-tunnel experiments using a deformalble plate [35]. Thanks to its properties, SMA have been largely studied, specially in modelling [36, 37, 38].

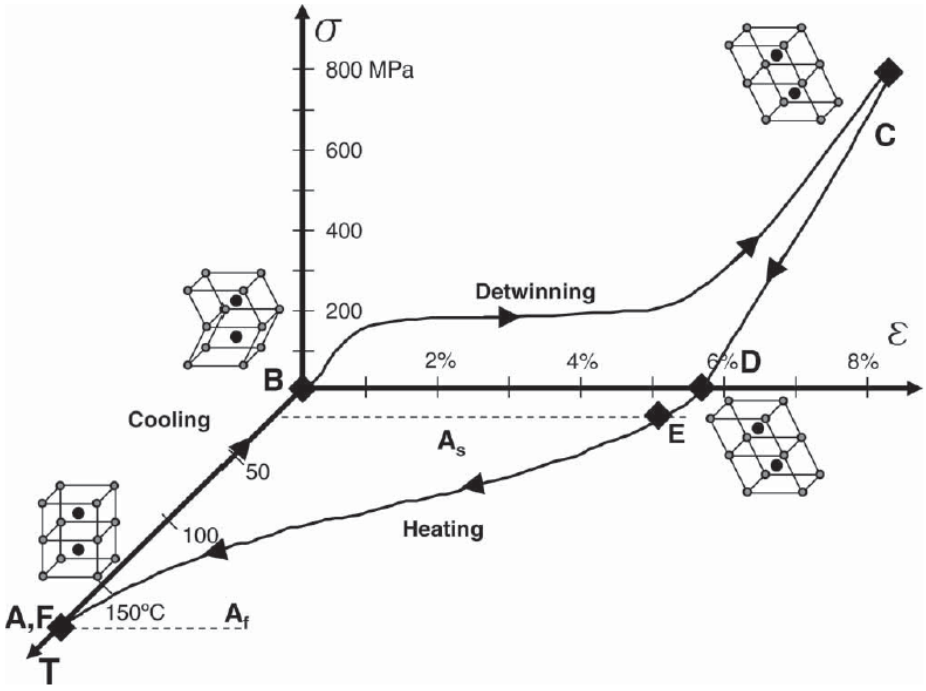

Figure 2.11: Experimental stress–strain–temperature curve of a NiTi SMA illustrating the shape memory effect (NiTiCu, Texas A&M University) [34].

2.3 RS Prototype of the SMS project

The prototype was designed by LAPLACE team in collaboration with IMFT, according to the "hybrid electroactive morphing concepts", in the context of the PhD thesis of G. Jodin [39]. It corresponds to an A320 airfoil. The chord is 700 mm and the span is 590 mm. Both actuation systems are embedded in the last 30% of the chord, following real flap configuration in commercial aircrafts as it is shown in Figure 2.13.

The camber control actuation system is made of six Shape Memory Alloy (SMA) wires pre strained to +3% with respect to their initial length in the same way as by Scheller [22]. At room temperature, SMA present martensite crystalline structure, but when it is heated by Joule effect, the crystalline structure becomes austenite. This modification in the material internal structure generates a change from plastic to elastic regime, so the SMA tend to recover the initial length once actuation is interrupted. The stress created during this transformation generates a bending moment capable of modifying the camber of the prototype.

The piezoelectric actuators, also called Higher Frequency Vibrating Trailing Edge (HFVTE) is designed to reach vibration amplitudes up to 2 mm depending on the actuation frequency. Figure 3 shows the HFVTE, it is formed by two piezoelectric MFC patches with active length of 35 mm glued on both sides of a metallic substrate. In order to obtain maximum displacement on both sides, the MFC patches are activated alternatively. Figure 2.12 shows the described actuators.

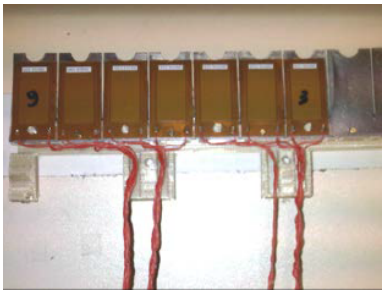

(a) MFC patches.

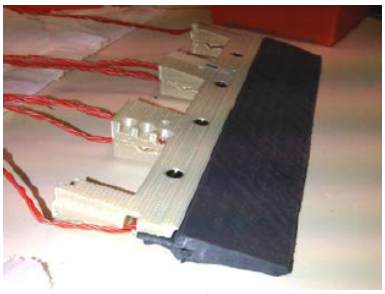

(b) Assembled HFVTE actuator.

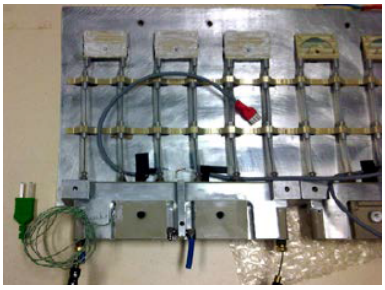

(c) SMA wires.

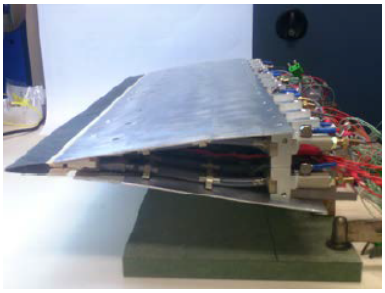

(d) Hybrid morphing test bench.

Figure 2.12: RS prototype actuators [39]

Both actuation systems allow us to act on two different times scales on the flow in the so-called "hybrid electroactive morphing", obeying the turbulence spectrum content of different time and length scales. While the SMA actuation operates at low frequencies, in the order of 1 Hz, and in high deformations, around 20% of the wing's chord, affecting the cambering and wing's deformation, the HFVTE actuation operates in a higher frequency range, up to 500 Hz, in small deformations. This actuation is able to inject smaller-scale vortex in the shear layers, thus manipulating the existing turbulence structure and producing suitable vortex breakdown of larger coherent structures, therefore enhancing beneficial vortex and destroying harmful ones to increase the aerodynamic performances. The association of these different actuations, operating at different time and length scales is a bio-inspired concept from the large span hunting birds who actuate simultaneously their wings, ailerons and feathers according to the sensing due to the pressure distribution, captured by their muscles and nervous system. A detailed description of the prototype design and manufacturing is found in the article

of Jodin [40] and Scheller [22]. Figure 2.14 shows the complete prototype.

All the experiments have been carried out in S4 wind-tunnel of IMFT. The test section is 592 mm width per 712 mm height. The wing is mounted at an incidence of 10°. The numerical simulations in synergy with these experiments have taken into account the present influence of the blockage ratio.

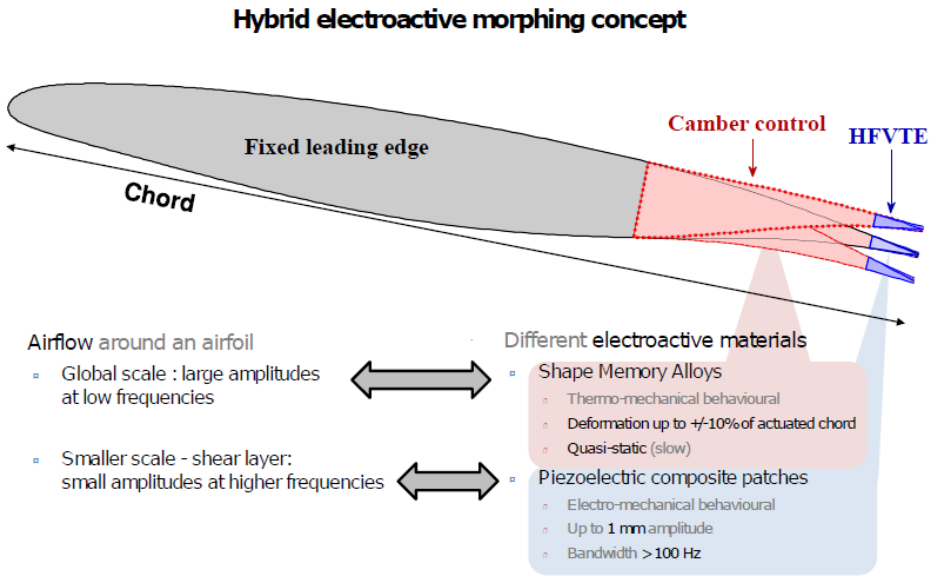

Figure 2.13: RS prototype description.

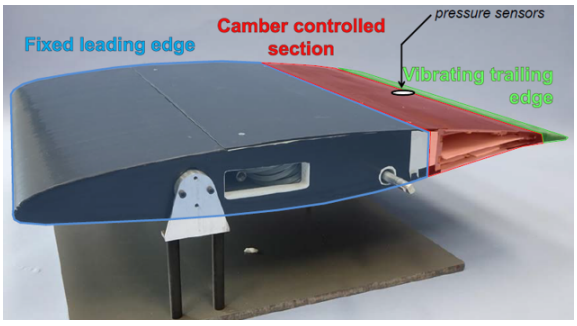

Figure 2.14: The Reduced Scale Prototype.

2.4 Actuators characterization

For the complete study of morphing, knowing the capabilities of the actuation systems of the prototype is as important as identifying the main aerodynamic instabilities present in the flow. This section is devoted to the characterization of HFVTE and SMA actuators. The different techniques were employed to investigate the response of the flap to open-loop actuation. First, the experimental set-up for piezoelectric characterization using a laser vibrometer is described. Then, the optical technique to capture the motion due to the SMA actuation inside the wind-tunnel is presented.

2.4.1 Piezoelectric actuators

In order to obtain better performance, piezoelectric actuators can be designed to operate at its natural frequency. Jodin PhD thesis [39] shows that the amplitude of flapping has an important role on lift increase. It is therefore necessary to characterize the piezoelectric actuators to identify the frequency range where the MFC elements provide higher vibration amplitudes.

In this investigation a alternative to LabView and MatLab was used. Despite their well known efficiency to manage complex experimental set-ups, these software request high investment for the purchase of licenses. The Scilab Visa Toolbox is an interface for controlling hardware developed by the community and available for download free of charge. The toolbox is well documented and it is compatible with most of hardware available in the market. An arbitrary waveform generator model Tektronix AFG320 was used to supply the actuators with the input signal. Data acquisition has been made with an oscilloscope model Tektronix 4034 with sampling frequency of 500k samples per second and record length of 100k elements. A laser vibrometer was used to measure the tip velocity of the trailing edge. The total displacement was calculate by numerical integration. The experiment was carried outside the wind-tunnel due to the long distance between the test section and the laser receptor.

Figure 2.15 shows the result of the characterization. The piezoelectric actuators were tested by varying their supplied tension from 50% up to their maximum capacity. The natural frequency of the actuator is located between 110 and 120 Hz, reaching 2 mm of maximum displacement. This amplitude is consistent with that used in simulations.

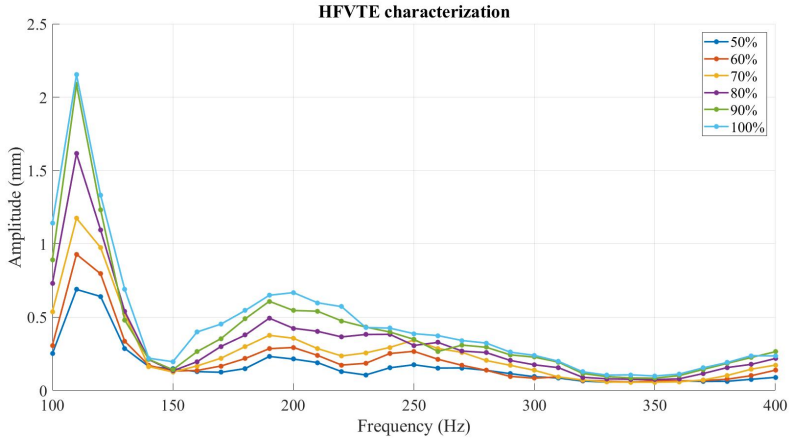

Figure 2.15: Characterization of HFVTE actuators.

2.4.2 SMA actuators

A LaVision camera model Imager sCMOS was used to record the flap during cambering. The images were sampled at 50Hz. For post-processing, the software DaVis from LaVision was chosen. It runs a PIV computation to trace the trajectories of small particles painted on the flap surface. This technique was employed for being less intrusive if compared to other instrumentation devices since images are recorded simultaneously with force and pressure measurements. SMA actuation is performed at open loop. The power supply has the electric tension as input parameter. The campaign has been carried out with actuation at 30 and 50 V. Figure 2.16 shows the normalized vertical position of the trailing edge as a function of the electric tension applied to the SMA. The results were obtained in the wind-tunnel at Reynolds number of 500,000. The bending force needed to camber the flap comes from the internal temperature-induced phase transformation. As it is expected from the constitutive law of SMA explained by Brinson [37], crystalline phase transition takes longer when 30 V are supplied to the actuator. An algorithm based on this actuation system able to predict the non-linear behavior of the SMA elements is presented by Simiriotis [41].

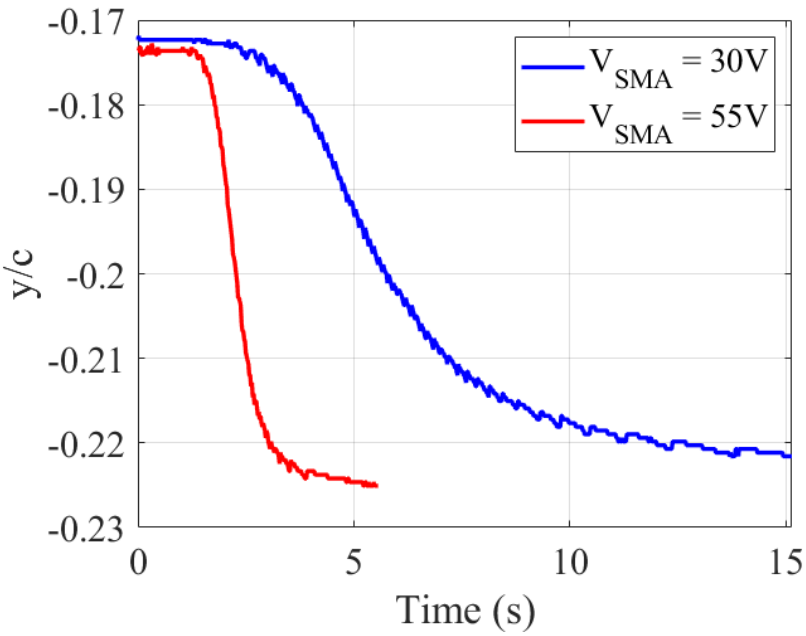

Figure 2.16: Tip displacement of the flap during SMA actuation.

Figure 2.17 shows the vertical velocity of the trailing edge for both supplied tensions. Its maximum value is reached in the inflection point of the displacement curve. The influence of the high frequency vibration during the descent of the flap was also investigated. On Figures 2.18 and 2.19 one can see the tip displacement and the vertical velocity for different hybrid morphing configurations. No major variation is detected, indicating that SMA actuation does not depend on the vibration frequency of the piezoelectric elements.

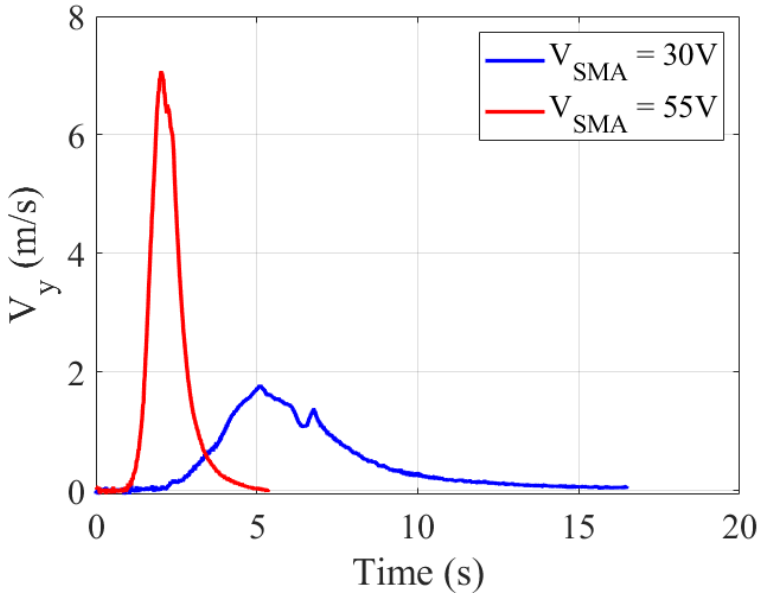

Figure 2.17: Tip velocity of the flap during SMA actuation.

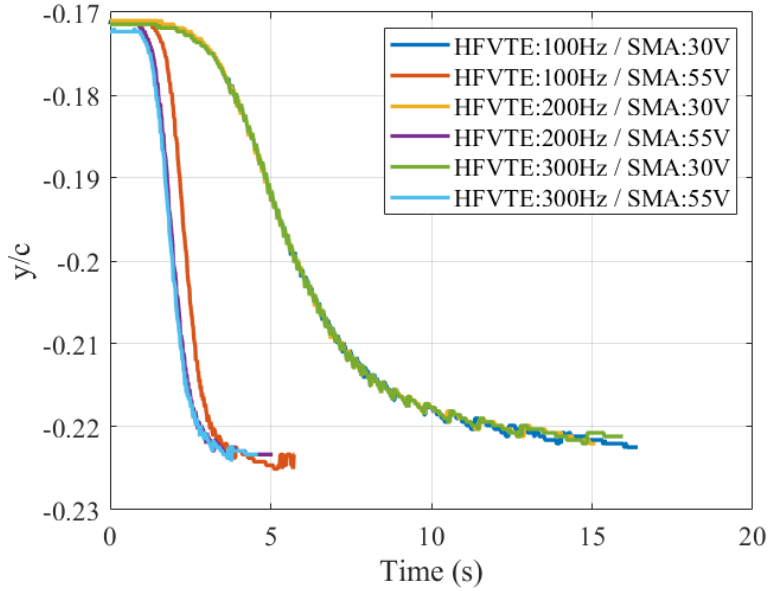

Figure 2.18: Characterization of flap cambering during hybrid morphing.

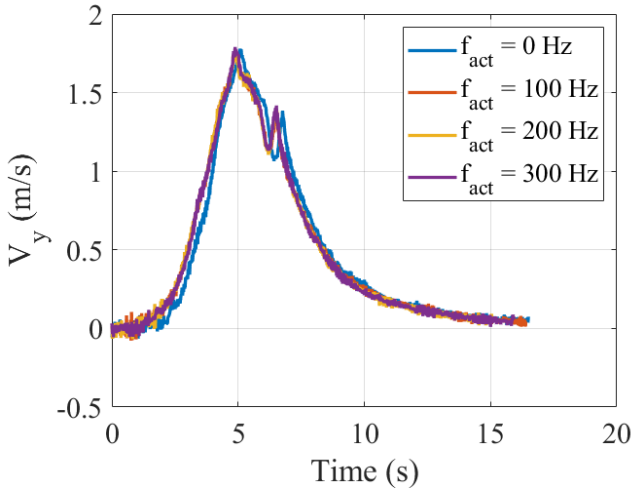

(a) SMA: 30 V

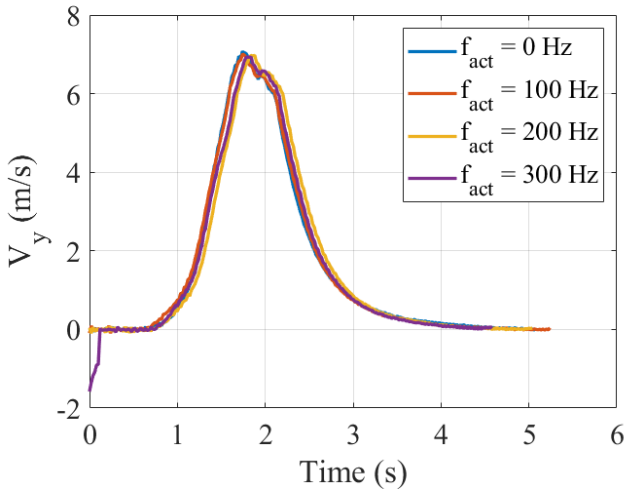

(b) SMA: 55 V

Figure 2.19: Tip velocity during hybrid morphing.

Chapter 3

Experimental set-up and post-processing tools for data analysis

In this chapter the experimental set-up assembled for this study is presented as well as the mathematical tools used for post-processing of the data. Time-Resolved Particle Image Velocimetry (TR-PIV) technique is described as it is one of the main experiments carried out in this work. Spectral analysis has been widely used for signal processing and to investigate the evolution of time series at specific points inside velocity fields. Finally, Proper Orthogonal Decomposition (POD) was chosen for modal analysis of flow dynamics. It is a useful tool for the identification of the main coherent structures present in the wake flow [42, 43, 44].

3.1 Time-Resolved Particle Image Velocimetry (TRPIV)

Particle Image Velocimetry is an experimental flow visualization technique. Conventional visualization methods using smoke wire and surface oil flow are widely used for analysis of vortex shedding and shear layer instabilities [14]. But PIV allows us to obtain a large set of flow features and its applications go from fluid dynamics to combustion and biology among many other fields. The advantage of PIV is its relative simplicity for two-dimensional flow visualizations and the extensive literature that can be found [45]. The IMFT

support team Signaux & Images has mastered the implementation of PIV set-up and the post-processing of data over the years. Figure 3.1 shows the representation of the experimental arrangement of the equipment required for a PIV campaign. Conventional PIV apparatus consists of a high speed camera, a laser and an optical lens to limit the region illuminated and generate the interrogation window. A software manages image acquisition by acting as a trigger to synchronize the camera and the laser. Small smoke particle or bubbles in the order of micrometers in diameter are inserted into the wind tunnel to be carried by the flow and be lighted by the laser sheet.

The images are recorded in short succession, so it is possible to track the particle by statistical cross-correlation. The correlation map will indicate a peak relative to the location of the particles identified in the following frame. This computation will determine their displacement. Since the time step is known, it is possible to generate the flow velocity field. Figure 3.2 helps to understand this tracking method.

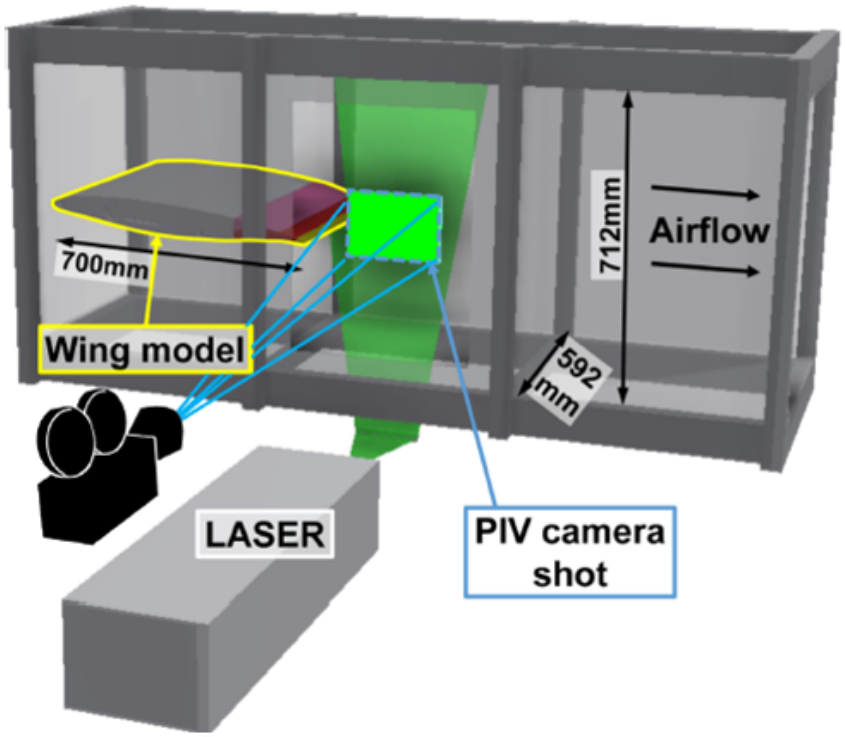

Figure 3.1: Schema of PIV set-up.

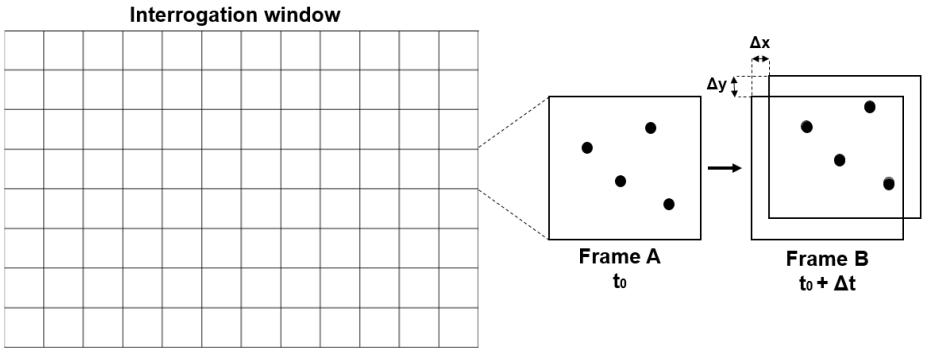

Figure 3.2: Correlation for particle tracking in PIV.

In the context of morphing, Tomographic PIV has been used to study the 3D aspect of wake turbulence past a thin plate [46]. The thickness of the laser sheet must be increased and four cameras are positioned in order to generate not an investigation window, but an investigation volume. Some test campaigns have already been carried out during this thesis to apply this configuration on the study of the morphing wing, the test bench can be seen in Figure 3.3. Some factors make Tomographic PIV in wind tunnels challenging. It is necessary to have a good resolution on the images to track the particles for a satisfactory time. In addition, to obtain enough signal the laser sheet must have sufficient energy to illuminate the particles, but power diminishes as the thickness increases. This trade-off results in a reduction of the investigation zone. Despite these challenges the Tomo-PIV allows us to generate the separated flow structure and to identify the coherent vortex pattern in a more complete way. That is why the test campaigns will continue to be carried out.

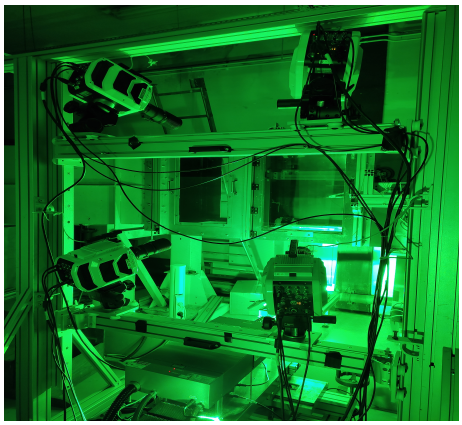

Figure 3.3: Tomographic PIV campaign in IMFT.

3.2 Post-processing of experimental data

3.2.1 Spectral Analysis

One of the foundations of signal processing is the spectral analysis. When we look into a time series, we can obtain statistical information like mean and RMS values, but much more can be accomplished by going from time to frequency domain. The Fourier Theorem states that any reasonably continuous signal can be expressed as a sum of a series of sine or cosine terms. By doing so it is possible to compute the amount of energy of a signal as a function of its frequency. The result is a complex-valued function, whose magnitude represents the energy of each periodical component present in the original function. Conventional methods to compute the Fourier Transform, like the FFT (Fast Fourier Transform), have good performance, but their use may not be the most appropriate in some cases. The advantage of using FFT is the spectral precision, the downside is its sensitivity to noise and non-stationarities. The Welch's method proposes a trade-off between high spectral resolution and reduced variance by manipulating a set of parameters. The idea behind this technique is to divide the signal into time windows, computing the periodogram of each segment and then averaging the results. Also, the signal partitions are often multiplied by a window function, such as the Gaussian or the Hamming windows, to avoid edge effects when the segments overlap. More details about the Welch's method and other signal processing tools can be found in the spectral analysis book of Stoica [47].

In the present thesis the stabilization of fluid flow instabilities by electroactive morphing is investigated. A well known and most simple way to post-treat the data is to consider the time-average decomposition. There are of course more elaborate decomposition forms, like the phase averaging [48], as well as modal decomposition. In the next chapters time-averaging was used for post-processing of unsteady pressure and lift measurements. Thus, the analyzed data can be written as:

$$u(t) = \overline{U}(t) + \tilde{u}(t) \tag{3.1}$$

Where $\overline{U}(t)$ is the mean value of the output signal u(t) and $\tilde{u}(t)$ is its unsteady component. Therefore the spectra presented in the next chapters have this general form:

$$U(f) = \{\tilde{u}(t)\} \tag{3.2}$$

3.2.2 Proper Orthogonal Decomposition (POD)

Any dynamic system can be considered as the sum of the individual contribution of its natural modes. The advantage of using this approach is to isolate a specific number of modes to identify the main features of the system. POD is a method to expand partial differential equations by finding optimal basis representation. Here we are interested in solving fluid flow problems. POD was applied in velocity fields computed by PIV, this approach allows us to detect the coherent structures featured by the flow on the basis of their wake number and frequency. POD has been largely used for post-processing of both numerical and experimental data [49]. For example, to solve the time evolution of a variable u:

$$u_t = M(u, u_x, u_{xx}, ..., x, t) \tag{3.3}$$

Where u_t depends on a non-linear function M of u and its derivatives:

$$u_t = \frac{\partial u}{\partial t}, u_x = \frac{\partial u}{\partial x}$$

To solve the equation forward in time we must discretize the space variable x into a finite number of elements. We name u_n the solution in the n point

of the grid:

$$u_n = u(x_n, t) \tag{3.4}$$
$$n = 1, 2, 3, ..., N$$

By approximating the derivatives using its neighboring points the equation 3.3 becomes:

$$\frac{du_n}{dt} = M(u_n, u_{n+1}, u_{n+2}, ..., x_n, t) \tag{3.5}$$
$$x \in [-L, L]$$

The next step is to perform separation of variables by assuming that the solution can be written as the product of two different functions, a matrix φthat contains the basis functions and $\vec{a}(t)$ which represents their time dynamics. It is important to chose a good set of basis functions to solve the time evolution of u from a finite number of elements using the formulation:

$$u(x, t) = \sum_{n=1}^{N} \vec{a_n}(t)\phi(x) \tag{3.6}$$

The solution can be found by expanding the equation 3.5 and picking an orthonormal basis set. To do so, we consider the following inner product between the basis functions:

$$\langle \phi_n, \phi_m \rangle = \int_{-L}^{L} \phi_n \phi_m^* \, dx \tag{3.7}$$

The main interest of using POD is to exchange a large partial differential equation by a large system of differential equations. The number of equations of the system can be inferior to N if the right set is chosen. The resulting expression after using the orthonormal basis functions is the finite system of differential equations:

$$\frac{da_m}{dt} = \langle \phi_m, M \rangle \tag{3.8}$$
$$m = 1, 2, ..., N$$

The method presented by Perrin [48] is selected to compute the modal reduction. This approach is particularly suitable for large experimental

database. The iflow field obtained with the PIV is discretize in N_x elements for each N snapshot. The obtained data matrix containing vertical and horizontal velocity components of each spacial sample is:

$$M = \begin{bmatrix} u_1^1 & u_1^2 & u_1^3 & \dots & u_1^{N-1} & u_1^N \\ u_2^1 & u_2^2 & u_2^3 & \ddots & u_2^{N-1} & u_2^N \\ \vdots & \vdots & \vdots & \ddots & \vdots & \vdots \\ u_{N_{x-1}}^1 & u_{N_{x-1}}^2 & u_{N_{x-1}}^3 & \ddots & u_{N_{x-1}}^{N-1} & u_{N_{x-1}}^N \\ u_{N_x}^1 & u_{N_x}^2 & u_{N_x}^3 & \ddots & u_N^{N-1} & u_N^N \\ v_1^1 & v_1^2 & v_1^3 & \ddots & v_1^{N-1} & v_1^N \\ v_2^1 & v_2^2 & v_2^3 & \ddots & v_2^{N-1} & v_2^N \\ \vdots & \vdots & \vdots & \ddots & \vdots & \vdots \\ v_{N_{x-1}}^1 & v_{N_{x-1}}^2 & v_{N_{x-1}}^3 & \ddots & v_{N_{x-1}}^{N-1} & v_{N_{x-1}}^N \\ v_{N_x}^1 & v_{N_x}^2 & v_{N_x}^3 & \dots & v_N^{N-1} & v_N^N \end{bmatrix} \tag{3.9}$$

Each column of M corresponds to one snapshot. Moving forward, the correlation matrix R can be written as:

$$R = \frac{1}{N} M^T \cdot M \tag{3.10}$$

Then the corresponding eigenvalue problem can be solved:

$$RA = \lambda A \tag{3.11}$$

Where λ is the array of eigenvalues and A is the matrix of eigenvectors. The computed eigenvalues are then rearranged in descending order. The eigenvectors matrix is employed to compute the spatial modes:

$$\phi_i = \frac{\sum_{j=1}^{N} A_j^i u^j}{\left\| \sum_{j=1}^{N} A_j^i u^j \right\|} \qquad i = 1, 2, ..., N \tag{3.12}$$

The computation of the temporal modes a_i are found be solving the system of differential equations 3.8:

$$a_i = \phi_i M \tag{3.13}$$

Chapter 4

Investigation of the cambering effects through SMA actuators by means of TR-PIV

In this chapter the SMA actuation is studied by means of Particle Image Velocimetry. The parameter of this campaign were chosen to approach the duration of numeric simulations and make possible the analogy between both results. First, the equipment assembled for the experimental campaign is described, then PIV and POD results will be discussed.

4.1 Experimental set-up

The PIV campaign was performed to investigate the influence of the SMA actuation on the flow. Images were sampled at a rate of 5 kHz using a digital high-speed camera Phanton V2012. The laser sheet is generated by a Photonics DM60-527-DH. To obtain an investigation window size of 170 per 260 mm, 0,5 µm particles were employed. Furthermore, in other to image both the upper and the lower surfaces of the wing a 400mm Nikon lens with a focal distance of 3 m was chosen. The complete experimental set-up is found in Figure 4.1. It was necessary to use a flexible mask to avoid direct laser reflection on the prototype surface. It made it complicated the prost-processing of raw images before the PIV calculation. In addition to the difference of light intensity in the investigation window, an adaptable filter had to be applied to follow the position of the flap. These steps are shown

in Figure 4.2. All experiments have been carried out at Reynolds Number of 1M. Matlab and the commercial software DaVis10 from LaVision was used for post-processing.

SMA are supplied with voltage in order to reach full camber position in about 1,5 s. The tip displacement corresponds to 25 mm. Snapshots of the acquisition sequence show two different solution times of the PIV computation (Figure 4.3). As it is expected, one can see the increase of the recirculation zone in the wake once full cambering is reached by means of SMA actuation.

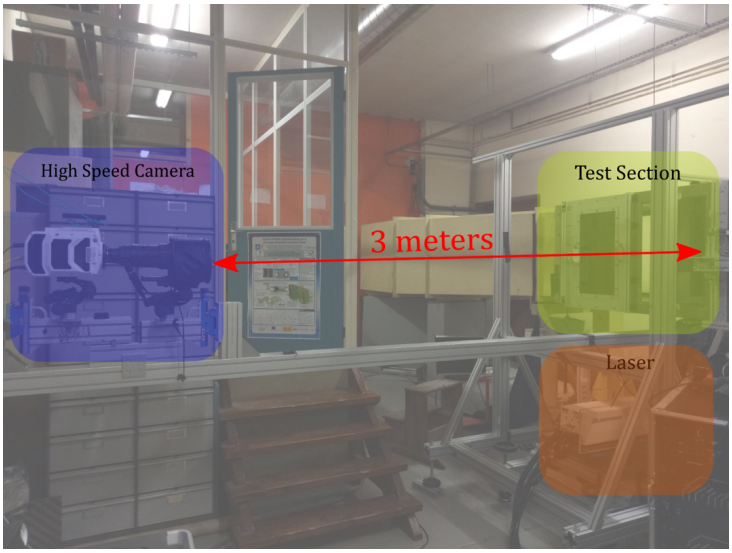

Figure 4.1: Experimental set-up of PIV campaign at IMFT facilities.

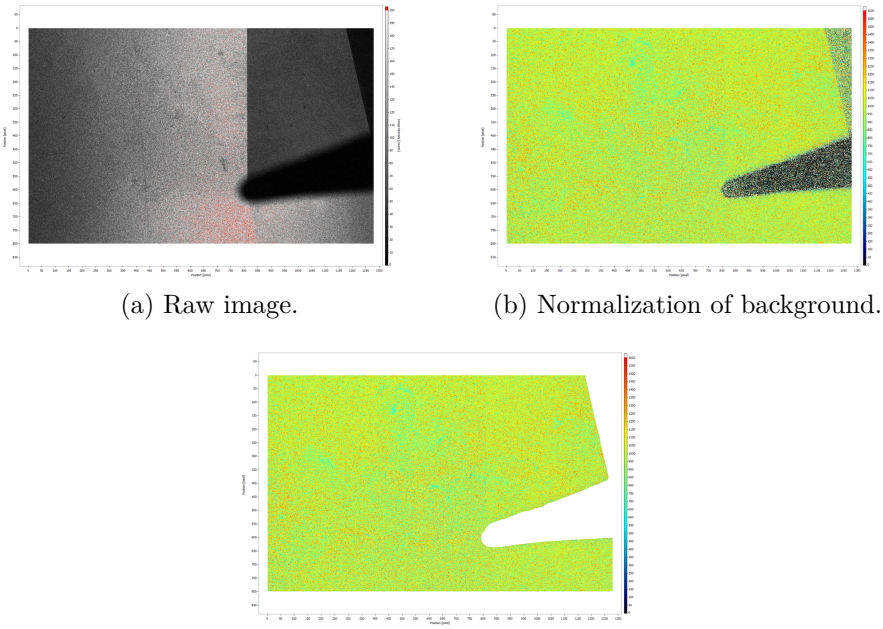

(a) Raw image.

(b) Normalization of background.

(c) Adaptable mask applied.

Figure 4.2: Post-processing of raw images for PIV calculation.

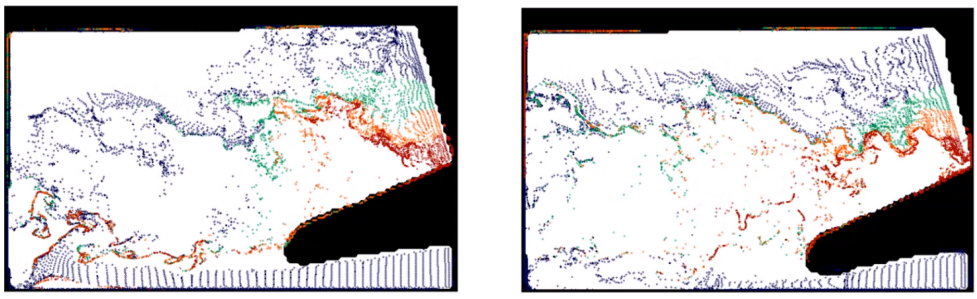

(a) Static configuration.

(b) Full camber position.

Figure 4.3: Snapshots of PIV campaign.

4.2 Proper Orthogonal Decomposition (POD) analysis

Modal analysis has been performed on the grid despite the motion of the flap. The POD allows us to perform modal reduction of dynamic systems. The first mode, which corresponds to the mean flow velocity, together with a specific number of higher order modes can be used to reconstruct the system by applying the reverse process of the decomposition. This mode reduction works like a filter, where only a selected group of coherent structures are represented.

To understand the flow dynamics during SMA actuation, the modal reduction was employed using high energy modes from 1 to 5. The energy distribution of the modes during SMA actuation can be seen in Figure 4.4. Snapshots of the POD reduction in Figure 4.5 illustrate the main features shown by the modal reconstruction. Streamlines help to observe the coherent structures generated during the flap's descent in four different moments, t* represents the normalized time step. The snapshots show the formation of a recirculation zone above the flap due to SMA actuation. A small vortex is generated in the wake of the trailing edge followed, as camber increases, by a bigger one. Snapshots of velocity contours in Figure 4.6 at t* = 0,75 also illustrate the massive recirculation zone created.

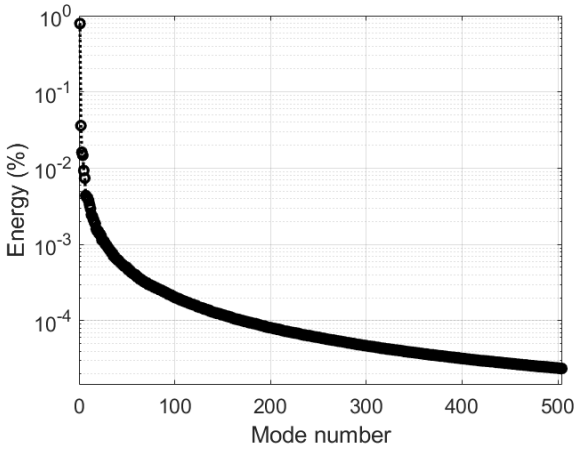

Figure 4.4: Energy distribution of POD decomposition of SMA actuation.

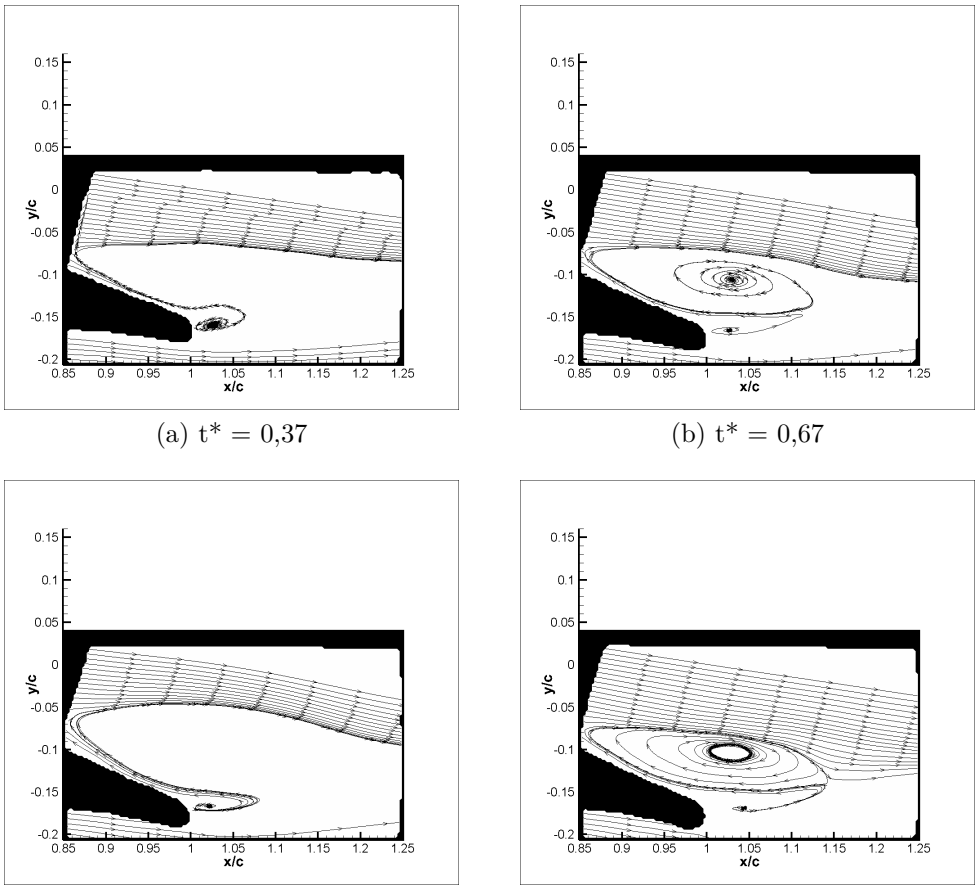

(a) t* = 0,37 (b) t* = 0,67

(c) t* = 0,74 (d) t* = 0,75

Figure 4.5: Snapshots of POD reconstruction using high energy modes.

Streamlines and vertical velocity contours are superposed to better understand flow dynamics during dynamic cambering. Monitor points are used to verify the periodicity of the main vortex obtained due to the von Karman instability. Both elements can be seen in Figure 4.7. Despite the short duration of SMA actuation, the spectra of the vertical velocity V_y on the monitor points, seen in Figure 4.8, show natural frequencies around 30 Hz followed by the first harmonic around 60 Hz. The spectra of the mode's temporal coefficient show similar natural frequencies of the monitor points, between 30 and 40 Hz, as it can be seen in Figure 4.9, which confirms the low frequency aspect of high energy coherent structures highlighted by the POD

reduction. The low pressure zone created by the SMA actuation generates a suction region above the flap.

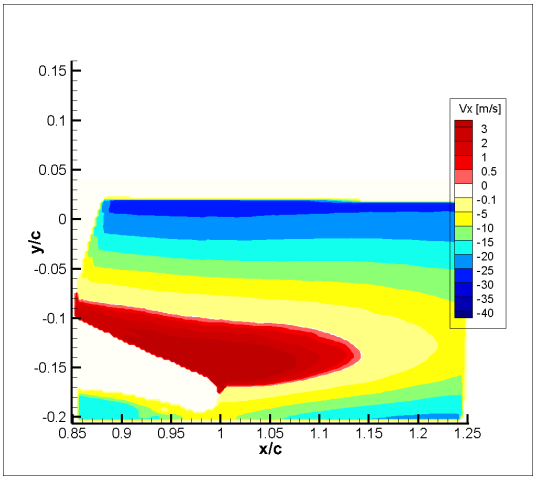

(a) V_x

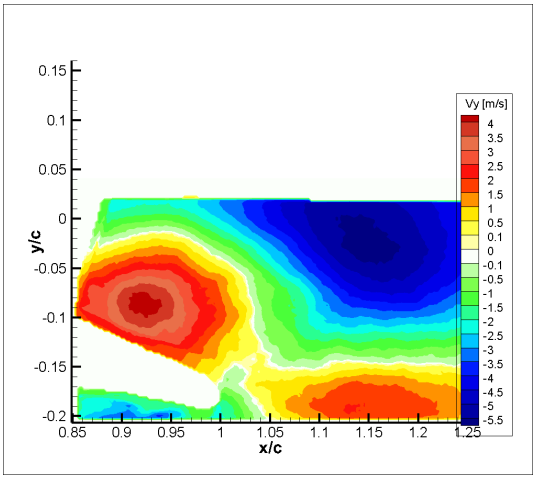

(b) V_y

Figure 4.6: Velocity contours during SMA actuation at t* = 0,75.

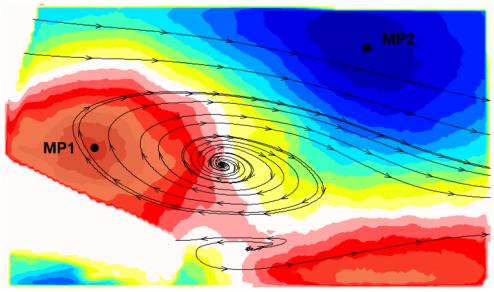

MP	x/c	y/c
1	0,92	-0,09
2	1,15	0

Figure 4.7: Monitor points used for spectral analysis.

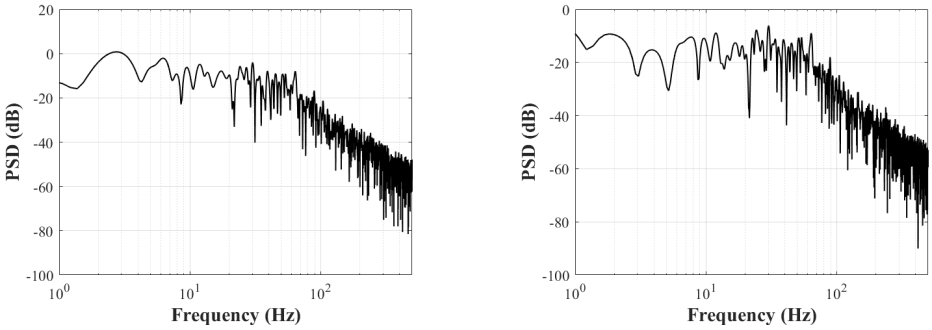

(a) MP1 (b) MP2

Figure 4.8: Spectra of monitor points.

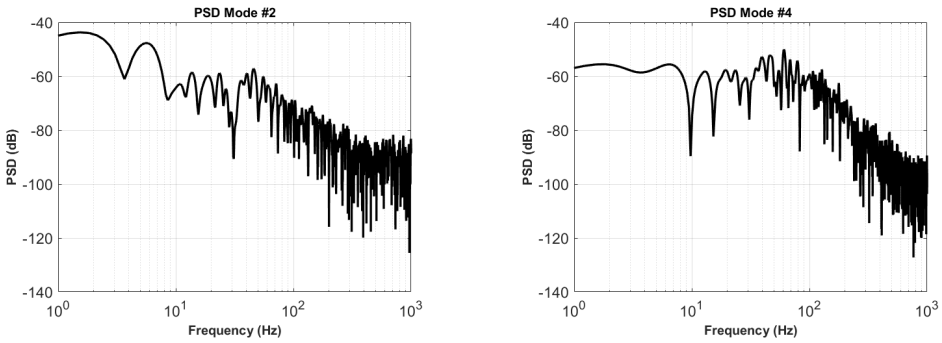

(a) Mode 2 (b) Mode 4

Figure 4.9: Spectra of temporal coefficients of POD modes.

The transient aspect of the flow pushes forward the structures that form the von Kármán instabilities into high order modes. Another POD reconstruction has been computed using the range of modes from 10 to 21 in order to spot this kind of vortex. Figure 4.10 shows a snapshot of the reconstructed flow. The effects of the suction zone can still be seen, but one can observe the formation of coherent structures in the upper shear layer region. The spectra the temporal coefficient of modes 10 and 12 in Figure 4.11 indicates a natural frequency of this phenomenon near 70 Hz.

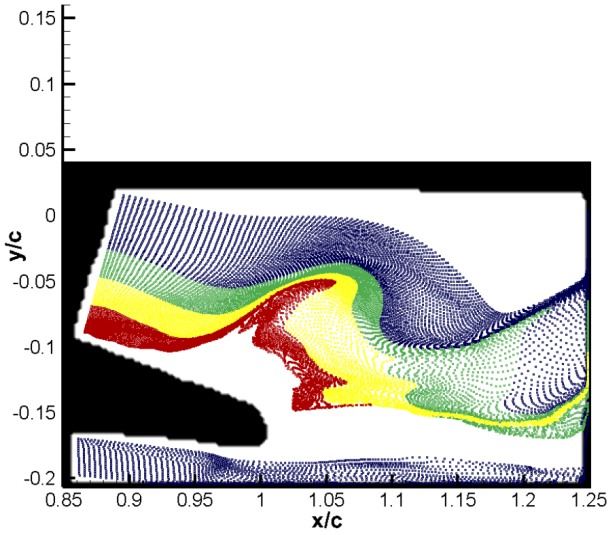

Figure 4.10: Snapshot from POD reconstruction of the flow using range of modes between 10 and 21.

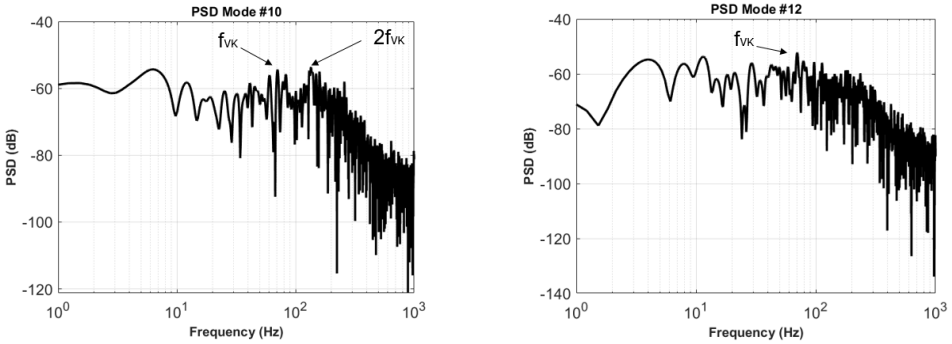

(a) Mode 10

(b) Mode 12

Figure 4.11: Spectra of temporal coefficients of POD modes.

4.3 Chapter conclusion

A complex experimental set-up was assembled to study the dynamics of flow passing through the prototype during SMA actuation at high Reynolds number. The present experimental investigation has captured the cambering effects on the shear layers and on the main vortex dynamics thanks to TR-PIV. The post-processing of raw images was a challenge once the flap was included in the investigation window. POD allowed identifying flow dynamics during a cycle of descending motion of the wing in which the last 30% of its chord has been deformed thanks to SMA actuators, according to a top descending velocity of 7 m/s and duration of about 1,5 seconds. POD reduction shows that this kind of actuation generates high energy structures as a massive recirculation zone is created above the flap. The transient regimes makes difficult the characterization of the main coherent structures created as the flap cambers, but PIV allows us to understand the mechanism that generates lift increase.

The results at static configuration obtained in this campaign will be revisited in the chapter dedicated to the feedback control design.

Chapter 5

Trailing Edge actuation

5.1 Wind-Tunnel experiments

Monochromatic piezoelectric actuation in a higher frequency range than the one obtained through the SMAs applied in the near trailing edge region is investigated in the next sections by means of unsteady pressure and lift measurements as well as TRPIV. These experiments have been carried out at Re = 1M. Spectral analysis is used to study the effects of this morphing concept on the fluid-structure interaction and on the aerodynamic performances and noise sources. This morphing concept has been realised by a series of MFC type (Macro-Fiber Composites) actuators with active length of 35 mm disposed in the trailing edge region along the 590 mm span. Furthermore, modal analysis and reconstruction through POD has been employed. POD was employed to identify how the piezoelectric actuation affects the fluid-structure system. Figure 5.1 shows the results of 3D simulations by Simiriotis [50] and Marouf [51] of the flow dynamics past the trailing edge in static configuration.

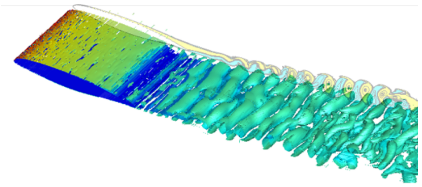

(a) 3D structure of the flow. Static configuration [51].

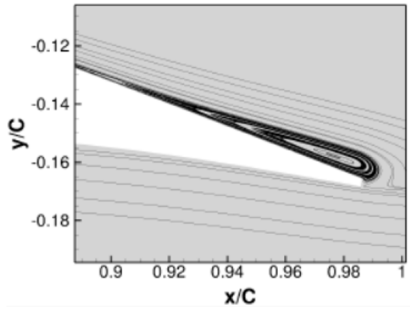

(b) Zoom of the recirculation region in the median plane [51].

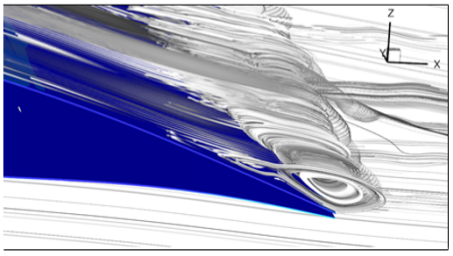

(c) Zoom of 3D recirculation region by Simiriotis [50].

Figure 5.1: Simulation results of 3D structure of the flow.

5.1.1 Experimental set-up

Actuation by means of the MFC type elements in the range of frequency of 50 to 400 Hz and in low amplitude, in the order of 1 mm, has been applied on the RS prototype of the SMS project. Data are sampled at $F_s = 6$ kHz for the pressure signals using highly sensitive piezoelectric pressure transducers MEGGITT 8507C-1 lined up at 56% spanwise in 60 and 85% of the chord. Sampling frequency is $F_s = 5$ kHz for lift measurements. An analogical filter was used for acquisition of pressure data to avoid electronic noise; the cut-off frequency is $F_{cut\text{-}off} = 1$ kHz. Figure 5.2 illustrates the set-up used for pressure data acquisition. For experimental reasons the piezoelectric actuators were supplied with 70% of their capacity.

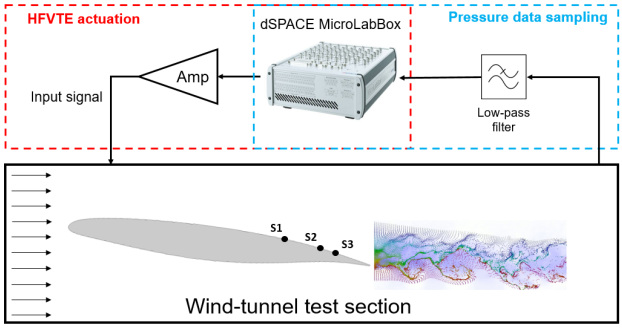

Figure 5.2: Experimental set-up for unsteady pressure measurements.

5.1.2 Lift measurements

The spectra of the fluctuating lift force have been measured by means of a piezoelectric balance designed by Scheller [22] and Jodin [39]. The lift coefficient signals are presented in Figure 5.3. They show important effects of HFVTE actuation on the fluid-structure interaction. It has been found that actuation frequencies in the range from 100 to 200 Hz attenuate significantly the amplitude of the power spectra in different regions. From 250 to 320 Hz, different effects can be seen.

Damping of the magnitude of the spectrum is found between 20 and 30 Hz for actuation frequencies up to $f_a = 250$ Hz. Thanks to analysis from numerical simulations [50] carried out simultaneously and in synergy with the present experiments within the SMS project, it was analysed that this frequency range corresponds to the Von Kármán mode, formed from the interaction of the two separated shear layers at a specific distance downstream. In the frequency range of 40 to 70 Hz in these spectra, a drastic decrease of the spectral amplitude, in terms of dB, has been obtained, concerning the actuation frequencies $f_a = 120$ and 170 Hz. Therefore, this indicates an optimal actuation range. Thanks to these results, monochromatic actuation of the trailing edge can be linked to the reduction of aerodynamic instabilities related to low frequency vortex present on the flow.

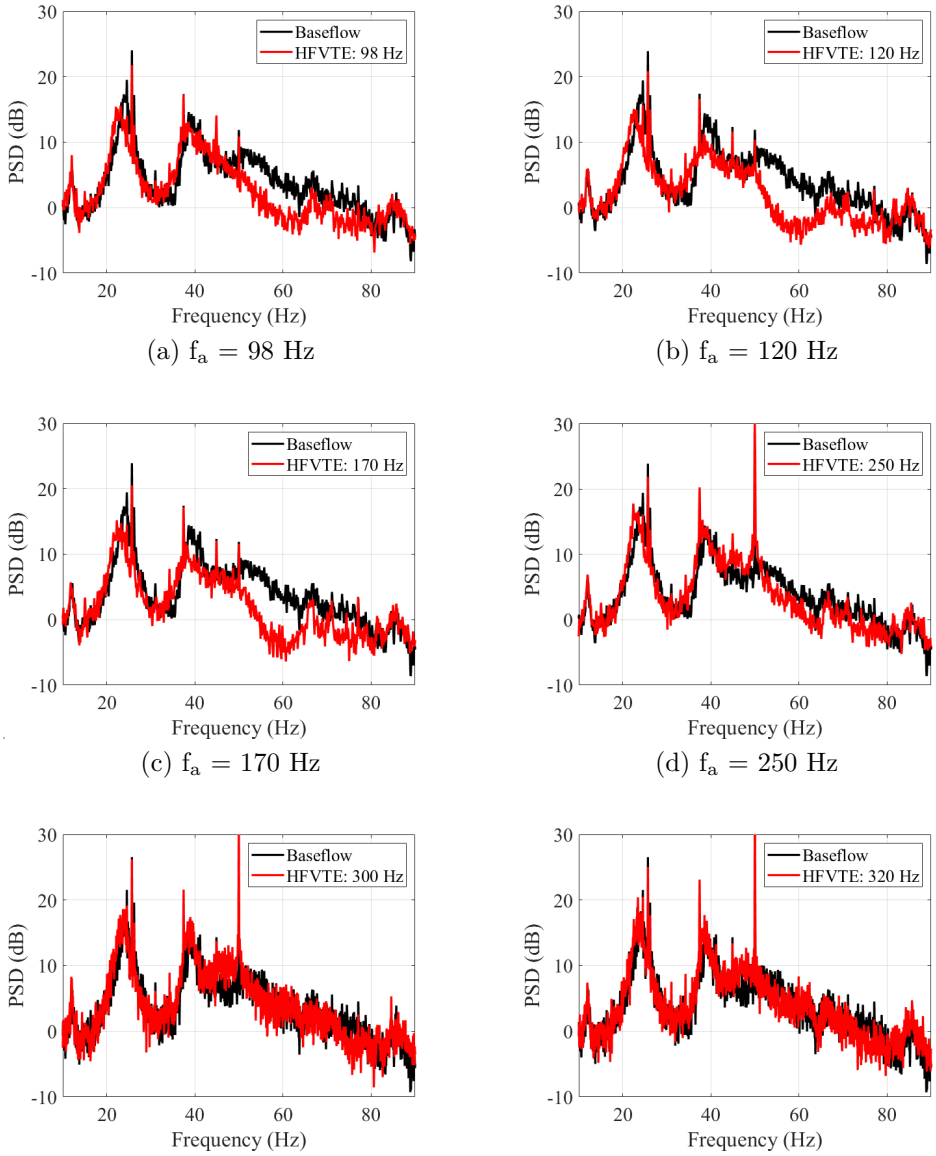

(a) f_a = 98 Hz (b) f_a = 120 Hz

(c) f_a = 170 Hz (d) f_a = 250 Hz

(e) f_a = 300 Hz (f) f_a = 320 Hz

Figure 5.3: Spectra of lift coefficient.

At higher actuation frequencies such as f_a = 250 and 320 Hz, HFVTE acts differently. The spectra do not present major damping due to morphing. Additionally, the frequency peak around 50Hz is reinforced. Figure 5.4 shows the spectra of signals sampled for f_a = 8, 12 and 30 Hz. The spectra of the actuation cases are practically superposed to the static (non-morphing) cases indicating no major effect of the monochromatic piezoelectric vibration in this range.

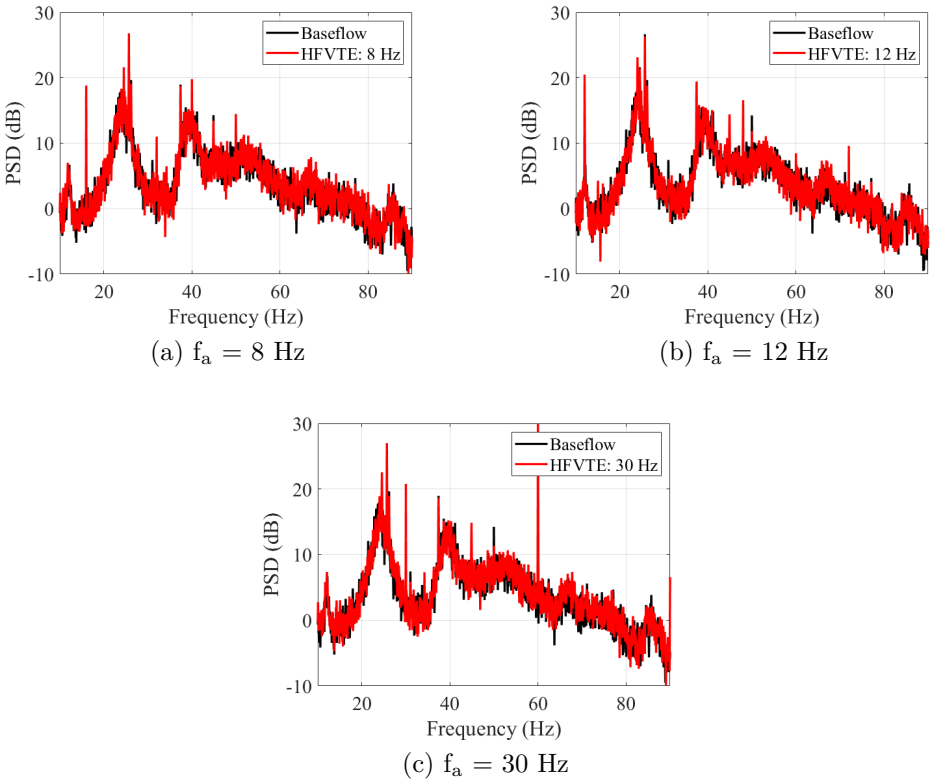

(a) f_a = 8 Hz

(b) f_a = 12 Hz

(c) f_a = 30 Hz

Figure 5.4: Lift coefficient spectra at low actuation frequency.

5.1.3 Unsteady pressure measurements

Figure 5.5 shows the spectra of the pressure signal sampled at x/c = 0,60. For all the actuation cases, a frequency bump is formed in the range of 130 to 170 Hz, corresponding to the shear layer instability, as reported by the

numerical simulations [52]. In order to analyse the fluid-structure interaction and to investigate whether the piezoelectric actuation was acting on the prototype structure, an experimental campaign was carried out using an accelerometer placed at x/c = 0,85. The spectra of acceleration output and unsteady pressure signals from the sensors located at x/c = 0,60 and 0,85 are seen together on Figure 5.6. One can observe that sensor 3 is sensitive to the proper mode located at 17 Hz, mostly due to its proximity to the accelerometer. No other peak seems to be related to mechanical vibrations, even so another approach was employed to verify it. The cross-correlation between the accelerometer and the pressure sensors signals was computed (Figure 5.7). The normalized cross-correlation coefficient has small values on both cases analyzed. It indicates that pressure signals have low interference coming from mechanical vibration from the prototype.

By analyzing the cross-correlation values the following result was noticed: the value of the coefficient is superior for the sensor placed at x/c = 0,60 even if it is more far from the accelerometer. To better understand the reason, the time signals were displayed on Figure 5.8. While a small phase shift occurs between acceleration and pressure signals at x/c = 0,60, there is a phase opposition at x/c = 0,85. This behaviour indicates that pressure transducers outputs are not biased by mechanical vibrations.

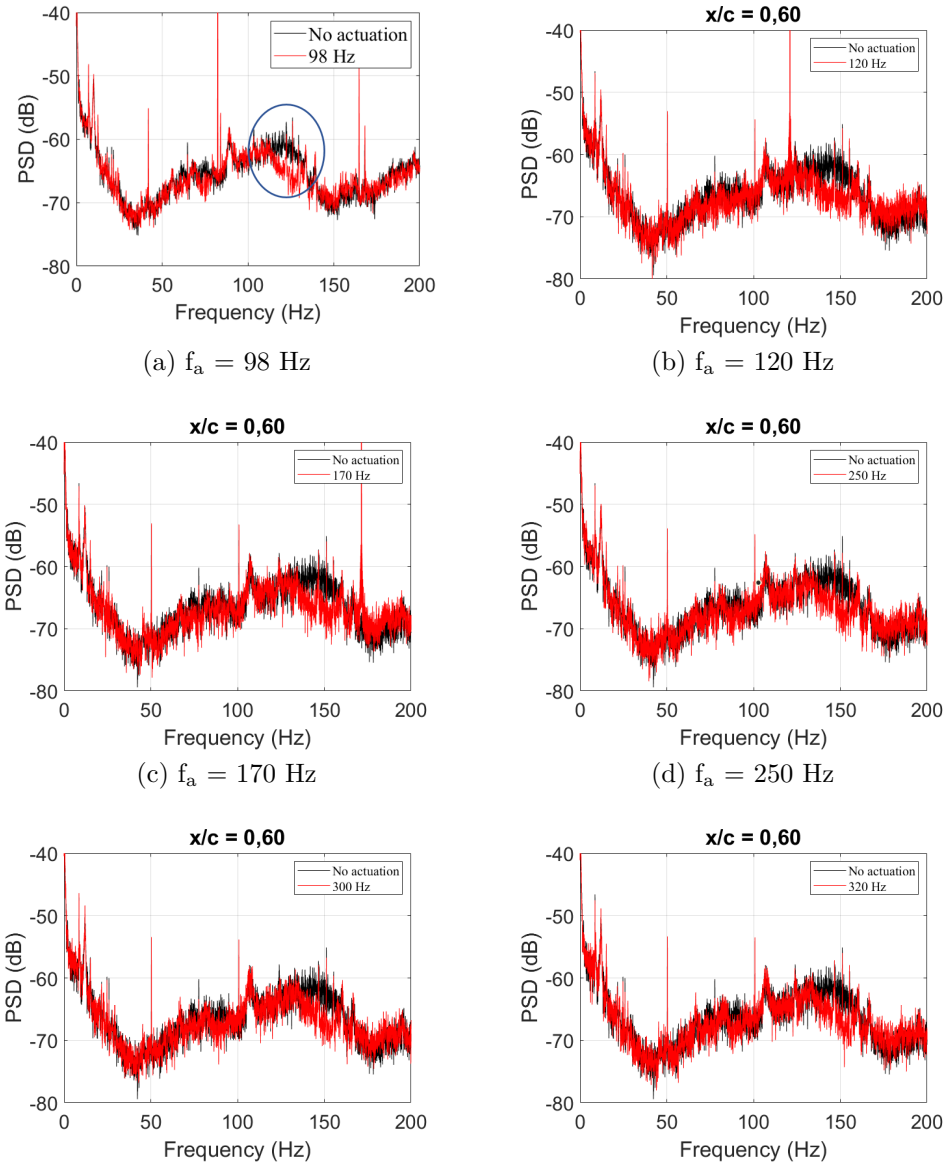

(a) f_a = 98 Hz (b) f_a = 120 Hz

(c) f_a = 170 Hz (d) f_a = 250 Hz

(e) f_a = 300 Hz (f) f_a = 320 Hz

Figure 5.5: Spectra of unsteady pressure signals.

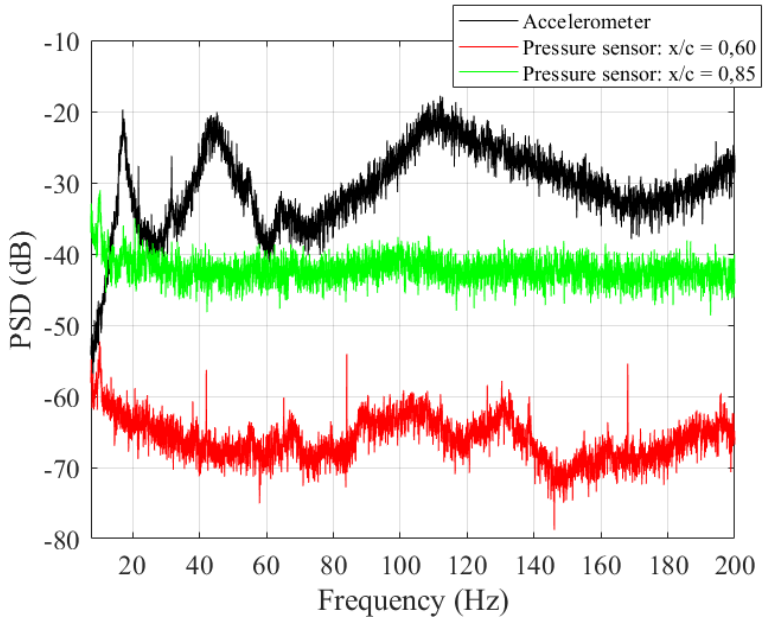

Figure 5.6: Superposition of acceleration and unsteady pressure spectra.

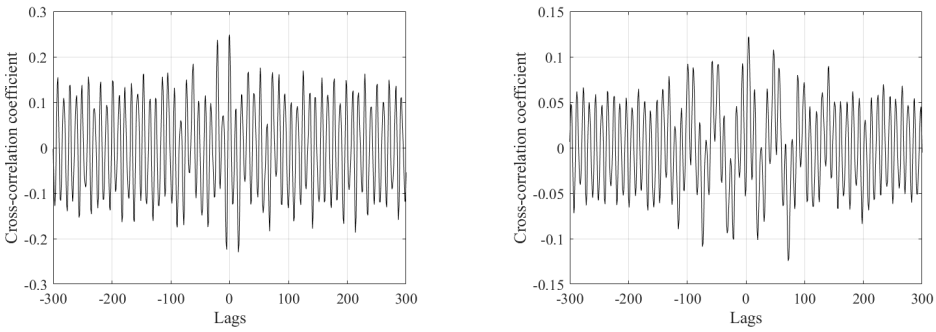

(a) x/c = 0,60 (b) f_a = 12 Hz

Figure 5.7: Cross-correlation between acceleration and unsteady pressure outputs.

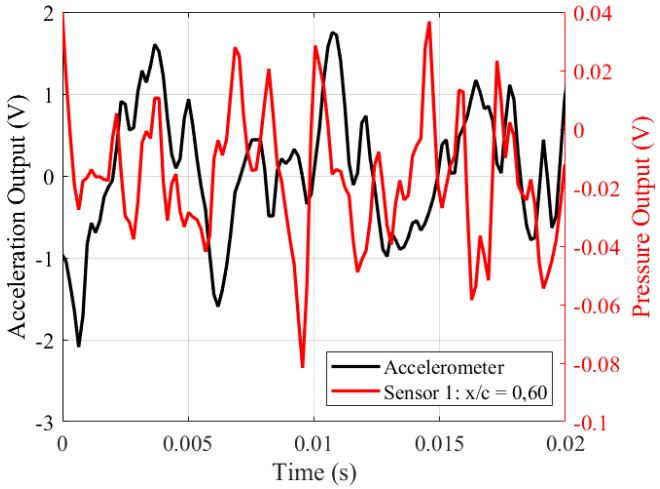

(a) x/c = 0,60

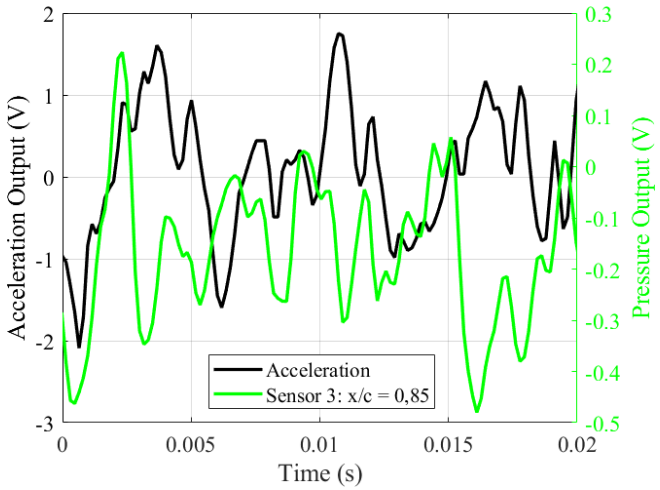

(b) x/c = 0,85

Figure 5.8: Output signals from accelerometer and pressure sensors.

5.2 Time-Resolved Particle Image Velocimetry (TRPIV): trailing edge piezo-actuation

5.2.1 Experimental set-up

The interrogation window was placed downstream of the trailing edge to investigate the dynamics of the shear layer. For image acquisition, a LaVision camera model V2012 was used with a sampling frequency of 10 kHz and a duration of 20 seconds. Reynolds number is 700,000. Full image size is 1200 x 800 pixels and each element used for the correlation is 16 x 16 pixels. For post-processing of data, the LaVision software DaVis and Matlab were used. Figure 5.9 shows the experimental set-up used for this campaign.

(a)

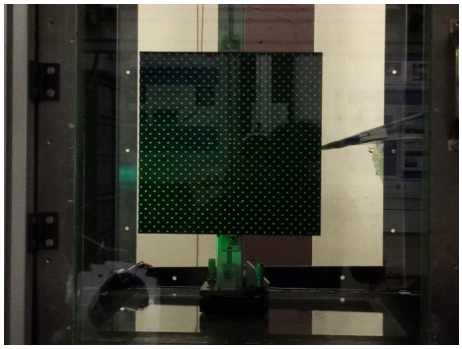

(b)

(c)

Figure 5.9: Experimental set-up of the TRPIV campaign.

5.2.2 Time-averaged velocity fields

Near to 200k snapshots were averaged to generate the mean velocity fields, ensuring converged statistics. These fields are displayed displayed in Figure 5.10. Two actuation frequencies, f_a = 100 Hz and 170 Hz, are analyzed together with the non-morphing case. The two velocity components, V_x and V_y, were used to computed the velocity magnitude. By looking at the V_x fields, one can see a reduction of the velocity inside the shear-layer once HFVTE actuation takes place along with the appearance of a low velocity zone in the bottom of the interrogation window. The V_y fields show that piezoelectric actuation changes the flow dynamics in the wake of the wing: once f_a = 100 Hz, it elongates the shear-layer, f_a = 170 Hz seems to act in the near region of the trailing edge by pushing it upwards and to slightly orient the near wake downwards, as seen by the velocity magnitude iso-contours.

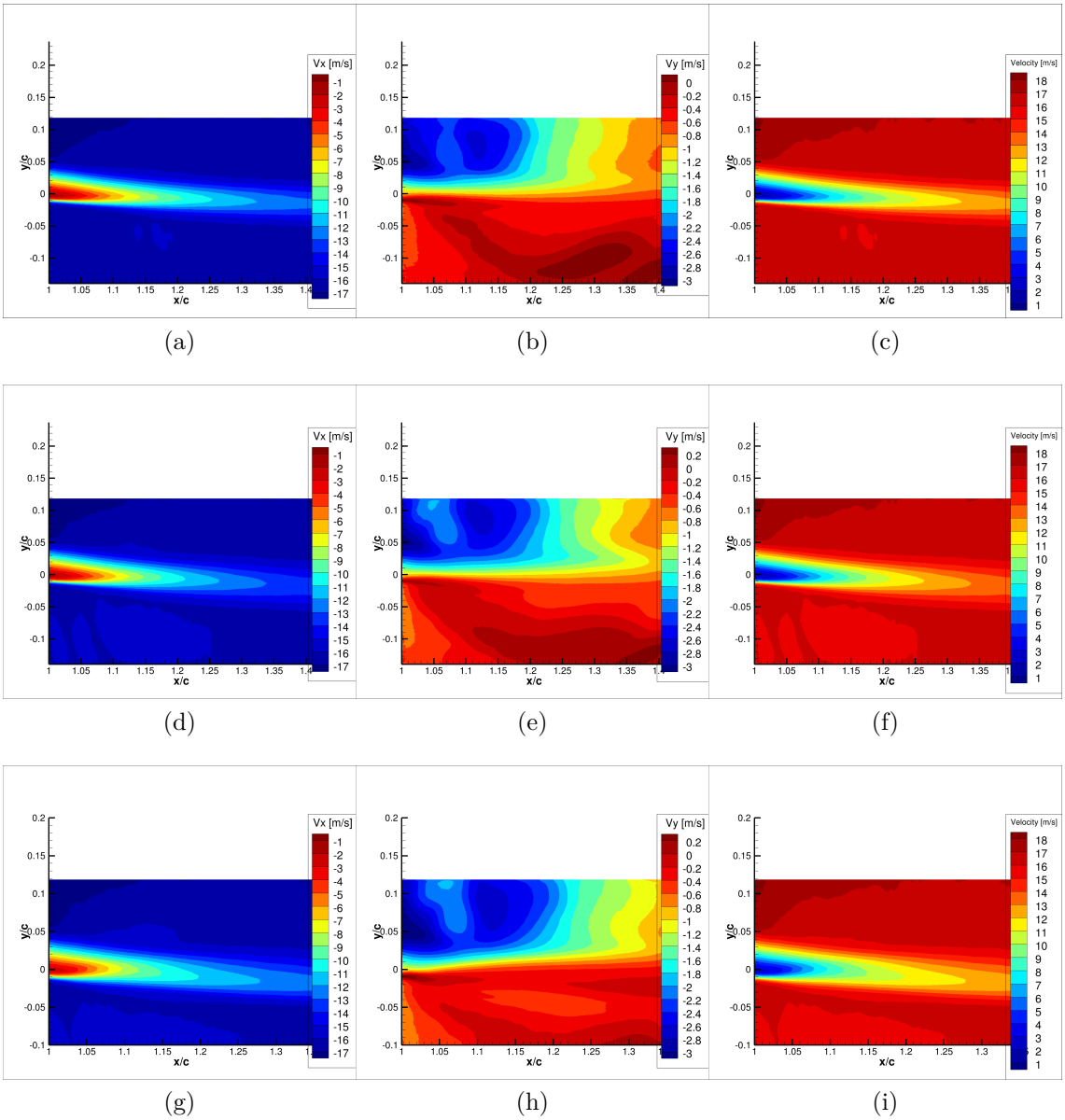

Figure 5.10: Time-Averaged velocity fields. Each row corresponds to one actuation frequency: 0, 100 and 170 Hz. First column: V_x; Second column: V_y; Third column: Velocity magnitude.

The profiles of the horizontal component of the flow velocity are shown in Figure 5.11 to analyze the influence of HFVTE on the shear layer. Four sections of the TRPIV window were chosen: x/c = 1,02, 1,13, 1,20 and 1,34. It is confirmed that the actuation frequency at f_a = 170 Hz induces a remarkable reduction of V_x near the trailing edge. This reduction is even clearer at x/c = 1,13 and 1,20 if compared to the reference case. At x/c = 1,34 an interesting phenomenon takes place once we see that the reduction of V_x is strongest for f_a = 100 Hz instead of 170 Hz (Figure 5.12). It can be related to the shear-layer dynamics seen in the mean velocity fields, especially in the V_y component. Numerical simulation results from Marouf [53] have shown that the flapping of the trailing edge at certain frequencies generates smaller vortex in the lower shear layer that are mixed with the existing coherent shear-layer vortex farther downstream. This interaction reinforces the vortex turning in the same sense as the actuation ones and produces vortex breakdown of those turning in opposite side.

These results are consistent with previous morphing studies of Jodin [54] and Sheller [31] at lower Reynolds number regarding the wake dynamics submitted to higher frequency vibration of the trailing edge. These studies show that actuation frequencies near the von Kármán shedding frequency induces resonance phenomena. In the next sections spectral analyzes will be presented in order to identify the natural frequencies of the main coherent structures present in the flow.

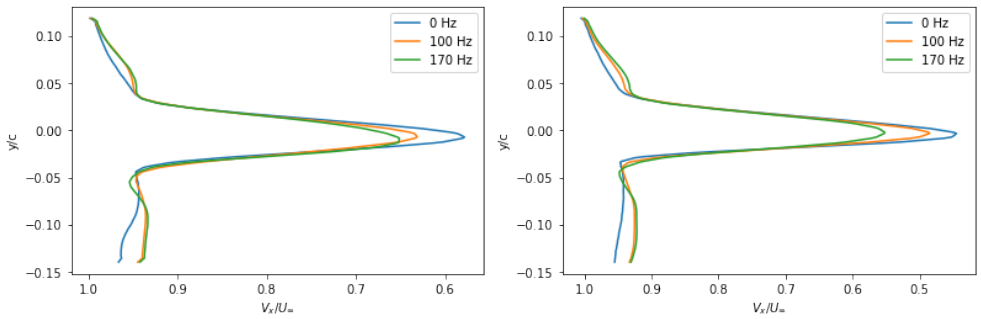

(a) x/c = 1,02

(b) x/c = 1,13

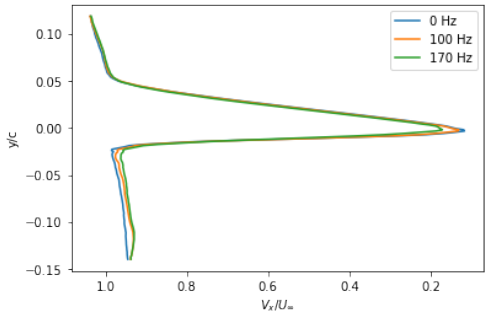

(c) x/c = 1,20

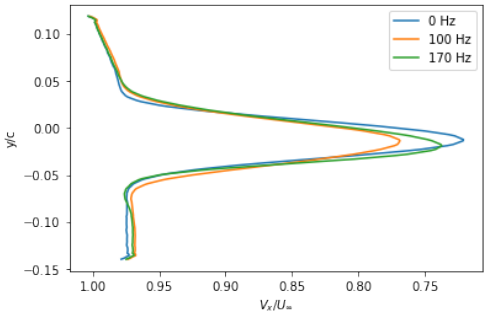

(d) x/c = 1,34

Figure 5.11: V_x profiles at four different sections of the wake flow.

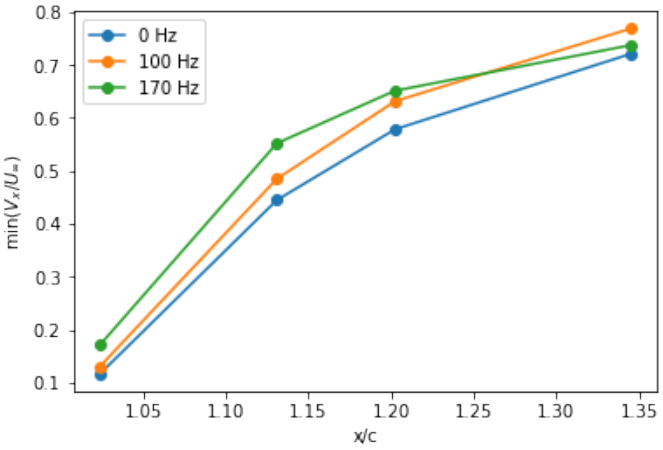

(a) Minimum values of horizontal component of the velocity inside the shear layer. The points correspond to the peaks seen in Figure 5.11 for each actuation frequency tested.

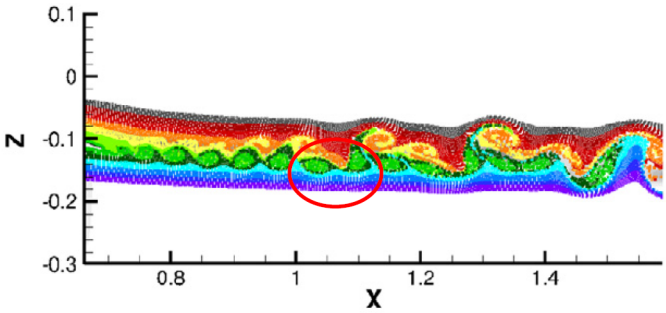

(b) Numerical simulation result of shear layer dynamics for HFVTE actuation at 300 Hz and Re = 1M [50].

Figure 5.12: Non-linear behavior of the shear layers by delaying the shedding frequency and creating Kelvin-Helmholtz vortex merging, leading to the von Kármán mode farther downstream.

5.2.3 Proper Orthogonal Decomposition (POD) analysis

The POD was used to investigate how the high frequency vibration of the trailing edge acts on flow dynamics. As a first step, the energy of the modes was computed for each actuation frequency and compared to the reference case. The result can be seen in Figure 5.13 where the first mode corresponds to the mean velocity of the flow.

A remarkable effect is noticed on modes 2 and 3, HFVTE actuation increases the energy of the first pair of modes. In Figures 5.14 and 5.15, the spectra of the temporal coefficient of these modes show peaks generated by morphing at the same frequency of the trailing edge actuation frequency. This frequency range corresponds to shear layer vortex as seen in the spectrum of the reference case. It indicates that HFVTE actuation near the natural frequency of shear layer instabilities breaks high energy coherent structures in the wake of the wing. The spectra of temporal coefficients in Figure 5.16 illustrate this phenomenon. The natural frequency of von Kármán shedding is displaced towards the frequency of the flapping while the energy of these instabilities is reduced. Moreover, closer is the actuation frequency to natural frequency of shear layer vortex, more efficient is the energy attenuation.

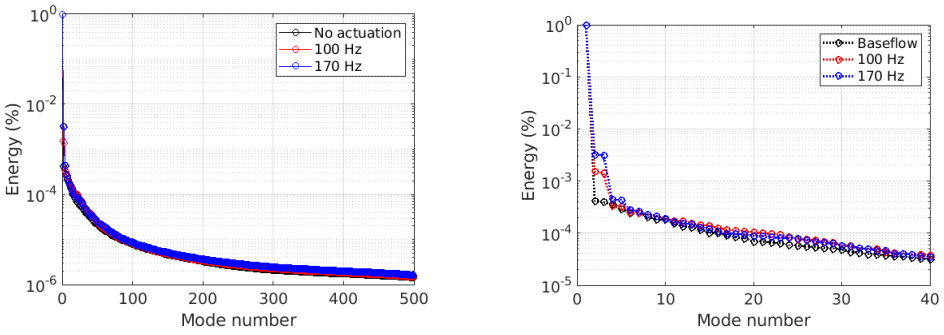

(a) (b)

Figure 5.13: Distribution of POD modal energy.

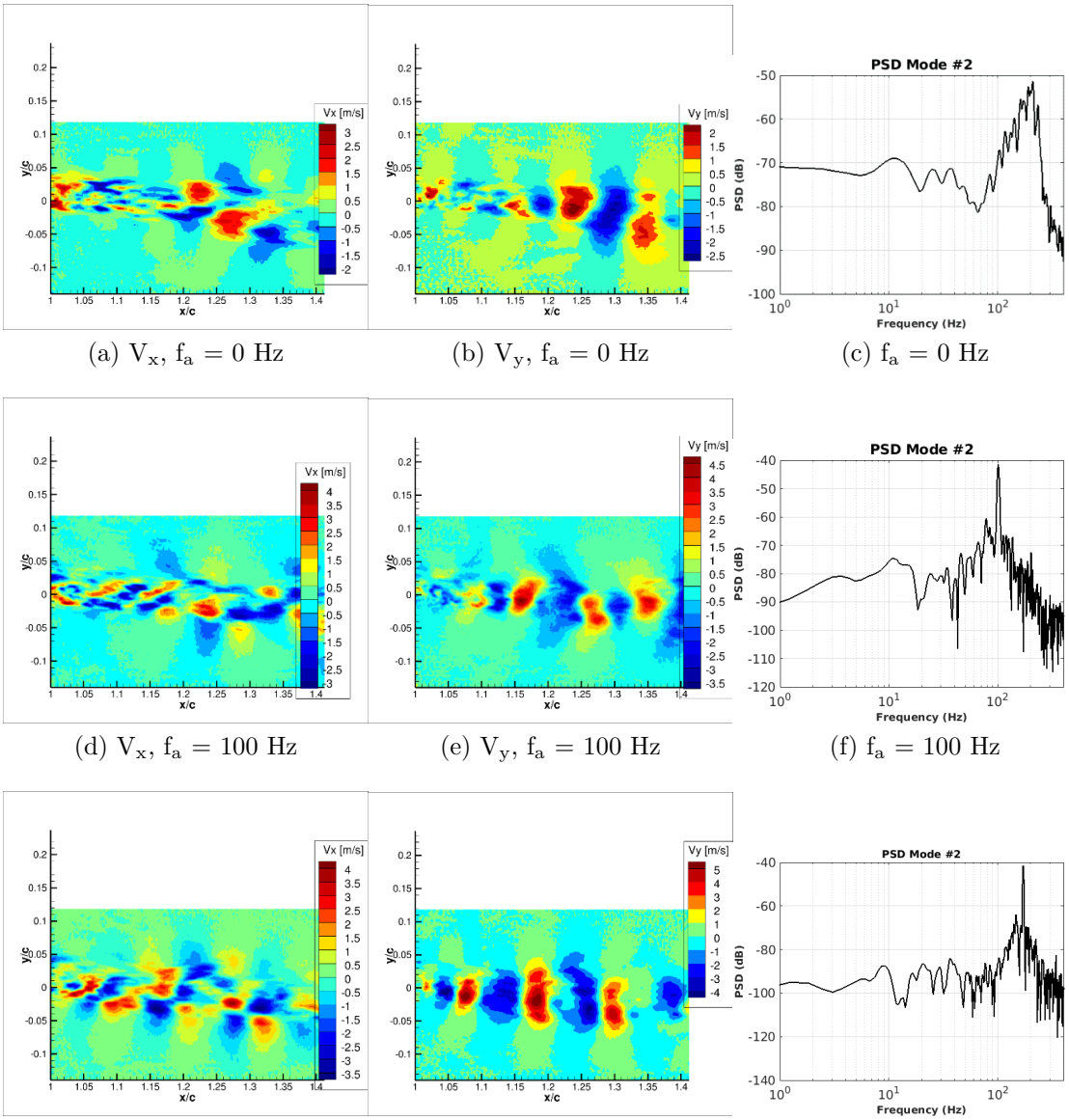

(a) V_x, $f_a = 0$ Hz (b) V_y, $f_a = 0$ Hz (c) $f_a = 0$ Hz

(d) V_x, $f_a = 100$ Hz (e) V_y, $f_a = 100$ Hz (f) $f_a = 100$ Hz

(g) V_x, $f_a = 170$ Hz (h) V_y, $f_a = 170$ Hz (i) $f_a = 170$ Hz

Figure 5.14: POD mode 2.

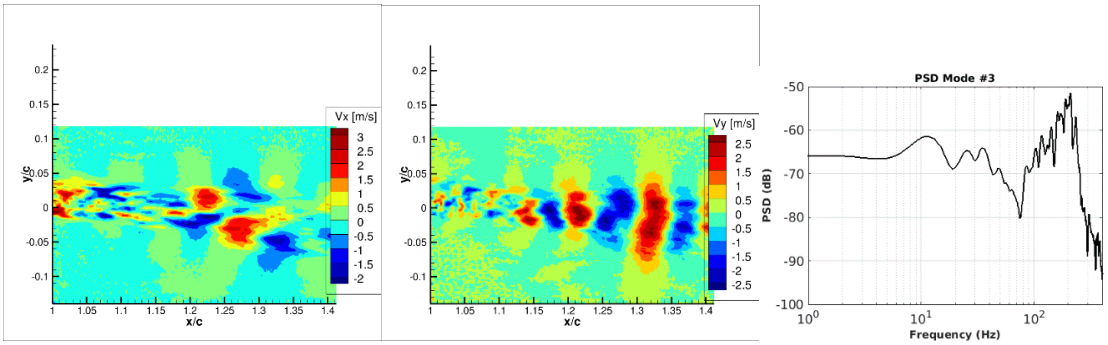

(a) V_x, $f_a = 0$ Hz (b) V_y, $f_a = 0$ Hz (c) $f_a = 0$ Hz

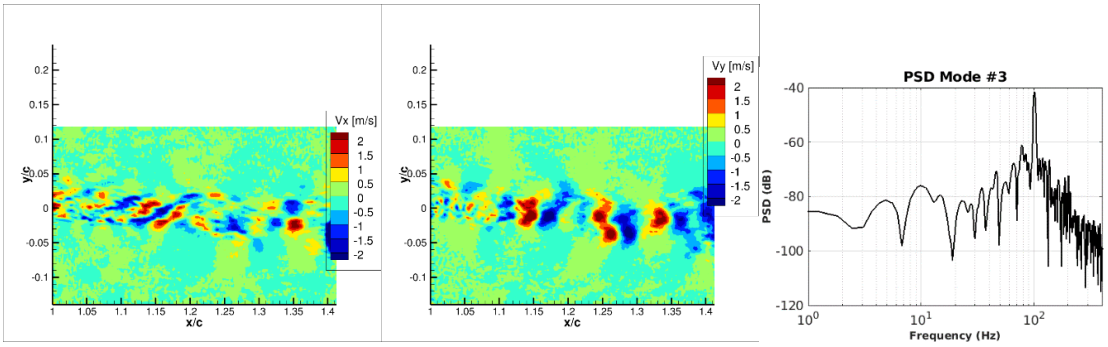

(d) V_x, $f_a = 100$ Hz (e) V_y, $f_a = 100$ Hz (f) $f_a = 100$ Hz

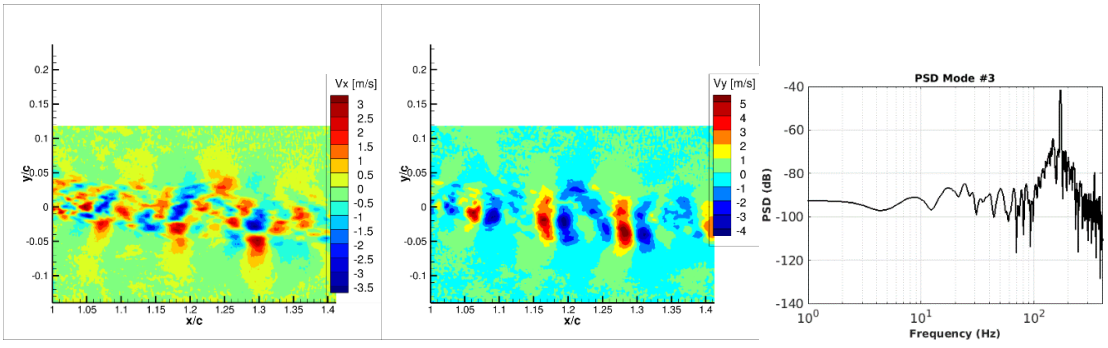

(g) V_x, $f_a = 170$ Hz (h) V_y, $f_a = 170$ Hz (i) $f_a = 170$ Hz

Figure 5.15: POD mode 3.

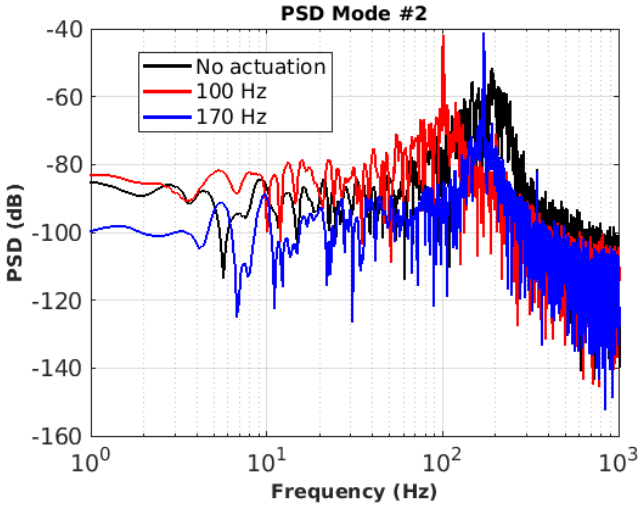

(a) Mode 2

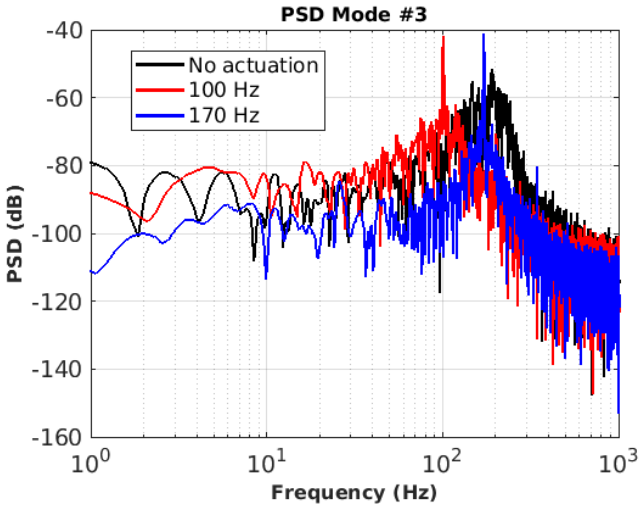

(b) Mode 3

Figure 5.16: Spectra of temporal coefficients.

Another interesting region worthy of analysis is the range between modes 15 and 30. After the effects described in the previous paragraph, the mode energies superpose quite well up to mode 15. For higher modes, energy increases in the morphing cases. The same approach for the analysis is used and the spectra of mode 24 were computed to understand this phenomenon (Figure 5.17). This mode is related to higher frequency structures of the shear layer and the comprehension of their dynamics requires more effort. The spectra show that high frequency actuation at $f_a = 100$ Hz increases the energy of the power spectrum around 300 Hz while $f_a = 170$ Hz seems to reinforce lower frequency vortex. We can relate this phenomenon to the reduction of the shear-layer observed previously in this section. Figure 5.18 shows damping of the reference spectrum at its natural frequency on both actuation cases due to the formation of higher frequency structures.

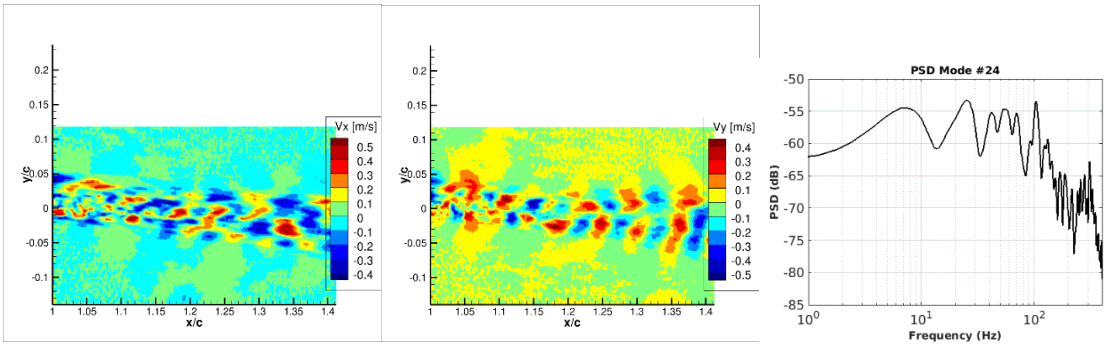

(a) V_x, $f_a = 0$ Hz (b) V_y, $f_a = 0$ Hz (c) $f_a = 0$ Hz

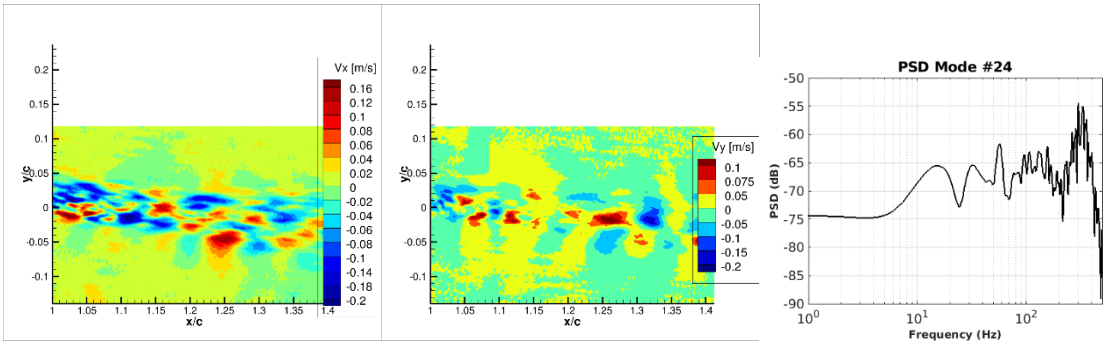

(d) V_x, $f_a = 100$ Hz (e) V_y, $f_a = 100$ Hz (f) $f_a = 100$ Hz

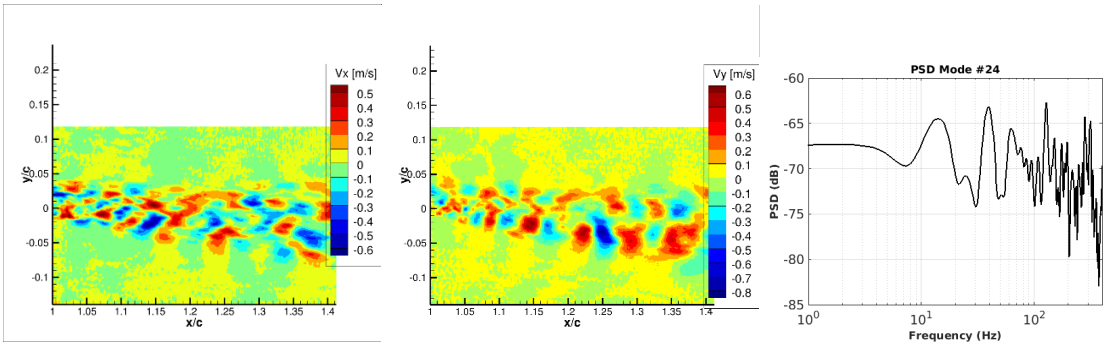

(g) V_x, $f_a = 170$ Hz (h) V_y, $f_a = 170$ Hz (i) $f_a = 170$ Hz

Figure 5.17: POD mode 24.

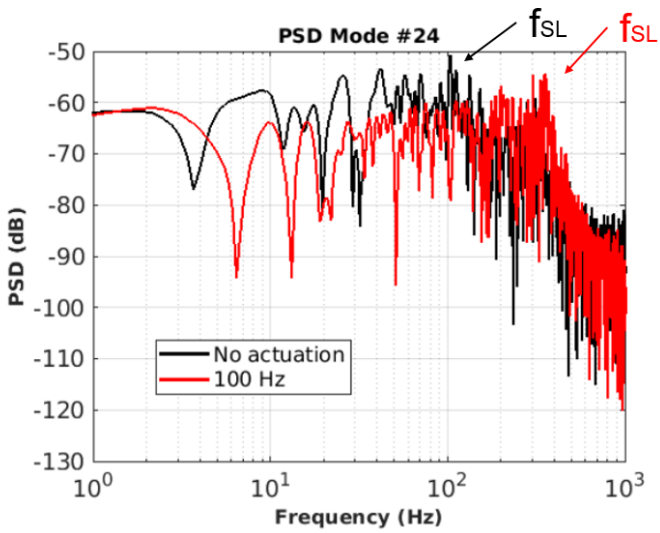

(a)

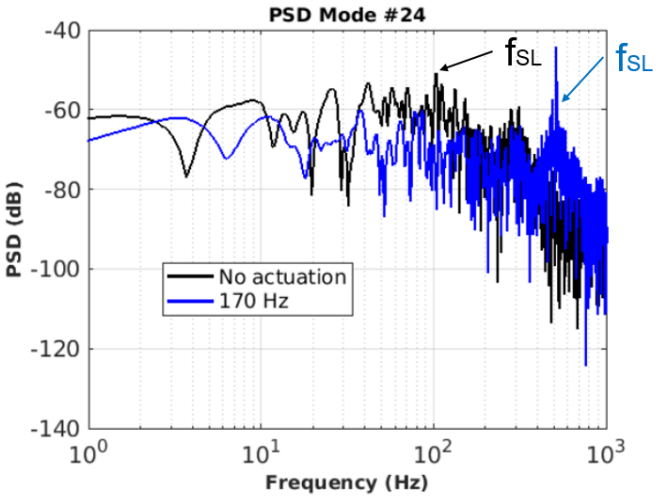

(b)

Figure 5.18: Superposition of the spectra of temporal coefficients from mode 24.

From mode 150 and onwards, the morphing increases the energy of the temporal coefficients. These modes are linked to high-frequency and low-energy vortex formed inside the shear layer. Figure 5.19 shows the energy distribution of low energy modes and the spectrum of the temporal coefficient of mode 347, located in this range. As it was expected, the spectra show the presence of coherent structures with higher natural frequencies and their harmonics. One possible reason for the rise of energy in this range of modes is the formation of these smaller-scale vortex due to morphing.

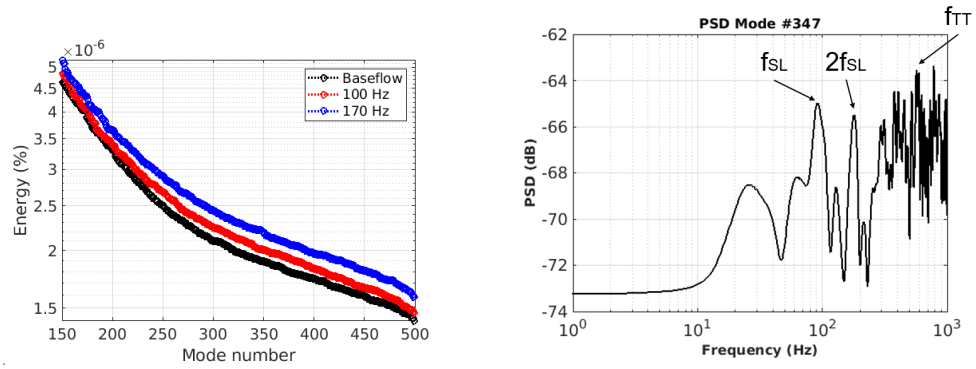

(a) Energy distribution of high order modes.

(b) Spectrum of temporal coefficient from mode 347.

Figure 5.19: POD reconstruction from high order modes shows the reinforcement of vortex formation in the turbulent/turbulent interface.

High energy modes are used to reconstruct the flow fluctuating part of the flow corresponding to the smaller-scale vortex generated by the HFVTE actuation on the shear layer that give birth to von Kármán vortex farther downstream. In this way, the instabilities and vortex dynamics occurring in the turbulent/non-turbulent (TNT) interfaces are analyzed. Furthermore, this kind of reconstruction corresponds to a turbulence re-injection in the shear layers thanks to the morphing, that is a result of the eddy blocking effect, analysed numerically by Szubert et al [55]. This turbulence re-injection materialised by the present study through the morphing effects is used in recent studies of our research group to improved turbulence modelling approaches able to enhance *upscale* modes, thus increasing shear sheltering and refraining excessive turbulence diffusion due to downscale turbulence cascade hypotheses. The present study through the experimental morphing precisely

shows the ability of this higher-energy mode turbulence re-injection in the shear layers to reduce their width and the turbulence diffusion effects

Figure 5.20 shows snapshots of the velocity field reconstructed from high energy modes. Streaklines highlight the important effect of trailing edge flapping on the wake flow. An increase of vorticity can be seen, indicating that HFVTE actuation near the natural frequency of von Kármán instabilities induces resonance phenomena. Due to the flapping, the formation region of the shear layer vortex is shortened and they are formed nearer the trailing edge, as also studied in numerical simulations of our group within the SMS project [52]. While $f_a = 100$ Hz seems to break coherent structures, $f_a = 170$ Hz reinforces them. These elements are linked to the reduction of the velocity deficit previously discussed in this section. Monitor points are used to further investigate these effects. Their position is shown in Figure 5.21 and table 5.1. The corresponding spectra confirm what the streaklines show: the energy magnitude of the morphing cases is higher than the static spectrum in MP2 while it is reduced in the MP1 region. It can be explained by the increase of the vertical velocity near the trailing edge zone due to vortex formation and its attenuation farther downstream when compared to the static case.

MP	x/c	y/c
1	1,34	-0,015
2	1,13	-0,015
3	1,34	-0,035

Table 5.1: Position of monitor points.

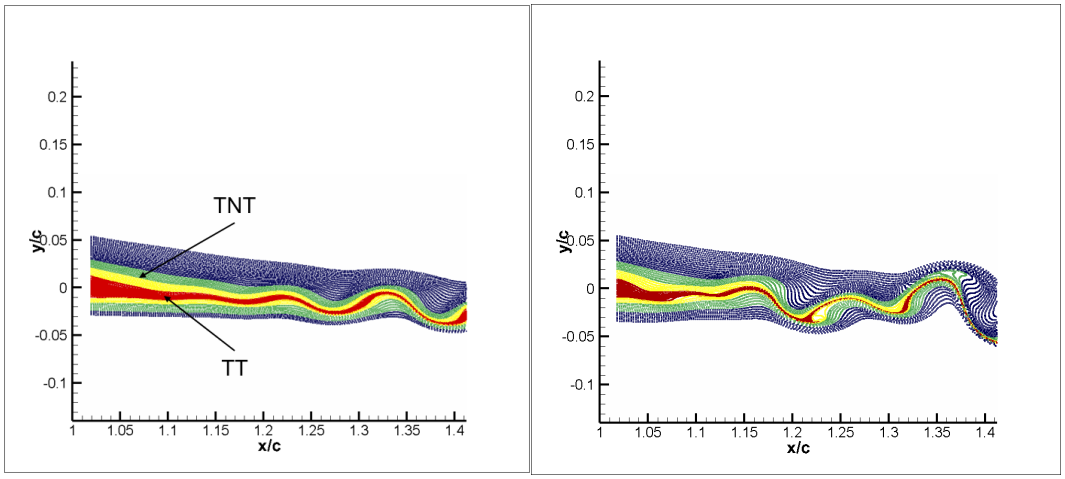

(a) $f_a = 0$ Hz (b) $f_a = 100$ Hz

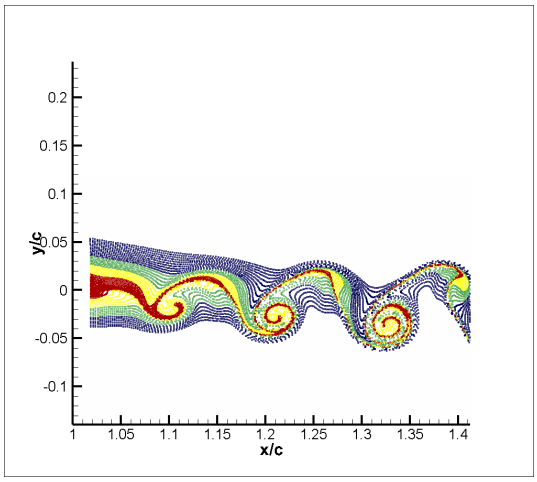

(c) $f_a = 170$ Hz

Figure 5.20: Manipulation of the turbulent/non Turbulent (TNT) interfaces interacting and modifying the turbulent/turbulent (TT) interface. Reynolds number 700,000.

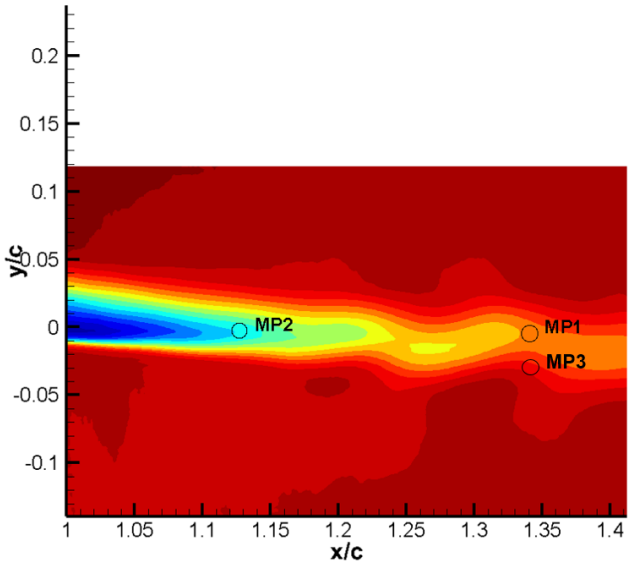

(a) Position of monitor points for spectral analysis.

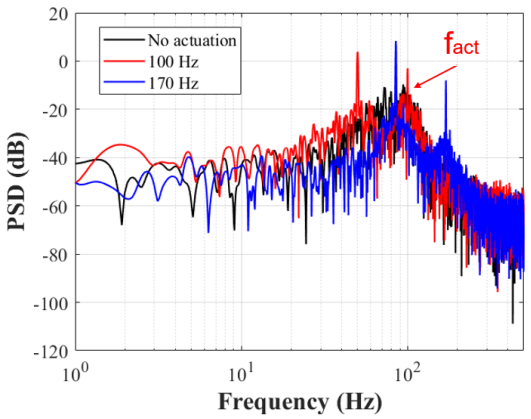

(b) MP1

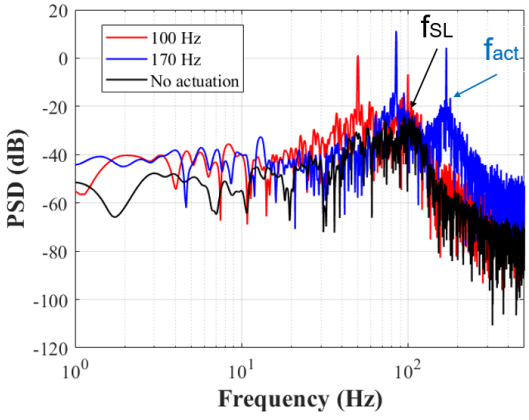

(c) MP2

Figure 5.21: Spectra of vertical velocity extracted from monitor points.

The POD reconstruction using high order modes emphasizes the effects of HFVTE on the lower shear layer. Streaklines on Figure 5.22 clearly show the morphing effect through eddy blocking in the turbulent/non-turbulent (TNT) interface dynamics. The generated smaller scale vortex act just downstream of the trailing edge along the shear layer and their manipulation begins in the near trailing edge region. Morphing acts locally but the effects propagate downstream interacting with different coherent structures naturally present in the flow. The spectrum of monitor point 3 in Figure 5.23 shows how piezoelectric actuation reduces the energy of the turbulent/non-turbulent interface. This spectrum presents attenuation of the main frequency peaks corresponding to the coherent structures and presents the effects of the vortex breakdown operated by the smaller-scale vortex generated by the HFVTE actuation. Trailing edge actuation at $f_a = 100$ Hz produces the same previously discussed non-linearity in the flow reconstructed from high energy modes, while flapping at $f_a = 170$ Hz seems to drastically change the flow dynamics by breaking the vortex seen in the static case, produced by the natural instabilities, into smaller less-energetic ones.

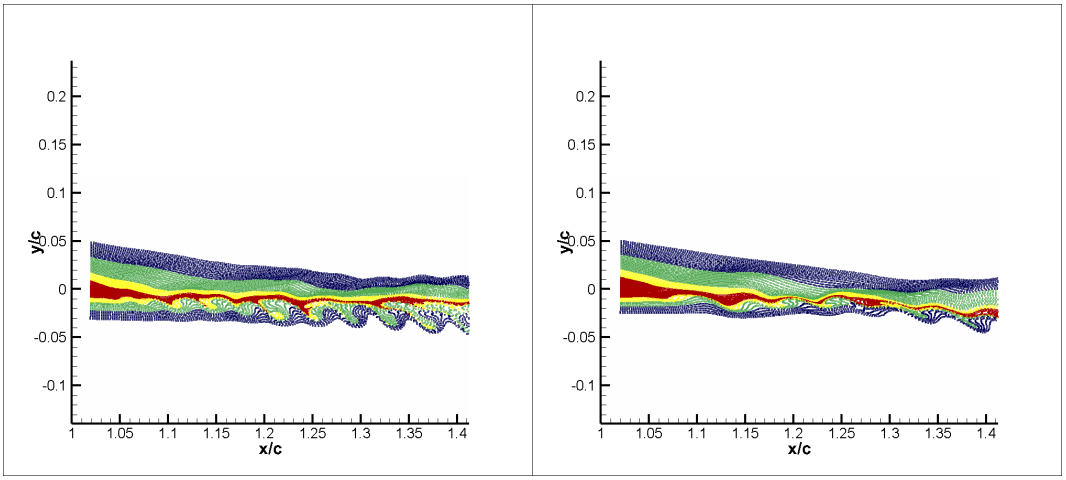

(a) $f_a = 0$ Hz (b) $f_a = 100$ Hz

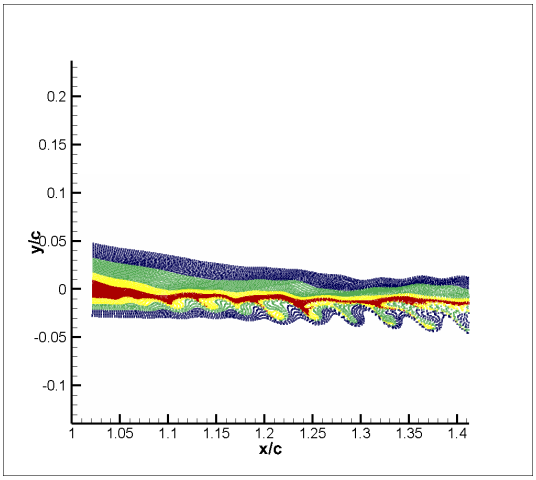

(c) $f_a = 170$ Hz

Figure 5.22: Streaklines according to POD reconstruction using high order modes.

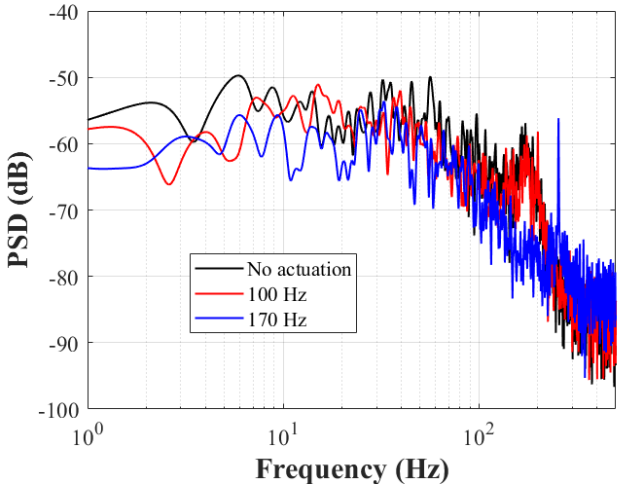

Figure 5.23: Spectrum of monitor point 3 from POD reconstruction of high energy modes.

5.3 Chapter conclusion

Spectral analysis of the lift coefficient and the unsteady pressure signals was used to study the effects of high frequency flapping of the trailing edge. Actuation is monochromatic with amplitude in the order of 0,5 mm at given frequencies chosen from previous experimental campaigns and simulation results in the SMS project. Furthermore, the present study shows the morphing effects in higher Reynolds numbers than the previous experimental campaigns. Lift measurements show that HFVTE actuation significantly attenuates spectra amplitude. Additionally, actuation frequency in the range of 100 Hz reduces the wake's width and the velocity deficit by 20% comparing to the static case, as well as the noise sources amplitude in dB by 8%. Trailing edge flapping is found to be effective to reduce aerodynamic instabilities closed to the natural frequency of von Kármán vortex, by enforcing the shear layer eddies and reducing their formation region length past the trailing edge. Unsteady pressure signals from a sensor placed near the detachment zone indicates that morphing induces important modification of flow dynamics by feedback. The frequency range concerned corresponds to shear layer instabilities. By means of detailed TRPIV measurements, spectral analysis and POD reconstruction, the eddy-blocking effect due to generation of

smaller-scale vortex past the trailing edge has been analysed and its effects to the TNT and TT interfaces thanks to the morphing have been evaluated. Moreover, cross-correlation computed between pressure and acceleration signals show that natural modes of the prototype do not compromise pressure measurements. This result is important because the closed-loop control for HFVTE actuation, which will be presented further on, is based on the variance of the pressure sensors.

Chapter 6

Hybrid morphing

6.1 Wind-Tunnel experiments

SMA and piezoelectric actuation allows us to act on two different time scales, be it in the modification of the lift/drag coefficient or in shear-layer dynamics. Therefore in accordance with the turbulence spectrum that is extended in multiple scales due to the different classes and size of the surrounding vortex. The hybrid morphing is partly bio-inspired, in the same way as large-span hunting birds do, by actuating their wings, ailerons and feathers at different frequencies, according to the pressure loads that they capture through their muscles, bones and nervous system during flight. The term of "hybrid electroactive morphing" has been first employed in the studies of the multidisciplinary research team IMFT-LAPLACE [22]. In this chapter unsteady pressure and lift signals are analysed combining camber control and HFVTE actuation. Then, a complete study from TRPIV results will be presented including time-averaged velocity fields and modal analysis.

6.1.1 Experimental set-up

The TRPIV results have been obtained thanks to the contribution of the "Signaux-Images" team of IMFT in the S4 subsonic wind tunnel. Results were obtained at Reynolds number of 700,000, which corresponds to a free stream velocity of 15,0 m/s. The prototype was mounted using the standard take-off configuration presented previously. The wind-tunnel balance used in this campaign was designed and manufactured in collaboration LAPLACE-IMFT and received the support of the "Signaux & Images" team of IMFT.

For the acquisition, a Yokogawa DL850 Oscilloscope was used. It allows us to make the zero adjustment with no need for signal conditioners and the sampling frequency goes up to 5 kHz, which is the rate used in this campaign. For post-processing, a low-pass filter was employed using Matlab, as it is going to be detailed later on.

6.1.2 Lift measurements

In this section, hybrid morphing combining open-loop actuation of the SMA and vibration of the trailing edge is investigated. HFVTE actuation is generated by three vibration frequencies f_a = 100, 170 and 300 Hz chosen from previous experimental campaigns and numerical simulations carried out in synergy with the experiments within the SMS project. In open-loop, the electric tension supplied to the SMA acts on the cambering velocity. Higher is the voltage, lower is the time needed to reach full camber position. Two cases were analyzed: the first at 30 V which gives a slow cambering (around 12 seconds) of the last 30% part of the chord's length and the second at 50 V where full camber is reached in less than 2 seconds. Figure 6.1 illustrates the actuated regions of the prototype following the flap configuration of commercial airplanes.

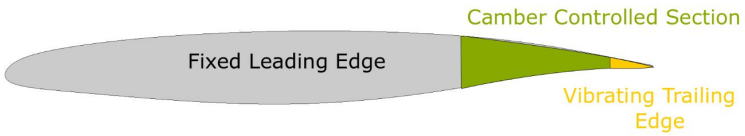

Figure 6.1: Arrangement of the actuators on the prototype used in the experiments.

Such as other instrumentation equipment, the wind-tunnel balance is sensitive to mechanical vibration coming from the trailing edge actuation. For this purpose, a low-pass filter is applied during post-processing of mean values of lift measurements to suppress the signature from the HFVTE actuation.

Figure 6.2 shows the effect of the numerical filter on the spectra of the lift signal. As it can be seen, the amplitude of the power spectrum is attenuated near the actuation frequency.

Two cases were used to analyze the effects of the hybrid morphing on the flow dynamics: slow cambering with supplied tension of 30V, where the trailing edge reaches 1,8 m/s during the descent, and faster cambering at 55V with maximum speed of displacement of 7 m/s. The performance of hybrid actuation is compared with simple SMA cambering by evaluating the mean values of the lift coefficient C_L.

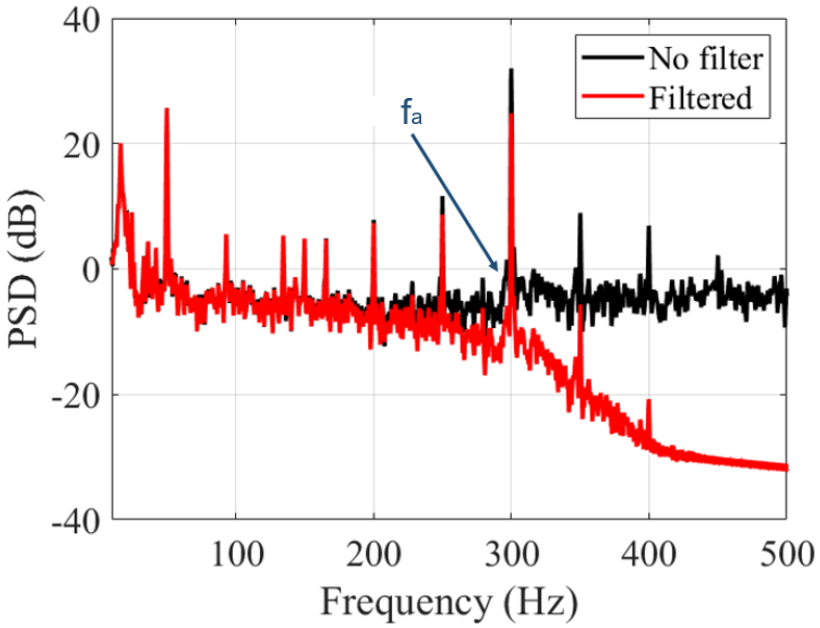

Figure 6.2: Spectra of filtered and non-filtered lift signals. Hybrid actuation at fast cambering and HFVTE actuation at 300Hz.

The lift coefficient C_L was computed from the output signal of the balance, they are displayed in figures 6.3 and 6.4. The first three cases correspond to slow SMA actuation while the three last show the results from fast cambering. To investigate the influence of HFVTE during cambering, the mean value of the C_L was calculated in the part of the signals that corresponds to full camber position. Table 6.1 shows lift increase for the three actuation frequencies of the trailing edge, indicating a positive effect obtained by applying hybrid morphing instead of simple SMA actuation. The relative gain in corresponding to the static case, (see Table 6.1) is more pronounced once the HFVTE is actuated at 100Hz on both slow and fast cambering. These results are consistent with those observed in Jodin [54] where the hybrid morphing

is found to increase by 2% the lift. By comparing the two cambering cases, a better performance is obtained once the voltage supplied to the SMA is 30V.

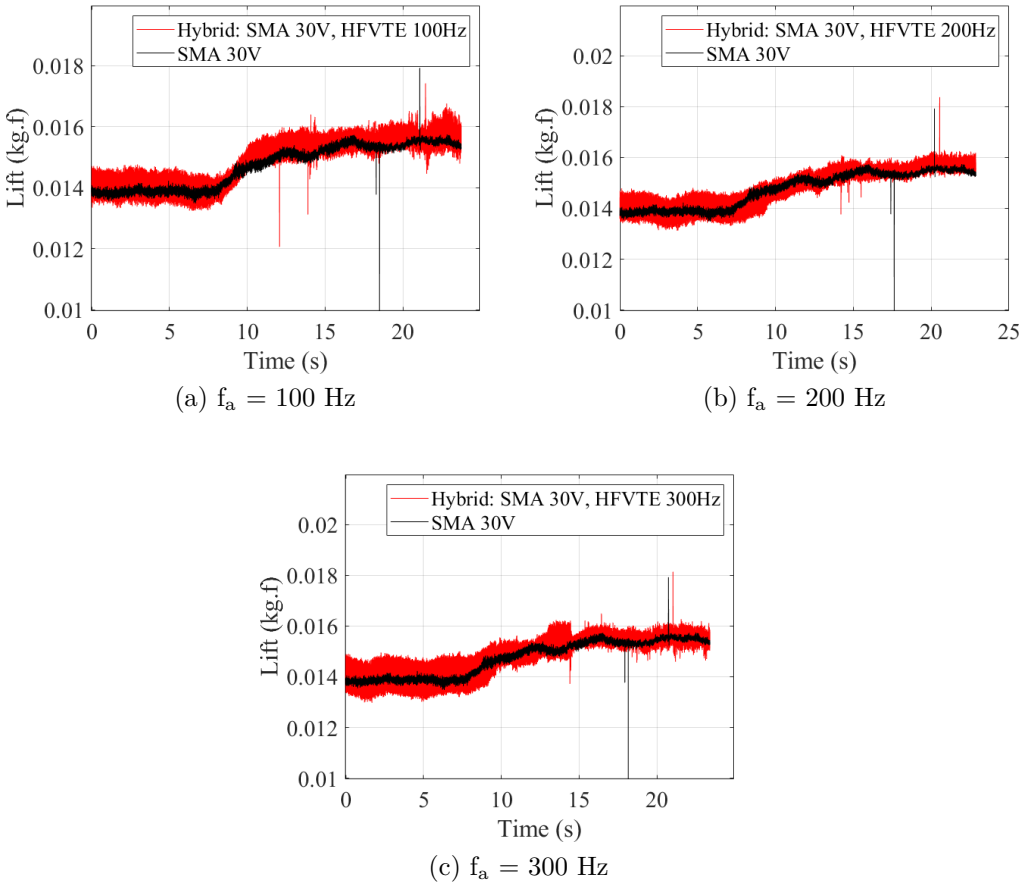

(a) f_a = 100 Hz

(b) f_a = 200 Hz

(c) f_a = 300 Hz

Figure 6.3: Lift coefficient versus time at slow SMA actuation.

The spectra of lift signals, on Figures 6.5 and 6.6, show higher amplitude on the hybrid case in the region between 10 and 20Hz. This effect can be related to the gain in lift obtained by the wind-tunnel balance. The hybrid morphing acts on the low frequency coherent structures (the von Kármán mode) reinforcing the lift force generated by them. The hybrid actuation generates in addition new predominant modes f_2 (25 Hz) and f_3 (45 Hz) due to the non-linear interaction between the cambering and the HTVE actuation. For more insight on the interaction between the higher frequency

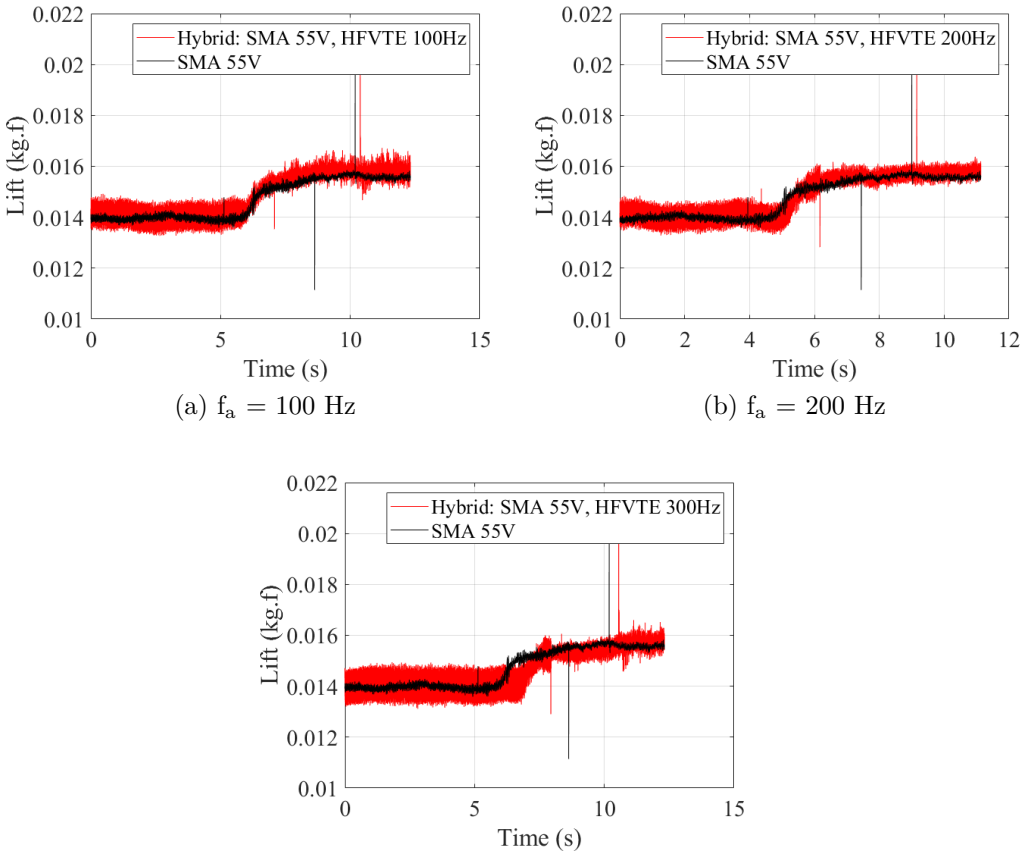

(a) f_a = 100 Hz (b) f_a = 200 Hz

(c) f_a = 300 Hz

Figure 6.4: Lift coefficient versus time at fast SMA actuation.

vibration of the trailing edge during cambering, unsteady pressure signals are analyzed.

SMA (V)	HFVTE (Hz)	Gain (%)
30	100	1,66
	200	1,01
	300	0,71
55	100	1,64
	200	0,41
	300	0,29

Table 6.1: Lift increase

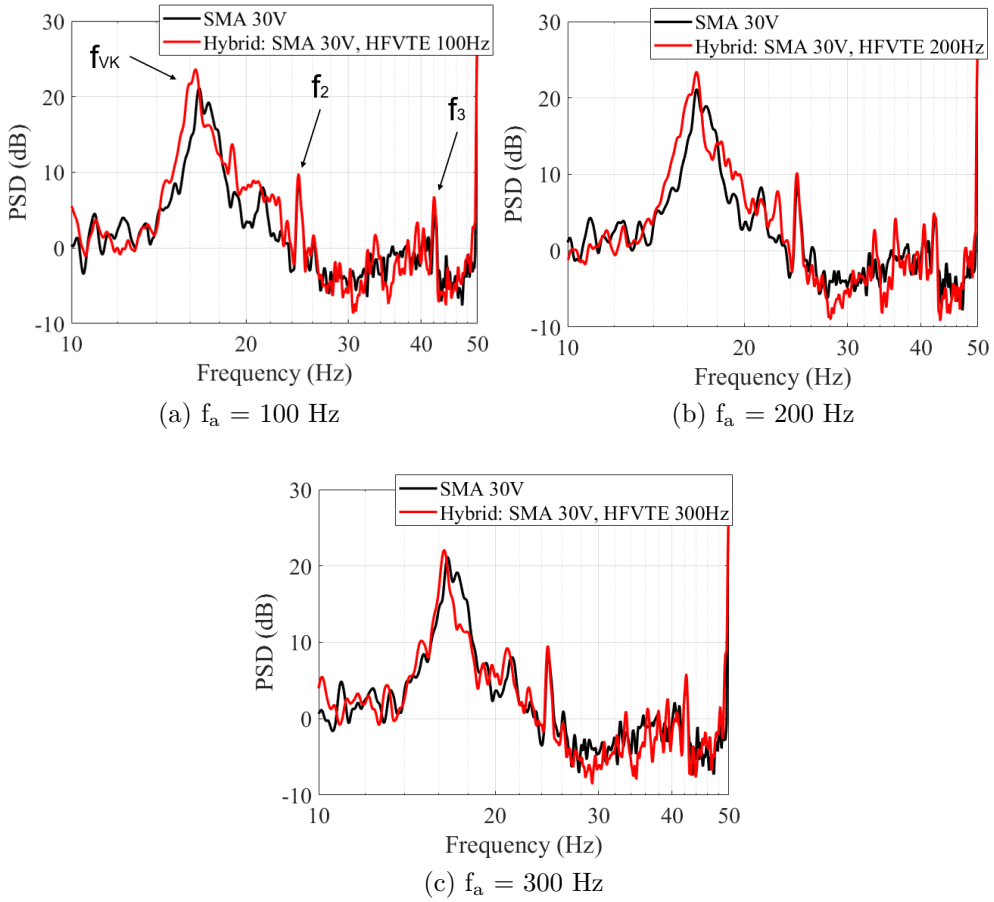

(a) f_a = 100 Hz

(b) f_a = 200 Hz

(c) f_a = 300 Hz

Figure 6.5: Spectra of lift at slow SMA actuation.

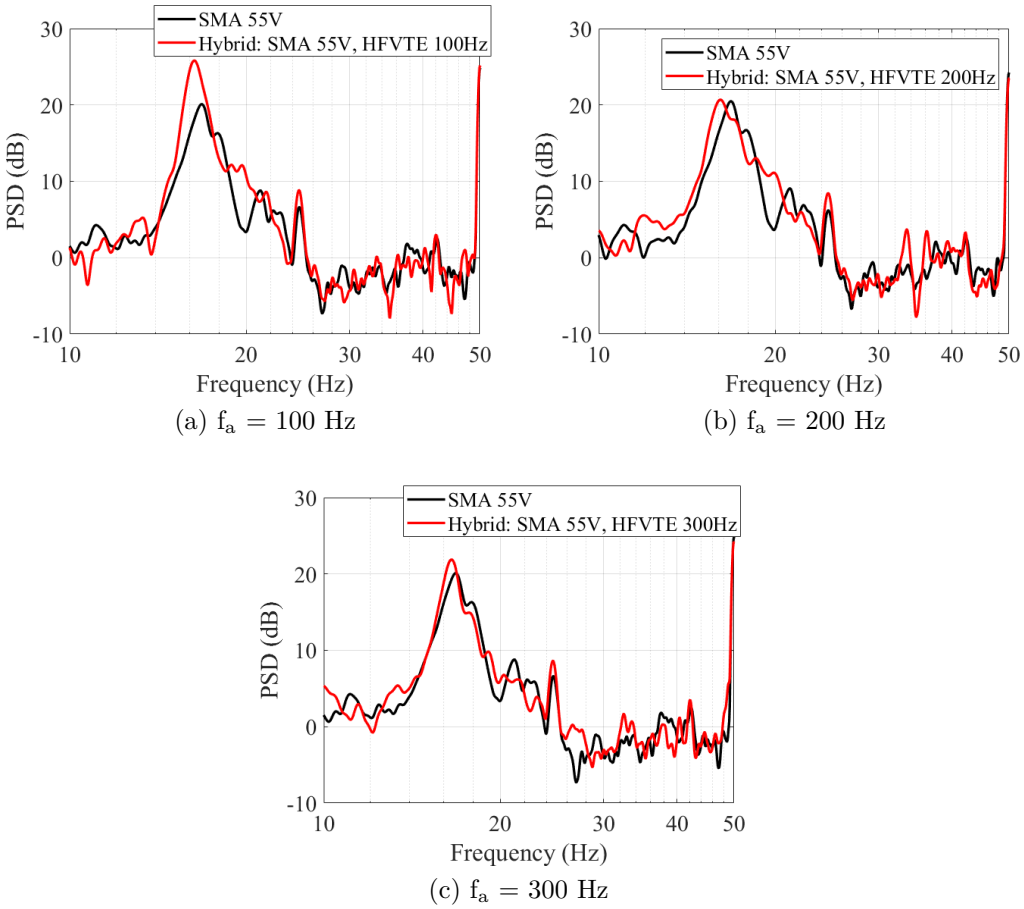

(a) f_a = 100 Hz (b) f_a = 200 Hz

(c) f_a = 300 Hz

Figure 6.6: Spectra of lift at fast SMA actuation.

6.1.3 Unsteady pressure measurements

The spectra of unsteady pressure signals also show damping in the low frequency region between 10 and 20 Hz. The hybrid morphing attenuates the amplitude of coherent structures in the area of the selected monitor point instead of reinforcing them. This phenomenon can be seen more clearly at x/c = 0,85 as shown in Figure 6.7. By using HFVTE actuation as a complement for SMA cambering, low frequency vortex are manipulated resulting in lift increase.

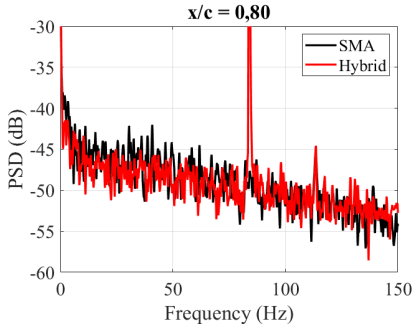

(a) SMA supplied at 30 V. $f_a = 100$

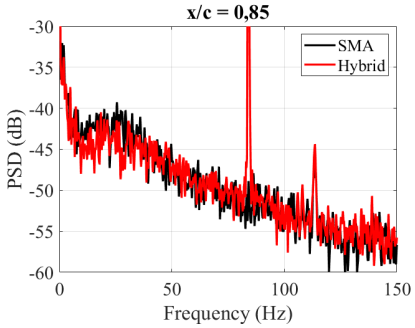

(b) SMA supplied at 55 V. $f_a = 100$

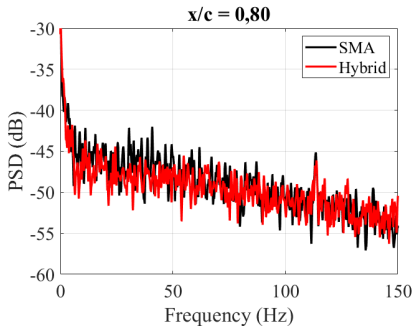

(c) SMA supplied at 30 V. $f_a = 200$

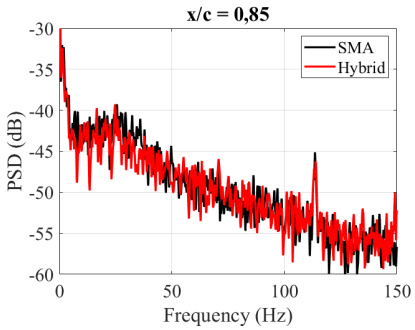

(d) SMA supplied at 55 V. $f_a = 200$

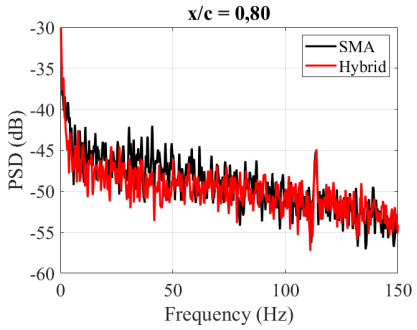

(e) SMA supplied at 30 V. $f_a = 300$ Hz

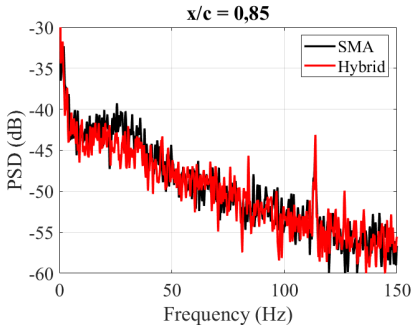

(f) SMA supplied at 55 V. $f_a = 300$ Hz

Figure 6.7: Spectra of the unsteady pressure coefficients provided by the pressure transducers.

6.2 Time-Resolved Particle Image Velocimetry (TRPIV): Hybrid morphing

6.2.1 Experimental set-up

This PIV campaign was carried out together with the one presented in the previous chapter, by using the same experimental experimental set-up. In addition to the HFVTE actuation frequencies of the last campaign, that is f_a = 100 and 170 Hz, flapping at 300 Hz was also tested because it was proven optimal by means of the numerical simulations [51]. Since the previous results indicate better performance at slow SMA actuation, only the supplied voltage at 30 V was chosen for these experiments.

6.2.2 Time-Averaged velocity fields

Due to the transient behavior of the flow during shape control, the flap descent was separated in three different steps with the same time duration and averaged to obtain the velocity fields here called: initial, intermediate and final. Given the long time to reach full camber position, the quasi-static hypothesis might be considered. Figures 1, 2 and 3 show the averaged fields of the horizontal velocity V_x, vertical velocity V_y and of the velocity vector's magnitude respectively.

As it is expected, the horizontal velocity shows the enlargement of the shear layer width during descent, which generates lift increase. At the same time one can notice a velocity reduction inside the shear layer in relation to the reference case, with no HFVTE actuation. The vertical velocity fields show that the piezoelectric actuation during the flap descent has a more important effect on the wake's turbulence, especially for f_a = 100 and 170 Hz: while the dynamics of the low pressure zone is modified in the initial averaged fields, the area corresponding to the recirculation zone is reduced when the flap approaches its final position and shape, thus reducing the velocity deficit and therefore refraining the drag increase due to the cambering.

The V_x profiles at four sections, x/c = 1,03, 1,13, 1,20 and 1,34 have been computed to provide a better understanding of the effects of hybrid morphing on the shear layer dynamics. Two sections, x/c = 1,13 and 1,20, illustrate the modification of the profiles due to HFVTE (Figure 6.11). It has been found that all the actuation frequencies reduce drastically the horizontal velocity values, thus providing less drag than the case with SMA cambering

only. A similar result was seen in the last chapter, emphasizing the important influence of piezoelectric actuation on vortex interaction. Only the minimum values of the profiles are shown in Figure 6.12 for comparison purposes. One can notice that the optimal actuation frequency changes depending on the flap position due to the transient aspect of the flow, reaffirming the potential use of a closed-loop control system for the high frequency flapping.

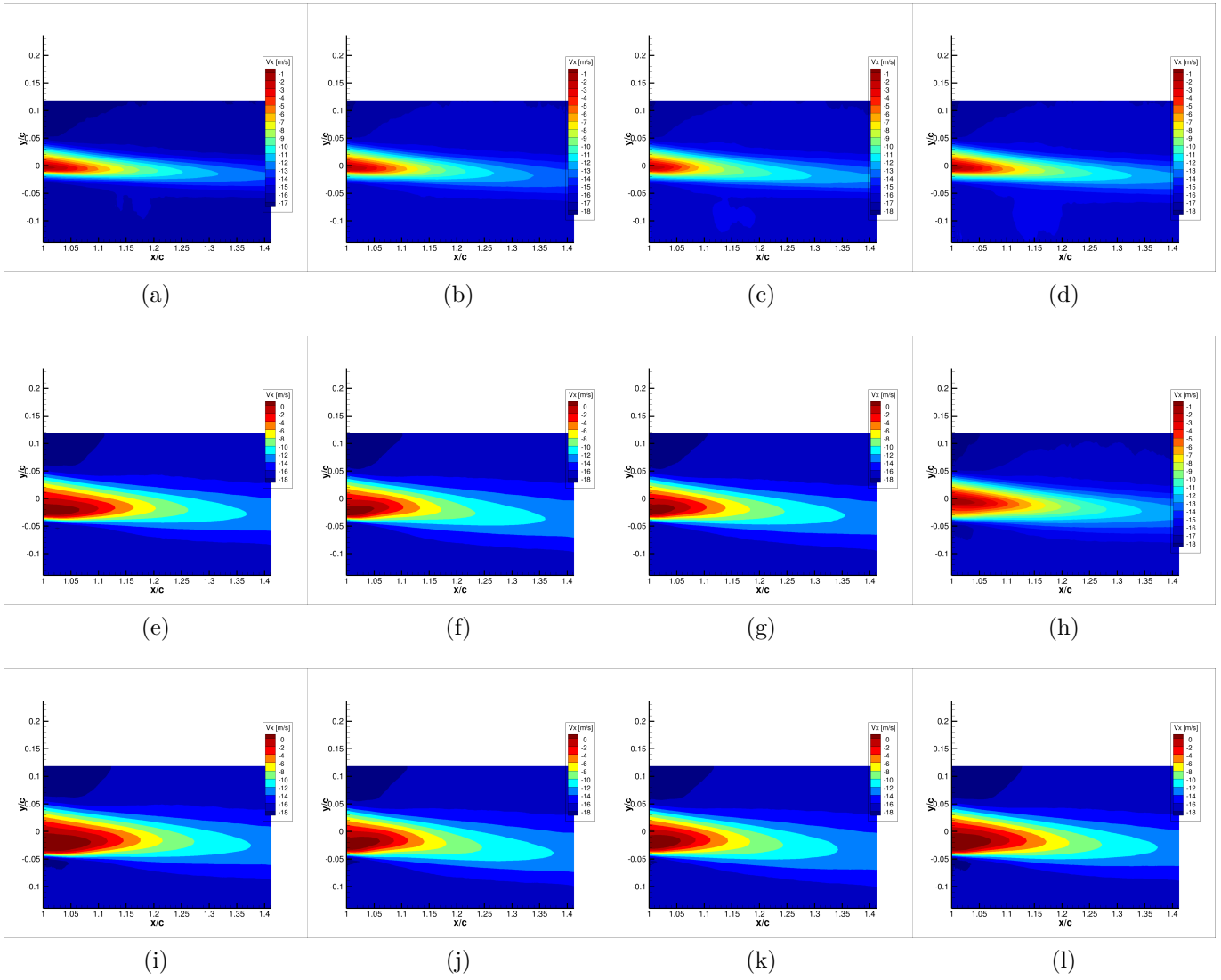

Figure 6.8: Time-averaged fields of horizontal velocity. Each column corresponds to one actuation frequency: 0, 100, 170 and 300 Hz. First row: initial position; Second row: intermediate; Third row: final.

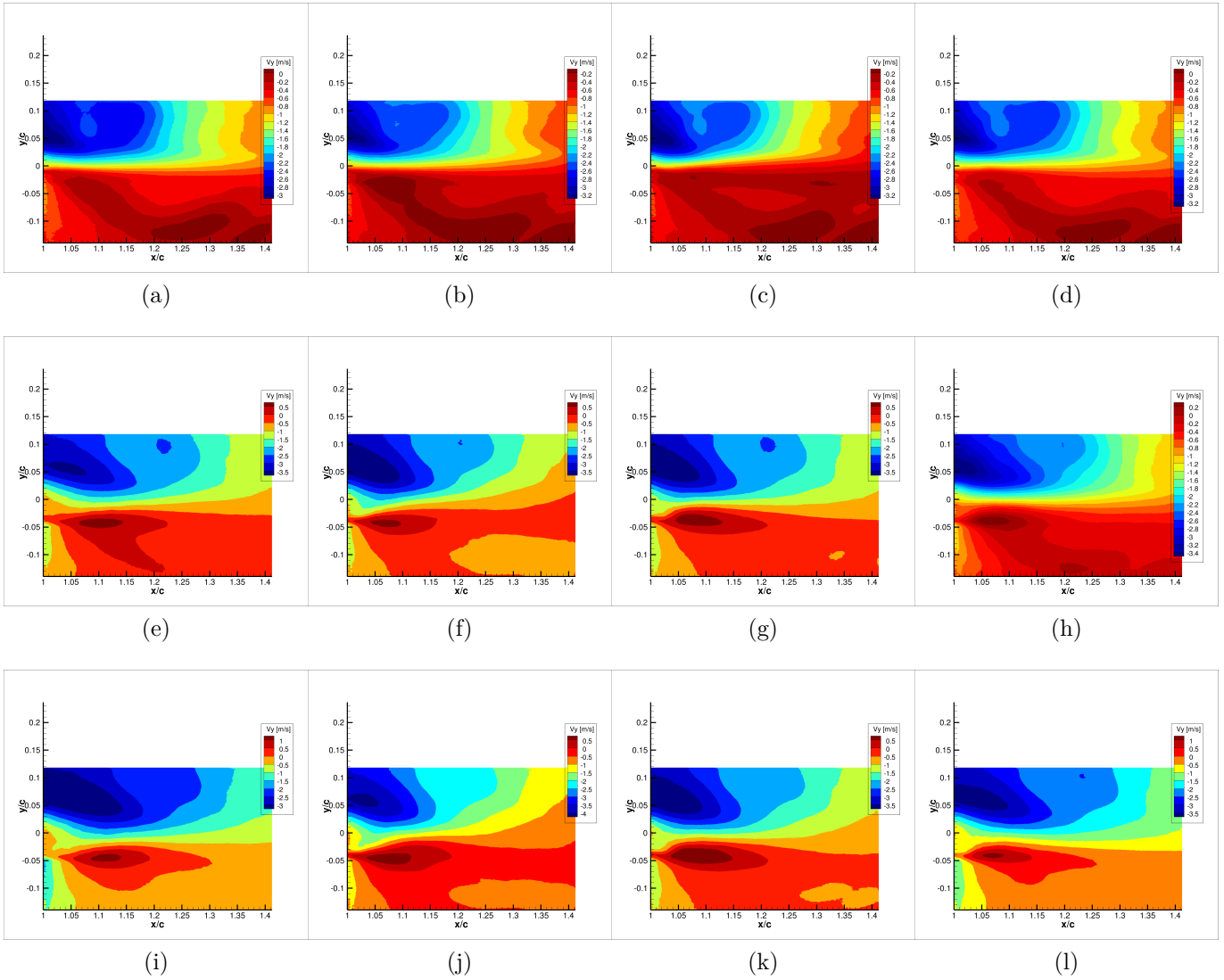

Figure 6.9: Time-averaged fields of vertical velocity. Each column corresponds to one actuation frequency: 0, 100, 170 and 300 Hz. First row: initial position; Second row: intermediate; Third row: final.

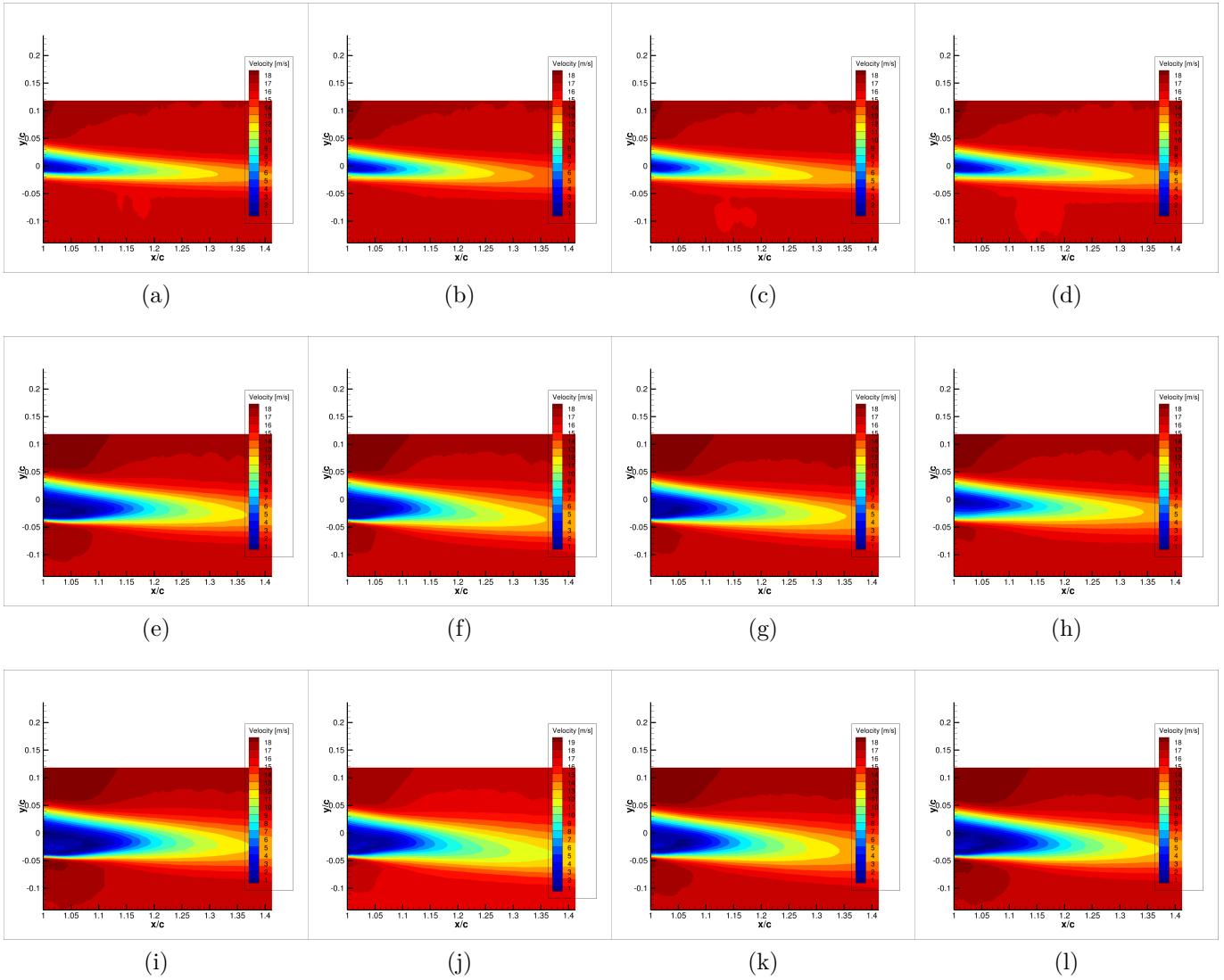

Figure 6.10: Time-averaged fields of velocity magnitude. Each column corresponds to one actuation frequency: 0, 100, 170 and 300 Hz. First row: initial position; Second row: intermediate; Third row: final.

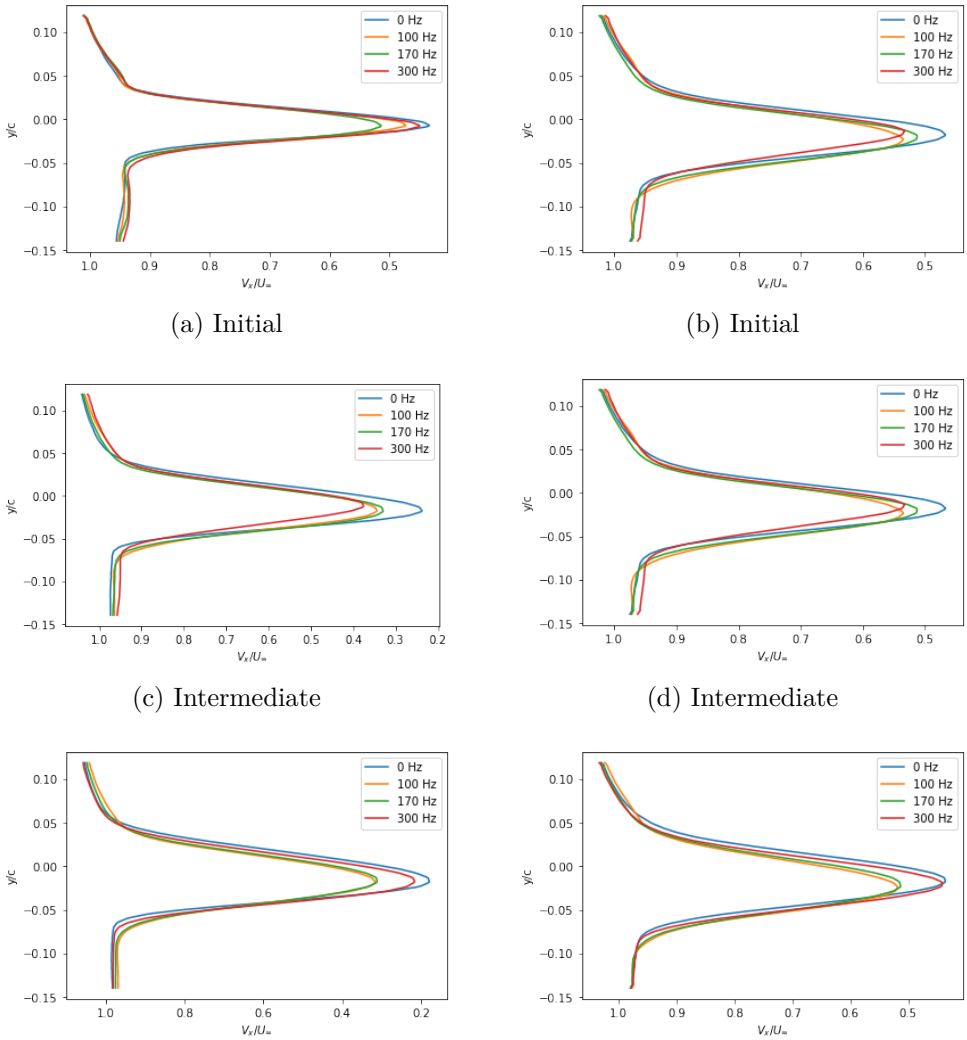

(a) Initial

(b) Initial

(c) Intermediate

(d) Intermediate

(e) Final

(f) [Final

Figure 6.11: Horizontal velocity profiles. First column: x/c = 1,13; Second column: x/c = 1,20.

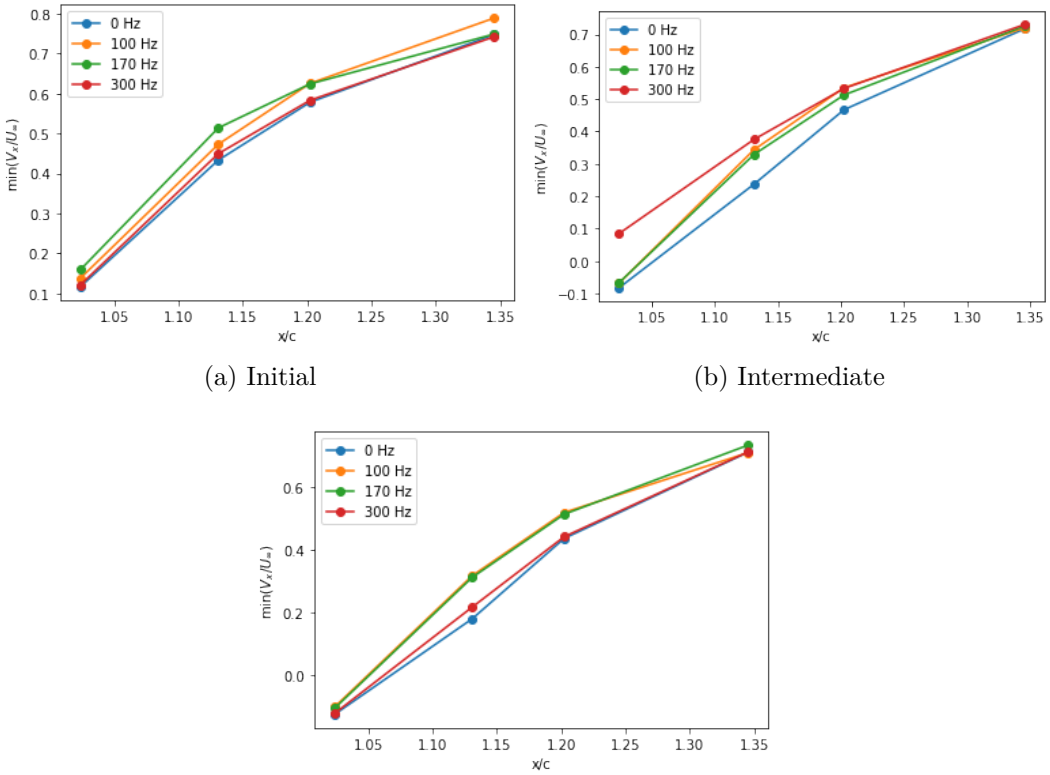

(a) Initial

(b) Intermediate

(c) Final

Figure 6.12: Minimum values of horizontal velocity.

6.2.3 Proper Orthogonal Decomposition (POD) analysis

The POD was applied on the fixed TRPIV grid despite the motion of the wing's portion throughout the whole flap descent to analyze how hybrid morphing acts globally on the SMA actuation process. The energy distribution is seen in Figure 6.13. Just as in the previous chapter, high energy modes are the most affected by piezoelectric actuation. Once more, trailing edge flapping at f_a = 100 and 170 Hz have more important effects on the flow dynamics, indicating that resonance phenomena also take place in the transient regime during cambering. These aspects are linked to the lift increase seen in this chapter, where actuation frequencies near the natural frequency

of the von Kármán instabilities have shown a better efficiency.

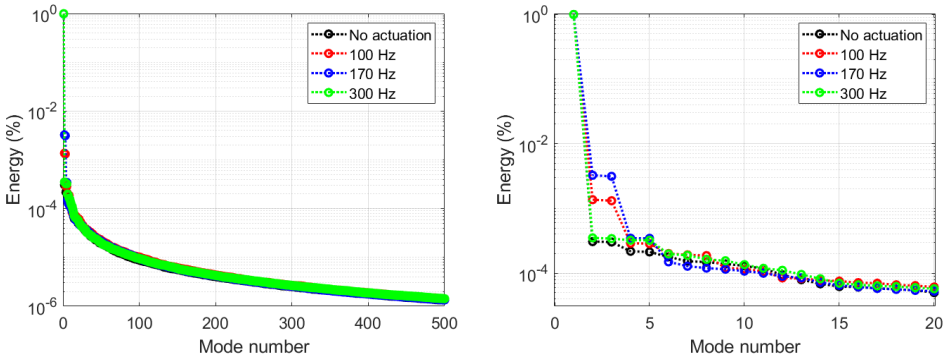

Figure 6.13: POD energy distribution.

Streaklines in Figure 6.14 illustrate how piezoelectric flapping acts on wake dynamics when the wing approaches full camber position. Resonance phenomena of the wake's turbulence are more evident at HFVTE actuation of $f_a = 100$ Hz, but $f_a = 170$ Hz also induces important modification on vortex structure. Flapping at 300 Hz seems to act mainly on the trailing edge. The increase of the recirculation zone modifies the shear layer dynamics farther downstream.

To investigate more deeply these interactions, monitor points were added in the TRPIV window. They are lined up at y/c = -0,03 to sample vertical velocity values near the lower turbulent/non-turbulent interface. Table 6.2 shows the selected coordinates of these points. Their position in relation to vortex dynamics can be seen in Figure 6.15. Spectra of these signals in Figure 6.16 show an important increase of the amplitude of the vertical velocity near the trailing edge, but the PSD is attenuated for monitor points downstream of the trailing edge, including the high frequency region of the power spectra. As seen in section 5.2.3 about HFVTE actuation, flapping increases the vorticity of the shear layers in the trailing edge's area, thus attenuating high energy structures that generate von Kármán vortex street farther downstream.

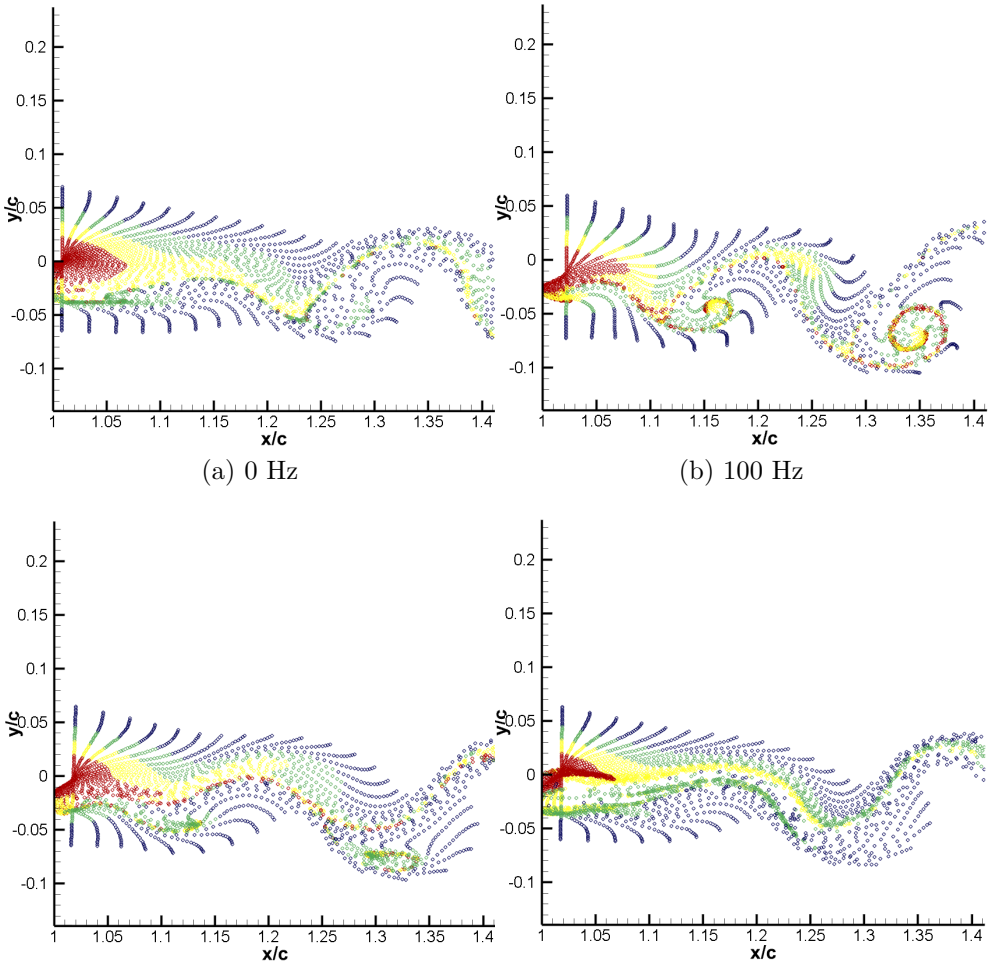

(a) 0 Hz (b) 100 Hz

(c) 170 Hz (d) 300 Hz

Figure 6.14: Streaklines in the case of hybrid morphing at full cambered position. SMA supplied tension of 30 V. Reynolds number of 700,000.

MP	x/c	y/c
1	1,06	-0,03
2	1,20	-0,03
3	1,34	-0,03

Table 6.2: Coordinates of the monitor points.

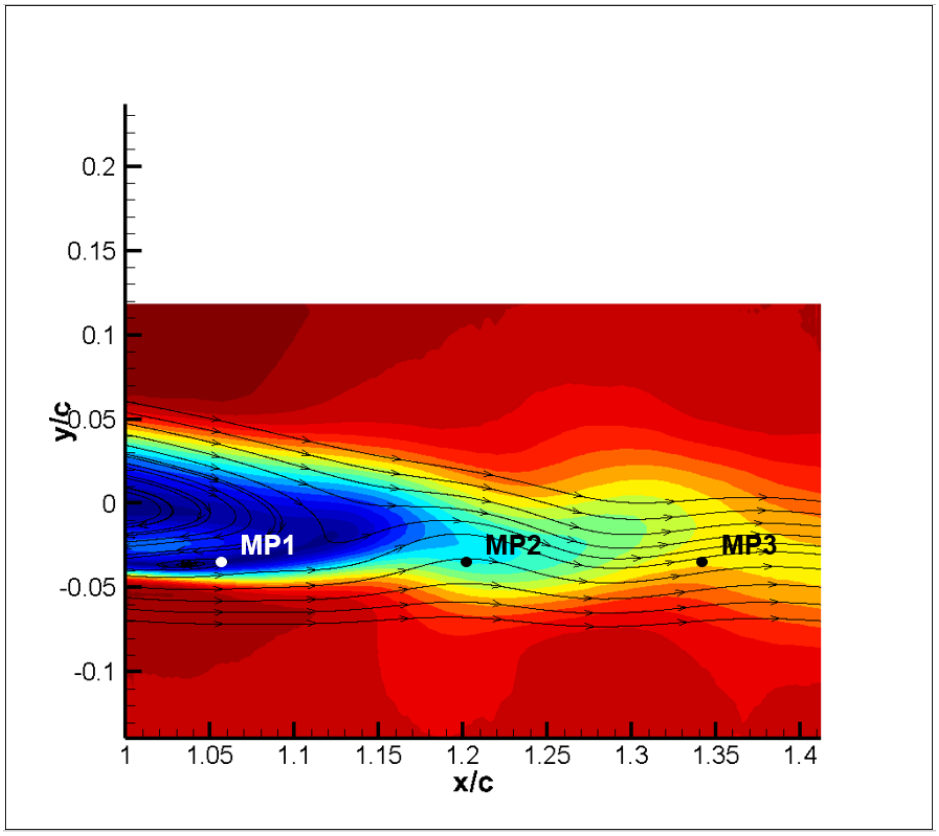

Figure 6.15: Position of the monitor points.

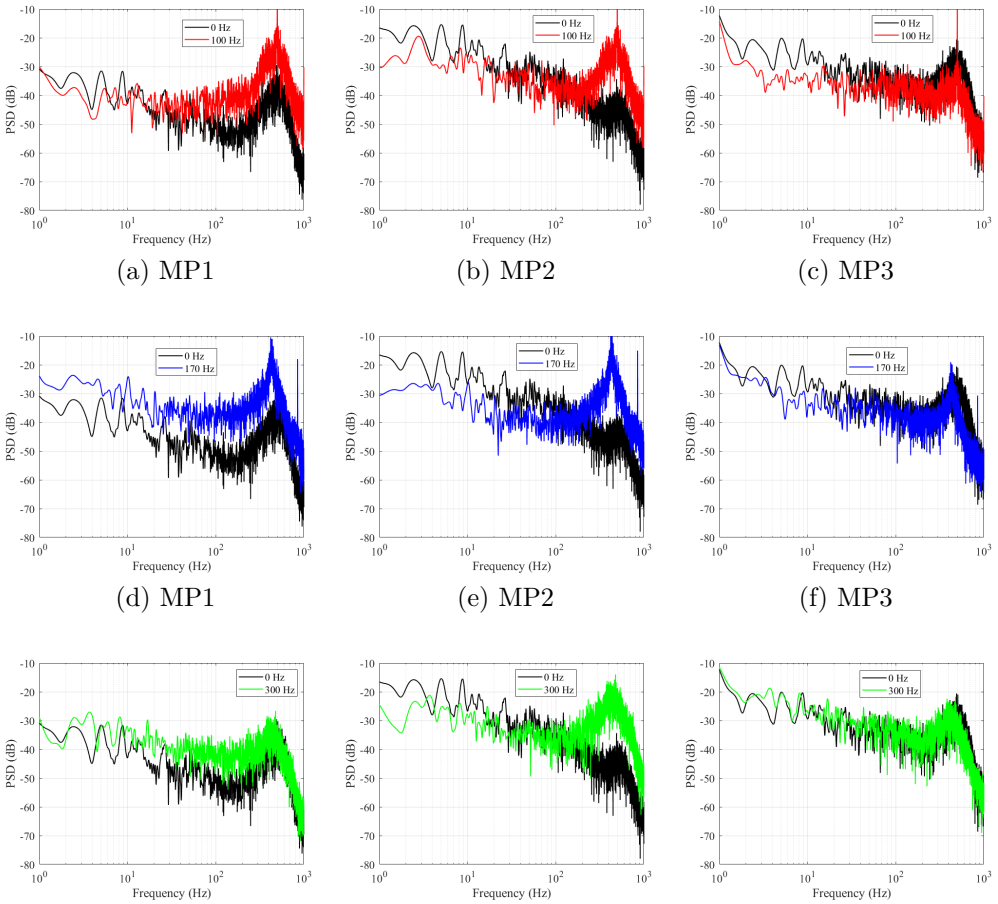

(a) MP1 (b) MP2 (c) MP3

(d) MP1 (e) MP2 (f) MP3

(g) MP1 (h) MP2 (i) MP3

Figure 6.16: Vertical velocity spectra at the corresponding monitor points. Superposition of reference case (only SMA actuation) and hybrid morphing. Re = 700,000 and angle of attack of 10°.

Numerical simulations carried out by the SMS project team have shown consistent results with those obtained in the experimental campaign [51]. The simulations at Reynolds number of 1M have used the prototype dimensions and angle of attack of 10°, as in the experiments. Hybrid morphing was tested with monochromatic piezoelectric actuation at 300 Hz. Figure 6.17 shows snapshots of the numerical results at simulation time t* = 0,75. The reduction of the shear layer length described previously is also obtained in

the hybrid morphing case.

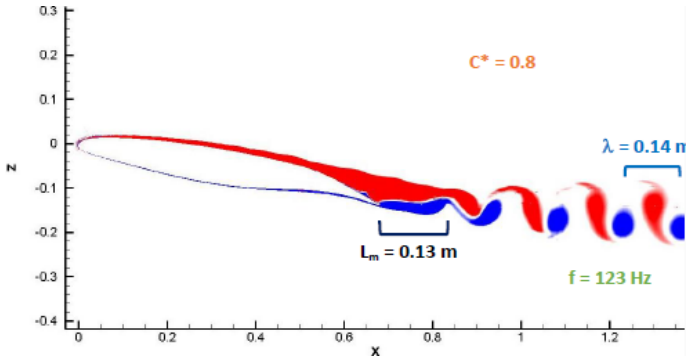

(a) $f_a = 0$ Hz

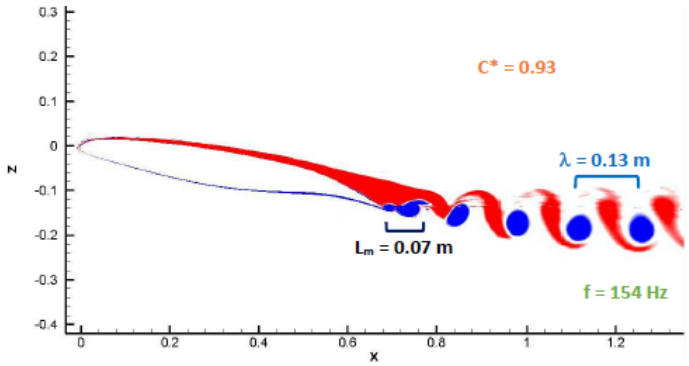

(b) $f_a = 300$ Hz

Figure 6.17: Snapshots of simulation results at t* = 0,75.

6.3 Chapter conclusion

As in the previous section, a complete experimental set-up was employed to study the aerodynamic performance of the hybrid morphing applied on the RS prototype of the SMS project. SMA actuators were supplied at two different electrical tensions to investigate the impact of camber velocity and shape on the lift. Three actuation frequencies were chosen for the HFVTE flapping. Lift increase is seen in all tested cases. Output signals from the balance indicate a better performance at slow cambering. HFVTE actuation at 200 Hz increases lift by more than 1% once SMA are supplied at 30 V

while f_a = 100 Hz is efficient at both camber velocities. f_a = 300 Hz is found to be benefit for lift increase at lower levels, up to 0,71%. For the unsteady pressure measurements, the transient nature of the flow limits the signals duration by the descent's time and turns the spectral analysis more difficult, but attenuation of energy can be seen at low frequency range thanks to hybrid morphing. The modal reduction obtained through the TRPIV shows that the hybrid morphing increases the turbulent activity in the near trailing edge area, but vortex formed farther downstream are attenuated. It has been found that all the actuation frequencies reduce drastically the horizontal velocity values, thus providing less drag than the case with SMA cambering only. This result is consistent with numerical simulations held in conditions similar to the experiments carried out to investigate the hybrid morphing with piezoelectric actuation at 300 Hz. Just like it was presented in the previous chapters, when SMA and piezoelectric actuation were described separately, hybrid morphing also modifies drastically the wake flow dynamics and contributes to a decrease of the velocity deficit thus refraining the drag increase due to the cambering.

Chapter 7

Piezoelectric feedback control

7.1 Fluid-structure interaction

In this chapter the design of an intelligent feedback control system for piezoelectric action is presented. The first sections are devoted to the investigation of the main flow instabilities that interact with the solid structure in the context of a fluid-structure system for which it is intended to decrease the variance thanks to feedback control. A band-pass filter is set for real-time testing. The control system, the selection of its parameters and the efficiency results are presented at the end of the chapter. The work is a collaboration between Toulouse INP (multidisciplinary team IMFT-LAPLACE) and ONERA. The experiments were made in IMFT facilities using the subsonic S4 wind tunnel and the RS, Reduced Scale A320 prototype, of the SMS project designed by LAPLACE while the control laws were developed by the ONERA team.

7.1.1 Experimental set-up

The experimental campaign includes unsteady pressure and acceleration measurements and TRPIV. Three dynamic pressure transducers MEGGITT 8507C-1 are placed at 60%, 80% and 85% of the chord and lined up at 56% of the span as Figure 7.1 shows. The actuation signal is supplied through a dSPACE MicroLabBox, as well as the signal acquisition which is made at a rate of 6 kHz. Signal length is 300 s, more than enough to reach the convergence of mean and RMS values. An accelerometer PCB model 352C33 was positioned at x/c = 0,85, next to the pressure sensor, to investigate the

fluid-structure coupling and especially whether mechanical vibration modifies unsteady pressure values. Sampling and cut-off frequency are $f_a = 6$ kHz and $f_{cut\text{-}off} = 1$ kHz respectively for data acquisition of both pressure and acceleration signals.

TRPIV results were obtained in the same campaign described in the section 4.1 at Reynolds number of 1 million. The main parameters are: sampling frequency $f_s = 5$ kHz, the diameter of the seeding particles is 0,5 µm and PIV investigation window size of 170 per 260 mm.

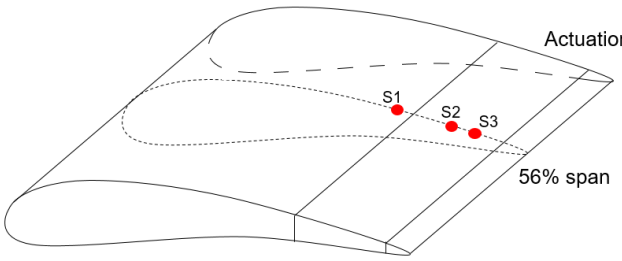

Sensor	x/c
1	0,60
2	0,80
3	0,85

Figure 7.1: Position of pressure transducers.

7.1.2 Unsteady pressure measurements

Pressure measurements were carried out for the design of the feedback control laws of the piezoelectric actuators. In a first step, the cut-off frequencies of the band-pass filter used during the acquisition have been examined. To identify the main coherent structures of the flow, the spectra of the unsteady component of pressure signals were evaluated. Figure 7.2 shows the results for the three pressure sensors. Two regions of interest have been identified: the range between 20 and 100 Hz and the one between 100 and 130 Hz. It is recalled from the numerical simulations [50, 51], that the von Kármán mode is located in the range of 15-35 Hz and the shear layer modes in the range 100-170 Hz.

Figure 7.3 shows the superposition of the outputs from the accelerometer and the pressure sensor located at x/c = 0,85. The frequencies captured by the accelerometer do not correspond to those of the pressure spectra. This result indicates that mechanical vibration induces low interference to the pressure sensors. The frequency range selected for the band-pass filter

is a good choice for the evaluation of the closed-loop control for HFVTE actuation.

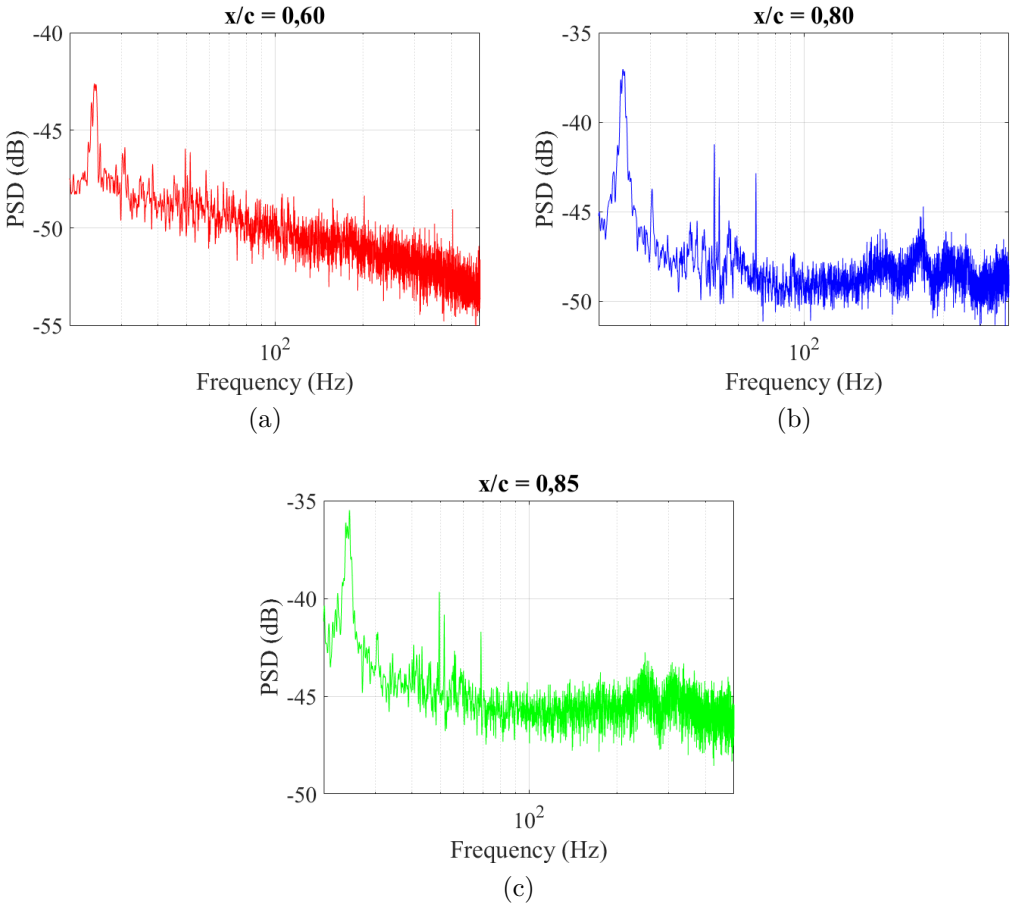

Figure 7.2: Spectra of pressure measurements, Re = 1M, a = 10°.

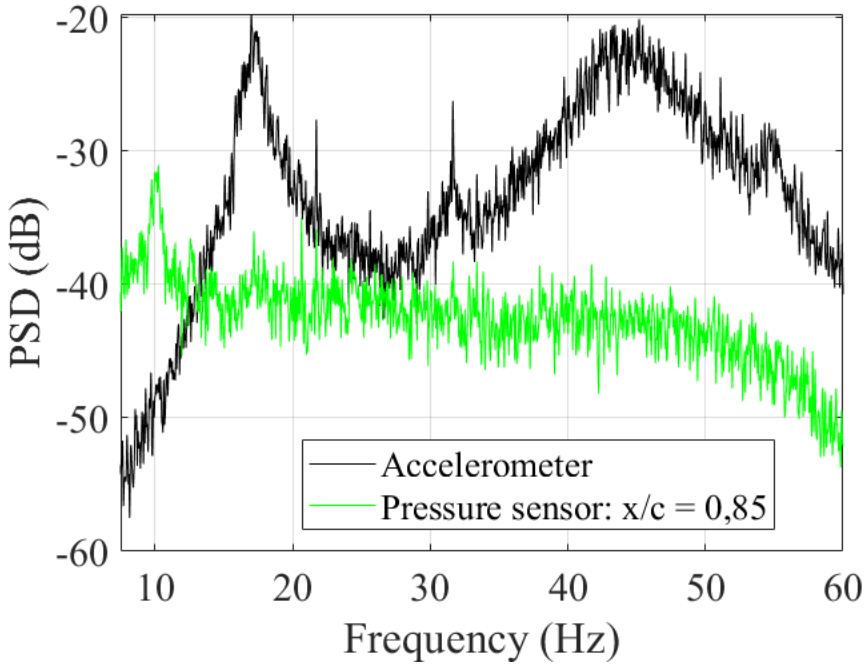

Figure 7.3: Spectra of output signal from accelerometer and pressure sensor.

7.1.3 Time-Resolved Particle Image Velocimetry (TR-PIV): feedback control study

The PIV has been used to investigate the static configuration's natural unsteadiness. In addition to the unsteady pressure measurements, TRPIV results were analyzed to evaluate flow instabilities at Reynolds number of 1 million. The POD was applied to identify the main coherent structures as well as the range of their natural frequency. Figure 7.4 shows the energy distribution of the POD modes. Low order modes were investigated since they are the most energetic ones. The spectra of temporal coefficients can be seen in Figure 7.5. Modes 2, 3 and 4 have their natural frequency below 100 Hz because they represent the von Kármán vortex and are mostly affected by them, unlike mode 5. One can conclude that this mode represents another kind of instability, produced from the VK-Shear layer interaction.

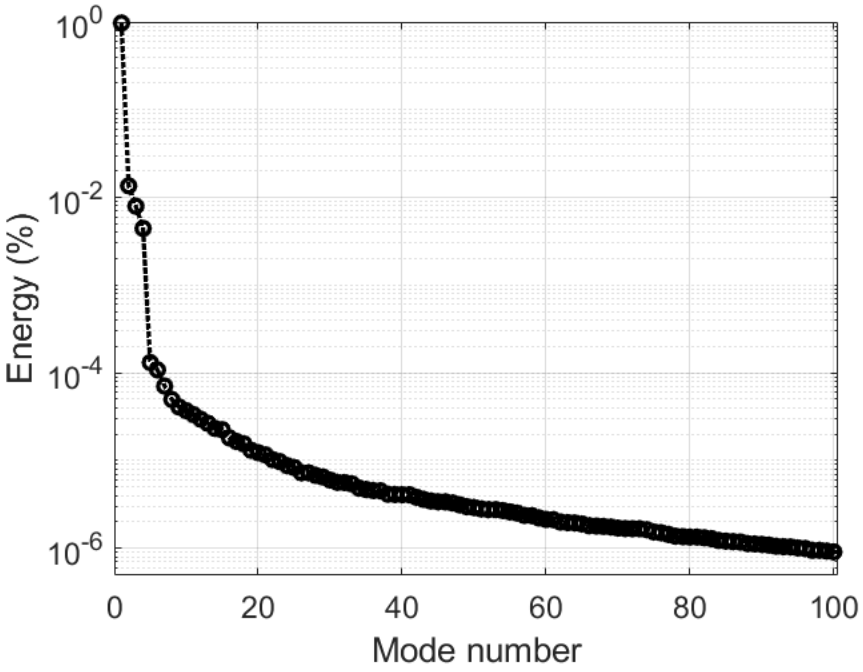

Figure 7.4: Energy distribution of POD modes.

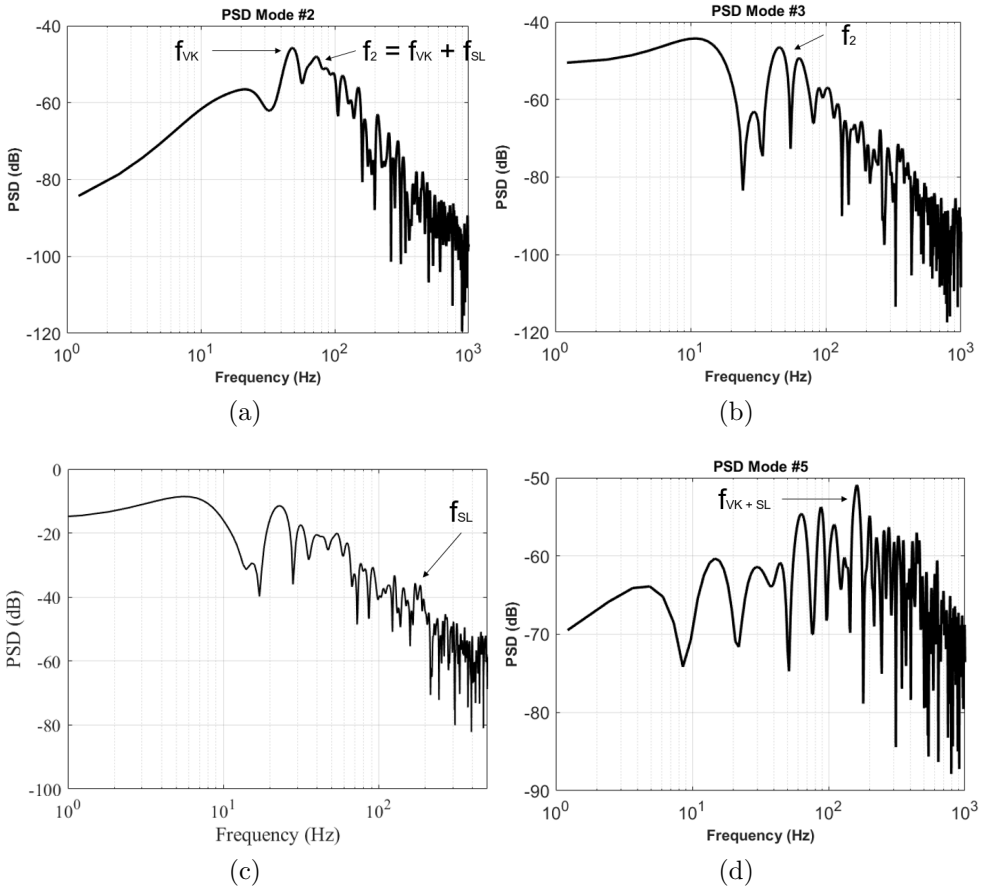

Figure 7.5: Spectra of temporal coefficients.

The next step is to perform on the basis of the TRPIV fields the POD reconstruction of the dynamic system from the low order modes. Monitor points are placed near the trailing edge, where the pressure sensors are located, and farther downstream to investigate the impact of the different classes of vortex. The position of the monitor points is presented in Figure 7.6 and Table 7.1. The spectra of the vertical velocity in Figure 7.7 show similar results among the monitor points, especially MP1 and MP2. Both are located above the flap, in the recirculation zone. MP3 shows the same natural frequencies and in addition the formation of a lower frequency bump corresponding to the first sub-harmonic region of the von Kármán mode as it was also obtained in the SMS project's simulations. MP4 also presents the same kind of lower frequency bump.

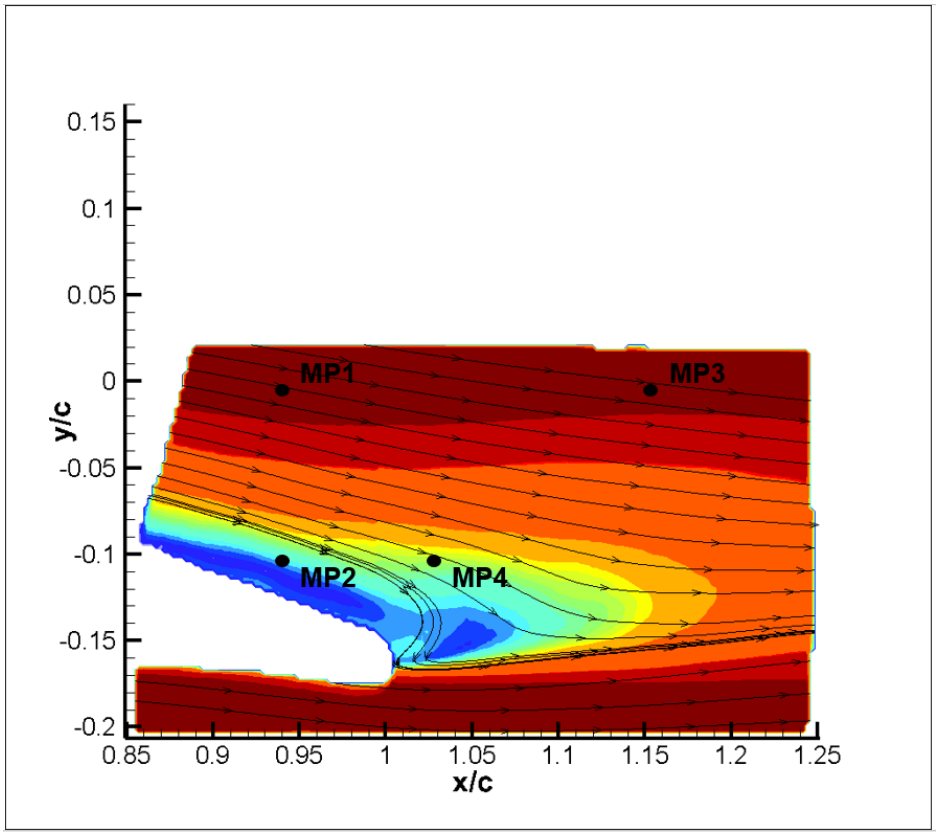

Figure 7.6: Position of monitor points used in flow characterization.

MP	x/c	y/c
1	0,93	0
2	0,93	-0,09
3	1,15	0
4	1,03	-0,09

Table 7.1: Coordinates of monitor points.

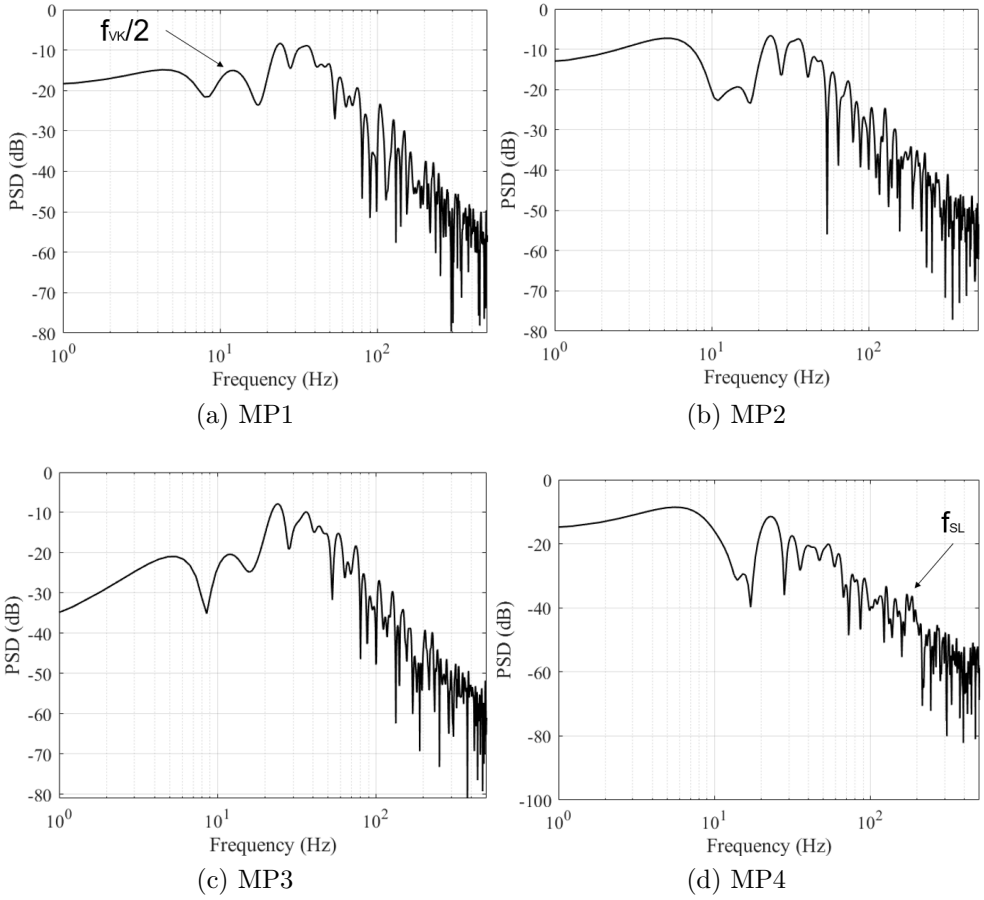

(a) MP1 (b) MP2

(c) MP3 (d) MP4

Figure 7.7: Spectra of V_y from monitor points.

7.2 Closed-loop control design

In collaboration with ONERA - Toulouse DCSD: Cédric Raibaudo, Carsten Döll, P. Mouyon, SMS EU partners, a wind tunnel pressure measurement campaign was conducted to design a closed-loop control system for piezoelectric actuation. For the design of the closed-loop control laws, a reduced dynamic oscillator was chosen to model the behavior of the complete system, which includes the dynamic system under control, the actuators and the sensors. Figure 7.8 shows its principle of operation.

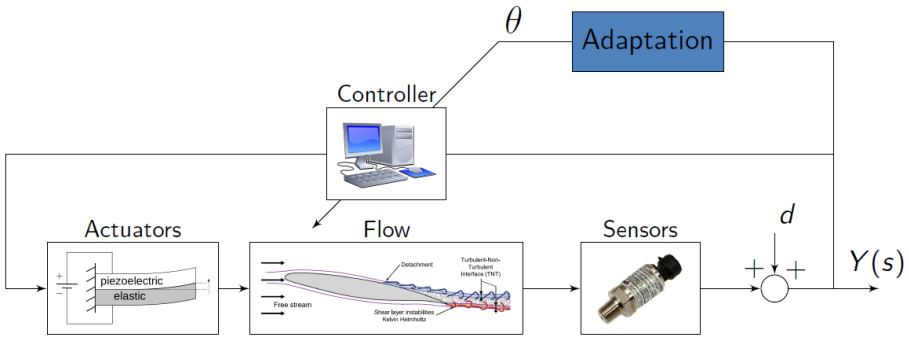

Figure 7.8: Implementation diagram of the closed-loop control system of the piezoelectric actuator.

The model should not be too complex in order to make parameter setting simpler. Nevertheless, it must capture the main characteristics of the phenomenon to be controlled. In this case, the control is intended to reduce the intrinsic vibratory phenomena that are present in the flow. It is then crucial to carefully consider the frequencies of unstable phenomena in the model used for the simulations. Non-linear oscillators such as the Van der Pol oscillator are therefore a satisfactory choice. The Van der Pol non-linear oscillator [56] has been chosen in previous works as being able to represent the stability and dynamics of the flow [57]. This model has been used to reproduce and control the dynamics of simplified thick bodies [13] or aerodynamic streamlined geometries [58], for example. The static gain controller is first considered. This corresponds to the use of a K gain and a τ delay in the output control:

$$u(t) = Ky(t - \tau) \tag{7.1}$$

A cost function J is defined to evaluate the performance of the controller, minimizing here the fluctuations of the oscillator output:

$$J = \sigma_{yy}^2 \tag{7.2}$$

with σ_{yy} the variance of the signals of the three pressure sensors. In order to find optimal values for the model, a generic algorithm technique has been employed. It is based on the evaluation of the cost function for a set of random parameters K and J. Then, by fixing the value of the gain, different values for the delay are tested. Once the cost function reaches a minimum value, the inverse process is made: J is fixed and K varies as illustrated in Figure 7.9. With the optimal parameters found by the experiments, the cost function is reduced on average by -6,5%, and at most by -10,5%. An approach similar to a gradient descent algorithm was also tested (Figure 7.10). The results show a convergence of the optimal parameters to a value similar to the results obtained with the previous approach. The reduction of the cost function reaches -4,4%, which is consistent with the scanning technique.

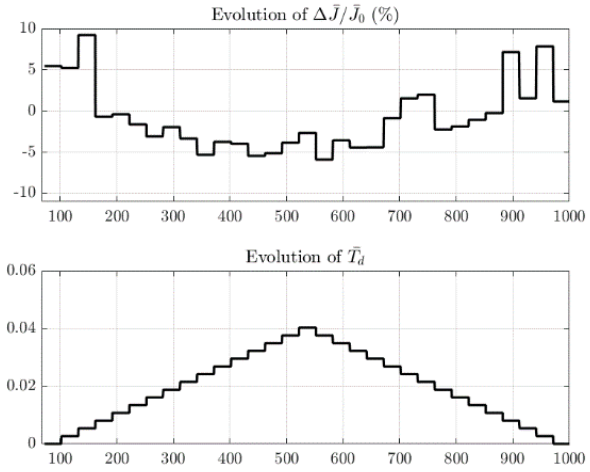

(a) Scan of delay τ, with K = 1,33.

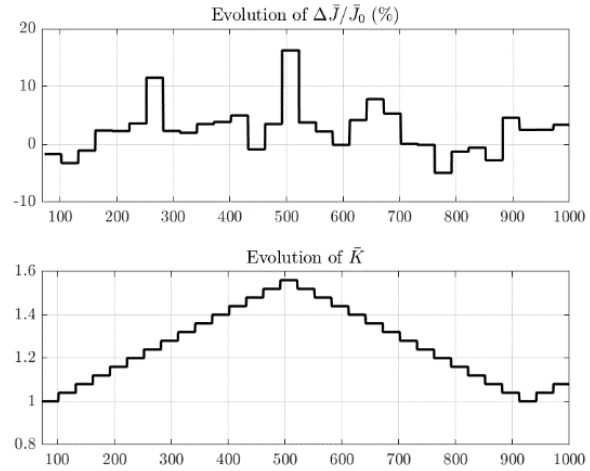

(b) Scan of gain K, with τ= 0,04 s.

Figure 7.9: Evolution of the cost function benefit (top) and adapted parameter (bottom).

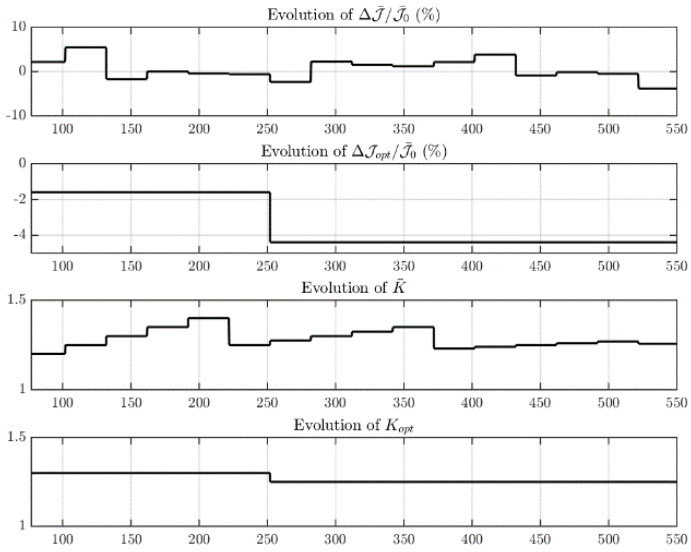

Figure 7.10: Adaptation of the gain using a gradient descent approach.

7.3 Chapter conclusion

To obtain an efficient closed-loop control system, a reduced region of the spectrum of the pressure measurements had to be the focus regarding the experimental campaign. This study identified the main natural instabilities governing the fluid-structure system. The optimality for the design of the close-loop has been based on the variance reduction of the pressure signals, investigated through spectral analysis. Unsteady pressure measurements were made using three pressure transducers placed on the flap and POD reconstruction based on the first five most energetic modes has been considered from the TRPIV results. The spectral analysis of pressure signals have identified two main regions of interest and the TRPIV has shown that the predominant frequency peaks of the natural unsteadiness due to the surrounding turbulence of the A320 morphing wing and its wake are concentrated in the low frequency range of the power spectra, around 10 to 200 Hz.

For the closed-loop control, van der Pol oscillator has been chosen as reduced order model. Different strategies were employed to set the best values

of gain and delay to the model including generic algorithms and gradient-descent optimisation. The cost function was defined as the sum of the three signals variance, since the goal is to enhance the stability of the aerodynamic forces, directly linked to the pressure variations. furthermore, it is worth mentioning that in real flight, only fluctuating pressure measurements can be available in real time in the embedded system of sensing and morphing (and not an aerodynamic balance). Both methods haven proven themselves to be effective in the stabilization of pressure output signals. The reduction of the cost function reaches an average in the order of -6,5% with generic algorithms and -4,4% with the gradient approach. This work shows that it is possible to design an intelligent feedback control system using a network of pressure sensors. This development allows the actuators to adapt themselves to the different flight conditions.

Chapter 8

Conclusion

It is well known a priority for the future aeronautics design fixed by the related industry and by the European Commission (cf. programme of Clean-sky 3), is to optimise the aerodynamic performances, reduce the noise sources and the CO_2 and NO_x emissions in all flight phases. In this context has been inscribed the present thesis under the H2020 N° 723402 research project SMS, "Smart Morphing & Sensing for aeronautical configurations", `http://www.smartwing.org/SMS/EU` coordinated by Toulouse INP, under the multidisciplinary research team of the two Laboratories IMFT and LAPLACE.

In the present thesis, the aerodynamic performance of the so-called "Reduced Scale (RS) morphing A320 prototype of the SMS project of chord 70 cm and span 59 cm has been consider regarding the effect of two different classes of electroactive devices, embedded under the "skin" of the lifting structure and operating at different time and length scales, as dictated by the nature of the turbulence spectrum. Therefore, by means of these actuators, it has been possible to manipulate selected turbulence vortex surrounding the wing by enhancing the beneficial ones and attenuating/suppressing through suitable vortex breakdown the harmful ones. Shape Memory Alloys have been implemented in the prototype's embedded system, able to produce a high deformation (more than 12% of the chord's length) in low frequency (order of 1 Hz). This actuation is inspired from the cambering of the large wings of big hunting birds and leads to lift increase, especially in regimes of low speed as the take-off/landing. The second kind of morphing devices embedded near the trailing edge region of the RS A320 prototype are small piezoactuators of MFC type (Macro-Fiber Composites), with active length of 35 mm, able to produce higher frequency vibrations in small deformations up

to 2 mm. The present thesis analysed how the piezoelectric MFC embedded in the trailing edge produce smaller-scale vortex that interact with the natural shear layer instabilities and related Kelvin-Helmholtz and von Kármán vortex by producing a beneficial "eddy blocking effect". This is able to attenuate the strength of the coherent vortex structures in the shear layers and farther downstream in the wake and to reduce the amplitude of the related frequency peaks in the energy spectra. This actuation concept corresponds to the motion of ailerons and feathers of the large span of bird wings able to respond to the aerodynamic pressure and to produce suitable small deformations and vibrations. Therefore, the electroactive morphing investigated in the present thesis is partly bio-inspired in the context of "Smart wing design through Turbulence control - Science imitating Nature", developed by the carried out in multidisciplinary research team IMFT-LAPLACE during the last decade.

To evaluate the performance of morphing, a complete experimental set-up as well as a structured methodology for post-processing was developed. Dynamic unsteady pressure transducers were used to sample pressure fluctuations on the prototype surface at elevated frequency of acquisition. For lift measurements a home-made aerodynamic balance was designed and manufactured in collaboration with the IMFT support team Signaux & Images. Time Resolved Particle Image Velocimetry campaigns at different Reynolds numbers have been conducted to investigate both types of actuation separately as well as in simultaneous association, in the context of the so-called *hybrid electroactive morphing* derived by the IMFT-LAPLACE team. To examine the large experimental database produced an extensive range of mathematical tools was used such as statistical calculation, cross-correlation, spectral analysis and Proper Orthogonal Decomposition (POD). In addition, Time-Resolved 4D Tomo-PIV has been accomplished for the HFVTE and hybrid morphing cases but these quite recent results have not yet been available in a complete post-treatment.

The experiments have been conducted in the S4 wind tunnel of IMFT with the RS prototype at 10° of reference angle of incidence, corresponding to one of the typical angles communicated by AIRBUS - ETCT (Emerging Technologies and Concepts Toulouse, endorser of the SMS project and at Reynolds numbers in the range 700,000 to 1 Million. POD reconstruction by using a reduced order of modes from the TRPIV results has contributed to analyse the coherent vortex and their frequency modification thanks to the morphing in all cases, HFVTE, cambering and hybrid morphing. The

analysis in case the of slow cambering in high deformations obtained through the SMA actuation has shown the development of the high-energy large coherent von Kármán vortex contributing to the lift, as well as their interaction with the smaller scale Kelvin-Helmholtz eddies developed in the shear layers past the separation points. High energy vortex are created due to increase of low pressure zone above the flap. The present thesis analysed in detail the effects of the higher frequency flapping (HFVTE) as stand alone morphing and also in association with the cambering. It has been shown that HFVTE is able to reduce the recirculation zone, to lead to shear-layer thinning and to produce a considerable reduction of the velocity deficit. These elements contribute to reduce the drag induced from the wake and thus to refrain the augmentation of drag occurred by the increase of cambering because of the more bluff form of the wing's shape. It is noticeable that the current conventional designs produce an effect of cambering by the high-lift non-deformable system of the wing/high-lift flap configuration but this unavoidably increases the drag with downgraded L/D performance. The present morphing is able to produce a high L/D thanks to the wake's drag reduction and simultaneously reduce the noise sources associated to sharp frequency peaks or bumps in the spectra, due to the coherent structures. Moreover, the HFVTE flapping has been proven able to reduce the variance in real time (and therefore the RMS of the aerodynamic pressure, thus leading to a more stable design and increased robustness during flight. These elements have been obtained through feedback control of the dynamic fluid-structure interaction system. High frequency flapping of the trailing edge acts on a larger range of coherent structures. In addition to modifying those responsible for von Kármán instabilities, the piezoelectric actuation is able to manipulate the shear layer vortex along the TNT (Turbulent/Non-Turbulent) interface. The result of these aspects is the reduction of horizontal velocity inside the shear layer and therefore of the velocity deficit, thus reducing the adverse pressure gradient effect around the whole wing and the wake's drag, directly associated to the velocity deficit. Flapping can induce resonance phenomena, but also break down turbulence into smaller vortex. By looking at the power spectra we can see reduction of energy at the natural frequency of the flow instabilities. Force measurements in the wind-tunnel have shown that hybrid morphing reinforces those vortex contributing to the circulation around the wing and therefore leading to the lift increase. The gain reaches +1% in the case of HFVTE actuation combined with camber control. In addition, the network of pressure sensors was used to implement the feedback control system for

piezoelectric actuation. The closed-loop has proven itself to reduce the variance of pressure outputs signals by -5% in average in real time. In a nutshell, the following experimental results can be listed:

- **SMA actuation**: TRPIV allows us to understand the mechanism that generates lift increase. POD analysis highlights the formation of high energy structures as a recirculation zone is created above the flap.
- **HFVTE**: Trailing edge flapping reduces the velocity deficit and the width of the wake. Actuation frequency in the range of 100 Hz decreases by 20% the horizontal velocity comparing to the non morphing case. Noise sources amplitude in dB is reduced by 8%.
- **Hybrid morphing**: Lift increase is seen in all tested cases. Force measurements indicate lift augmentation by 1,66% once SMA are supplied with 30 V and HFVTE is actuated at $f_a = 100$ Hz. $f_a = 200$ Hz and $f_a = 300$ Hz also present higher values of lift if compared to simple cambering: +1% and +0,7% respectively.

The Electroactive morphing research axis has been the focus of a partnership between IMFT and LAPLACE laboratories for more than 10 years in various research projects: EMMAV - Electroactive Morphing for Micro-airvehicles 2010-2012, DYNAMORPH (Dynamic regimes electroactive Morphing 2013-2015, SMARTWING, 2014-2016 funded by the STAE Foundation "Sciences et Technologies pour *l'Aéronautique et l'Espace - Réseau Thématique de Recherche Avancée (RTRA)*, `http://www.fondation-stae.net` as well as two collborative project with AIRBUS "Emerging Technologies and Concepts Toulouse", ETCT, concerning the morphing of the A320 high lift flap in near-scale 1:1, as well as a last project MINOTOR for the morphing of a very large drone's high-lift flaps for real free flight testing (2020-2021). The IMFT-LAPLACE team has lead the H2020 N°723402 Collaborative project SMS, `www.smartwing.org.SMS/EU` involving 10 European partners and three prototypes, the RS, the LS (Large Scale wing/high-lift flap), both for the flight phases of take-off and landing (low subsonic), as well as the tRS, the transonic Reduced Scale prototype for the cruise speeds. In the context of this project, High-Fidelity experiments and numerical simulations have been performed showing considerable aerodynamic performance increase in all flight phases. The study of the present thesis is part of the efforts within the SMS project and as fruit of the long-term research carried out by the multi-disciplinary

team IMFT-LAPLACE. As an important outlook, it is worth mentioning the study of a multiple degrees of freedom morphing system able to increase furthermore the aerodynamic performances far beyond known limits, thanks to novel actuation shells, able to deform and vibrate in multiple frequencies and shapes, partly bio-inspired strongly involving AI (Artificial Intelligence) approaches and to contribute to a new science and technology development, "Bio-Aeronautics", in interaction with AIRBUS.

Chapter 9

Outlook opened by the thesis results

Even with the end of the PhD, more experiments are planned to continue the study of morphing. Over the last years some attempts have been carried out to set-up a Tomographic PIV campaign in IMFT with the purpose of capturing the three-dimensional time-space modification of the coherent vortex structures and of the finer-scale turbulence due to the morphing. Four high-speed cameras have been used in the experimental set-up as seen in Figure 9.1. A considerable effort has been devoted to obtain an investigation 3D volume by reflecting the laser vertically to increase its width. The large data base of more than 4 To obtained at the end of May 2021 is under post-processing.

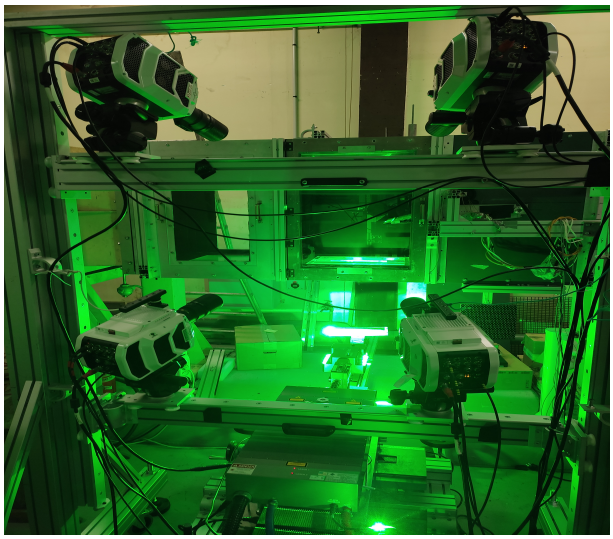

Figure 9.1: 4D Tomo-PIV experimental set-up for the measurements at 500,000 Reynolds number carried out in May 2021, around the morphing RS A320 prototype of the SMS project. S4 wind tunnel of IMFT with contribution of S. Cazin and M. Marchall - *Signaux & Images* service of IMFT. Laser and cameras put at the disposal of the experiments by the Fermat platform. `https://www.federation-fermat.fr/`.

This present study contributes to enrich this cooperation by providing promising results that push forward new advances in the morphing of aircraft structures. The accumulated know-how acquired over all these years allows us to envisage the application of the morphing concepts in different domains such as the shipping and automotive industries. As a perspective, machine learning techniques can be applied to post-process data and then achieve optimal performance of the actuators, Hornik and Baldi explains the wide applicability of these techniques and the back propagation learning method [59, 60]. Grant, for example, uses multi-layer neural networks to analyse PIV images [61]. Neural Networks are also used for simulations of near wall turbulent flow in the work of Milano and Koumoutsakos [62].

The bio-inspiration is an important source to enhance the performance of our means of transportation. It helps us to approach the efficiency of biological mechanisms developed in the course of millions of years of evolution. Once more the nature proves itself to be a reliable source of answers for nowadays technological challenges.

9.1 Published papers

In the context of this PhD thesis the following articles were published in the AIAA journal (American Institute of Aeronautics and Astronautics) of 2019 and in the Proceedings edited by Springer of the FSSIC symposium (Fluid-Structure-Sound Interactions and Control) held in Crete 2019:

- Carvalho, Mateus, et al. "Experimental study of electroactive morphing effects in the aerodynamic performance of a cambered A320 wing by means of time-resolved PIV." AIAA Aviation 2019 Forum. 2019. https://arc.aiaa.org/doi/pdf/10.2514/6.2019-2910.
- Carvalho, Mateus, et al. "Dynamics of a Cambered A320 Wing by Means of SMA Morphing and Time-Resolved PIV at High Reynolds Number." Fluid-Structure-Sound Interactions and Control: Proceedings of the 5th Symposium on Fluid-Structure-Sound Interactions and Control. Springer Nature, pages 283-284.https:/doi.org/10.1007/978-981-33-4960-5_44.

The list also includes an article under preparation about the special session STS17 of the WCCM-ECCOMAS 2020 dedicated to the SMS poject:

- A.Marouf, N.Simiriotis, J.B. Tô, M. Carvalho, Y. Bmegaptche, A. Kitouni, Y.Hoarau, J.F. Rouchon, M.Braza. "Smart Morphing and Sensing for the Wings of the Future". WCCM-ECCOMAS 2020.

Two other papers are in preparation for the Journal of Fluids and Structures:

- M. Carvalho, C. Rouaix, C. Jiimenez-Navarro, A. Marouf, J.B. Tô, C. Raibaudo, C. Döll, P. Mouyon, J.F. Rouchon, H. Hangan, M. Braza, "Electroactive morphing effects through trailing-edge actuation with frequency vobulation applied to an A320 type wing at high Reynolds number", in submition to the Journal of Fluids & Structures, July 2021.
- C. Raibaudo, M. Carvalho, C. Döll, P. Mouyon, J.F. Rouchon, M. Braza. "Aerodynamic performance increase of a morphing A320 ype wing through feedback control at high Reynolds Number", under submission in the Journal of Fluids and Structures, July 2021.

Appendices

Appendix A

Magnetic circuit design

We assume a ferromagnetic circuit, of section S, considered as perfect. On the circuit we place a coil of copper wire of N turns through which an electric current noted I flows. The latter generates the magnetic field lines, we find the magnitude of the field using Ampere's law on the mean contour by assuming that at any point the vectors $\vec{H}$ and $\vec{dl}$ are collinear so:

$$\oint Hdl = NI \tag{A.1}$$

We denote the magnetic induction $\vec{B}$ in Tesla, where μ_0 is the permeability of vacuum and μ_R is the relative permeability of the ferromagnetic circuit. We can then express Ampere's law as:

$$B = \mu_0 \mu_R H \tag{A.2}$$

$$\oint \frac{B}{\mu_0 \mu_R} = NI \tag{A.3}$$

It is still possible to write the theorem in terms of the magnetic flux Φ, in Weber, which passes through the section S of the circuit:

$$\Phi = BS \tag{A.4}$$

$$\oint \frac{\Phi}{\mu_0 \mu_R S} = NI \tag{A.5}$$

The flux is conservative throughout the circuit, so we can remove it from the integral. We define the reluctance of the magnetic circuit in AWb^{-1} or H^{-1}:

$$R = \oint \frac{dl}{\mu_0 \mu_R S} \tag{A.6}$$

We also define the magneto-motive force ε in Ampere turns:

$$\varepsilon = NI = R\Phi \tag{A.7}$$

It is possible to model the magnetic circuit as the following diagram in Figure A.1.

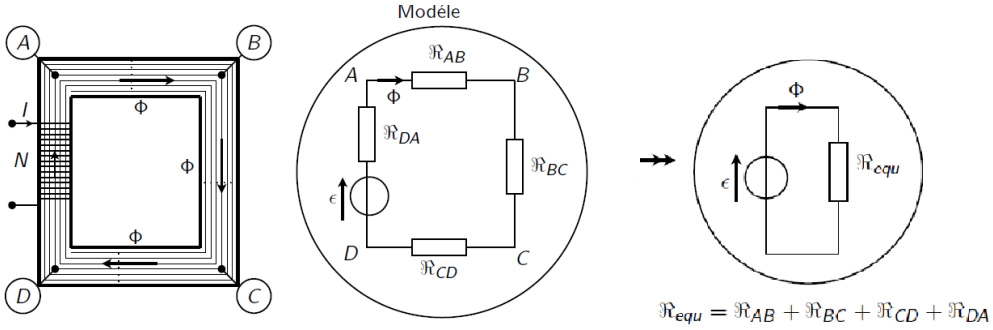

Figure A.1: Magnetic circuit model [63].

Normally this approach found in Ref. [63] is used for closed circuit design and the manufacture of transformers. Our case is different, we must create a gap along the circuit to place the MSMA. We must therefore add the reluctance of this gap to calculate the total reluctance of the magnetic circuit.

For the calculations, the circuit cross-section was defined as $S = 0.00154m^2$, slightly larger than the area of the sample where the field is applied. The gap where the sample is placed is equal to $4.5mm$. This dimension should be as small as possible, because the reluctance of air is much higher than that of ferromagnetic materials. The maximum magnitude of the magnetic field was set as $H = 900kA.m^{-1}$, large enough to saturate the MSMA, but not capable of saturating the magnetic circuit.

According to Equation A.7 we can obtain the magnetomotive force necessary to generate the desired magnetic field along the gap. With this result it is possible to adjust the values of the electric current and the number of

turns. In order to estimate the dimensions of the circuit, we use a current density in the conductor $J = 6A.mm^{-2}$ and a filling coefficient $\alpha = 0.6$ to find the cross section of the coil.

$$S_{coil} = \frac{NI}{\alpha J} \tag{A.8}$$

Finally, after the calculations, we can proceed to the realization of the circuit. As previously mentioned, the dimensions have been chosen in order to reduce the reluctance of the circuit and to respect the assumptions made during the calculations.

Imposed flow approach	
Magnetic Field	$9 \times 10^5 A.m^{-1}$
Circuit section	$0.00161m^2$
Vacuum permeability	$1.26 \times 10^{-6} H.m^{-1}$
Gap length	$7.5mm$
Filling coefficient	0.6
Electric current density	$6A.mm^{-2}$
Magnetic flow	$0.001819Wb$
Ampère turns NI	6750
Coil section	$1875mm^2$
Copper section inside coil	$1125mm^2$
Electric current	$8A$
Number of turns	140
Diameter of copper wire	$1.30mm$

Table A.1: Magnetic circuit properties.

Appendix B

MSMA properties

Properties of $Ni_{50}Mn_{28}Ga_{22}$ alloy (atomic %) provided by Goodfellow Cambridge Limited.

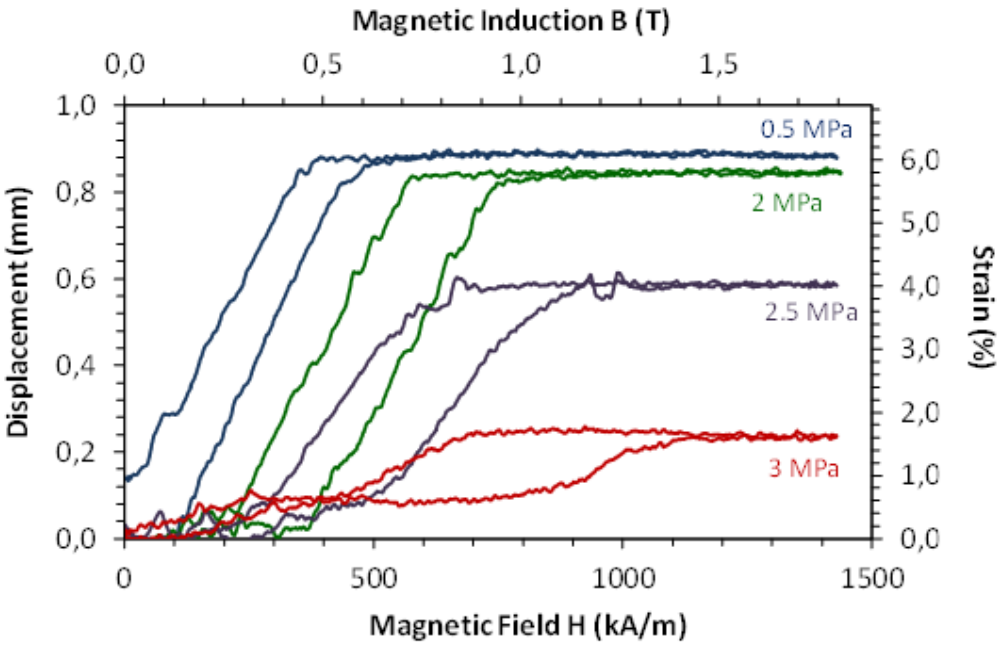

Figure B.1: Magnetization curve of MSMA sample.

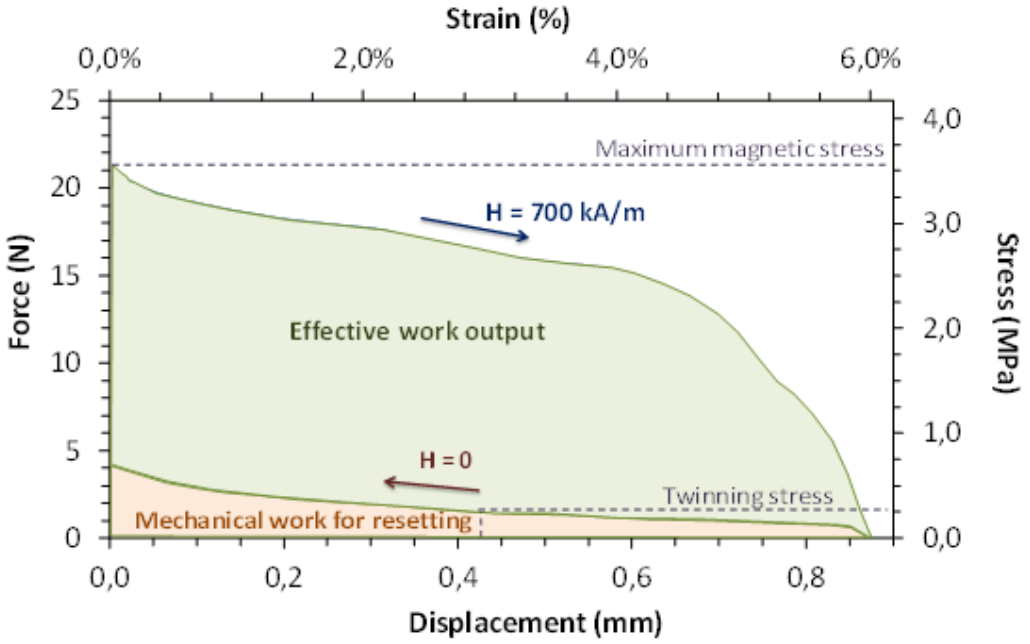

Figure B.2: Stress x Strain curve of MSMA sample.

Physical Properties	
Density	$8g.cm^{-3}$
Melting point	$1130°C$
Thermal Properties	
Crystallization point	$1090°C$
Coefficient of thermal expansion	$20 \times 10^{-6}K^{-1}(@20 - 100°C)$
Thermal diffusivity	$4.4mm^2s^{-1}(@22°C)$
Thermal conductivity	$16W.K^{-1}m^{-1}(@22°C)$
Maximum operating temperature	$45°C$
Temperature – Austenite transformation	$50°C$
Temperature – Martensite transformation	$45°C$
Electrical Properties	
Electrical resistivity	$70\mu\Omega.cm$
Temperature coefficient	$0.003K^{-1}$
Mechanical Properties	
Modulus of elasticity	$8 - 20GPa$
Hardness - Vickers	130
Compression stress	$> 700MPa$
Magnetic Properties	
Curie point	$97 - 105°C$
Initial permeability (hard axis)	2
Maximum permeability (easy axis)	90
Coercivity, Hc	$4000A.m^{-1}$
Activation field strength	$150kA.m^{-1}$
Saturation flux density	$0.6T$
Remanence from saturation	$0.02T$

Table B.1: MSMA sample properties.

Bibliography

[1] W. Nachtigall. Wind Tunnel Measurements of Long-Time Flights in Relation to the Energetics and Water Economy of Migrating Birds. In Eberhard Gwinner, editor, *Bird Migration*, pages 319–327, Berlin, Heidelberg, 1990. Springer.

[2] J. M. V. Rayner. The Mechanics of Flight and Bird Migration Performance. In Eberhard Gwinner, editor, *Bird Migration*, pages 283–299, Berlin, Heidelberg, 1990. Springer.

[3] B. W. Tobalske. Biomechanics of bird flight. *Journal of Experimental Biology*, 210(18):3135–3146, September 2007.

[4] P. J. Butler and A. J. Woakes. The Physiology of Bird Flight. In Eberhard Gwinner, editor, *Bird Migration*, pages 300–318, Berlin, Heidelberg, 1990. Springer.

[5] Ennes Sarradj, Christoph Fritzsche, and Thomas Geyer. Silent Owl Flight: Bird Flyover Noise Measurements. *AIAA Journal*, 49(4):769–779, April 2011.

[6] Florian T. Muijres, L. Christoffer Johansson, Melissa S. Bowlin, York Winter, and Anders Hedenström. Comparing Aerodynamic Efficiency in Birds and Bats Suggests Better Flight Performance in Birds. *PLOS ONE*, 7(5):e37335, May 2012.

[7] J. C. Liao. Fish Exploiting Vortices Decrease Muscle Activity. *Science*, 302(5650):1566–1569, November 2003.

[8] D S Miklosovic, M M Murray, L E Howle, and F E Fish. Leading-edge tubercles delay stall on humpback whale (Megaptera novaeangliae) flippers. *Phys. Fluids*, 16(5):5, 2004.

[9] H. Johari, C. Henoch, D. Custodio, and A. Levshin. Effects of Leading-Edge Protuberances on Airfoil Performance. *AIAA Journal*, May 2012.

[10] Frank E. Fish, Paul W. Weber, Mark M. Murray, and Laurens E. Howle. Marine Applications of the Biomimetic Humpback Whale Flipper. *Marine Technology Society Journal*, 45(4):198–207, July 2011.

[11] Camila Freitas Salgueiredo and Armand Hatchuel. Beyond analogy: A model of bioinspiration for creative design. *Artificial Intelligence for Engineering Design, Analysis and Manufacturing*, 30(2):159–170, May 2016.

[12] J. Sheridan, J. Soria, Wu Jie, and M. C. Welsh. The Kelvin-Helmholtz Instability of the Separated Shear Layer from a Circular Cylinder. In Helmut Eckelmann, J. Michael R. Graham, Patrick Huerre, and Peter A. Monkewitz, editors, *Bluff-Body Wakes, Dynamics and Instabilities*, pages 115–118. Springer Berlin Heidelberg, Berlin, Heidelberg, 1993.

[13] M. Provansal, C. Mathis, and L. Boyer. Bénard-von Kármán instability: transient and forced regimes. *Journal of Fluid Mechanics*, 182:1–22, September 1987.

[14] Rong F. Huang and Chih L. Lin. Vortex shedding and shear-layer instability of wing at low-Reynolds numbers. *AIAA Journal*, May 2012.

[15] G. Martinat, M. Braza, Y. Hoarau, and G. Harran. Turbulence modelling of the flow past a pitching NACA0012 airfoil at and Reynolds numbers. *Journal of Fluids and Structures*, 24(8):1294–1303, November 2008.

[16] Robert H. Liebeck. Design of Subsonic Airfoils for High Lift. *Journal of Aircraft*, May 2012.

[17] Silvestro Barbarino, Onur Bilgen, Rafic M. Ajaj, Michael I. Friswell, and Daniel J. Inman. A Review of Morphing Aircraft. *Journal of Intelligent Material Systems and Structures*, 22(9):823–877, June 2011.

[18] S. Barbarino, E. I. Saavedra Flores, R. M. Ajaj, I. Dayyani, and M. I. Friswell. A review on shape memory alloys with applications to morphing aircraft. *Smart Materials and Structures*, 23(6):063001, April 2014.

[19] Terrence A. Weisshaar. Morphing Aircraft Systems: Historical Perspectives and Future Challenges. *Journal of Aircraft*, 50(2):337–353, March 2013.

[20] D.C. Lagoudas. *Shape Memory Alloys*, volume 1. Springer US, Boston, MA, 2008.

[21] N. Gabdullin and S. H. Khan. Review of properties of magnetic shape memory (MSM) alloys and MSM actuator designs. *Journal of Physics: Conference Series*, 588(1):012052, 2015.

[22] Johannes Scheller. *Electroactive morphing for the aerodynamic performance improvement of next generation airvehicles*. thesis, Toulouse, INPT, October 2015.

[23] Herbert Schmidt. Magneto-Mechanical Energy Conversion in Magnetic Shape Memory Alloys. *Journal of Physics: Conference Series*, 303:012078, July 2011.

[24] Jean-Yves Gauthier, Arnaud Hubert, Joël Abadie, Nicolas Chaillet, and C. Lexcellent. Magnetic shape memory alloy and actuator design. In *Proceedings of the 5th International Workshop on Microfactories, IWMF'06.*, pages sur CD ROM – 4 pages., Besançon, France, October 2006.

[25] B. Krevet and M. Kohl. FEM simulation of a Ni–Mn–Ga film bridge actuator. *Physics Procedia*, 10:154–161, January 2010.

[26] B. Kiefer, H. E. Karaca, D. C. Lagoudas, and I. Karaman. Characterization and modeling of the magnetic field-induced strain and work output in Ni2MnGa magnetic shape memory alloys. *Journal of Magnetism and Magnetic Materials*, 312(1):164–175, May 2007.

[27] B. Kiefer and D.C. Lagoudas. Modeling the Coupled Strain and Magnetization Response of Magnetic Shape Memory Alloys under Magnetomechanical Loading. *Journal of Intelligent Material Systems and Structures*, 20(2):143–170, January 2009.

[28] Michel Brissaud. *Matériaux piézoélectriques: caractérisation, modélisation et vibration*. PPUR presses polytechniques, 2007. Google-Books-ID: wdfUzPJh4aQC.

[29] Rüdiger G. Ballas. *Piezoelectric Multilayer Beam Bending Actuators: Static and Dynamic Behavior and Aspects of Sensor Integration*. Springer Science & Business Media, March 2007. Google-Books-ID: 6kYK0DNW5hMC.

[30] Khaled S. Ramadan, D. Sameoto, and S. Evoy. A review of piezoelectric polymers as functional materials for electromechanical transducers. *Smart Materials and Structures*, 23(3):033001, January 2014.

[31] J. Scheller, M. Chinaud, JF. Rouchon, E. Duhayon, S. Cazin, M. Marchal, and M. Braza. Trailing-edge dynamics of a morphing NACA0012 aileron at high Reynolds number by high-speed PIV. *Journal of Fluids and Structures*, 55:42–51, May 2015.

[32] Johannes Scheller, Karl-Joseph Rizzo, Gurvan Jodin, Eric Duhayon, Jean-Francois Rouchon, and Marianna Braza. A hybrid morphing NACA4412 airfoil concept. In *2015 IEEE International Conference on Industrial Technology (ICIT)*, pages 1974–1978, Seville, March 2015. IEEE.

[33] Christian Lexcellent. *Shape-Memory Alloys Handbook*. John Wiley & Sons, April 2013.

[34] D J Hartl and D C Lagoudas. Aerospace applications of shape memory alloys. *Proceedings of the Institution of Mechanical Engineers, Part G: Journal of Aerospace Engineering*, 221(4):535–552, April 2007.

[35] M. Chinaud, J. F. Rouchon, E. Duhayon, J. Scheller, S. Cazin, M. Marchal, and M. Braza. Trailing-edge dynamics and morphing of a deformable flat plate at high Reynolds number by time-resolved PIV. *Journal of Fluids and Structures*, 47:41–54, May 2014.

[36] Dimitris C. Lagoudas, Zhongue Bo, and Muhammad A. Qidwai. A unifiel thermodynamic constitutive model for SMA and finite element analysis of active metal matrix composites. *Mechanics of Composite Materials and Structures*, April 2007.

[37] L.C. Brinson. One-Dimensional Constitutive Behavior of Shape Memory Alloys: Thermomechanical Derivation with Non-Constant Material Functions and Redefined Martensite Internal Variable. *Journal of Intelligent Material Systems and Structures*, 4(2):229–242, April 1993.

[38] M R Zakerzadeh and H Salehi. Comparative Analysis of Some one-Dimensional SMA Constitutive Models for a Ni-Ti Wire for Shape Control Applications with Experimental Data. page 14.

[39] Gurvan Jodin. *Hybrid electroactive morphing at real scale - application to Airbus A320 wings*. PhD thesis, Toulouse, INPT, 2017.

[40] Gurvan Jodin, Johannes Scheller, Karl Joseph Rizzo, Eric Duhayon, Jean-François Rouchon, and Marianna Braza. Dimensionnement d'une maquette pour l'investigation du morphing électroactif hybride en soufflerie subsonique. In *22e Congrès Français de Mécanique (CFM 2015)*, pages 1–13, Lyon, France, August 2015.

[41] N. Simiriotis, M. Fragiadakis, J. F. Rouchon, and M. Braza. Shape control and design of aeronautical configurations using shape memory alloy actuators. *Computers & Structures*, 244:106434, February 2021.

[42] Jean Hélder Marques Ribeiro and William Roberto Wolf. Identification of coherent structures in the flow past a NACA0012 airfoil via proper orthogonal decomposition. *Physics of Fluids*, 29(8):085104, August 2017.

[43] Serhiy Yarusevych, Pierre E. Sullivan, and John G. Kawall. Coherent structures in an airfoil boundary layer and wake at low Reynolds numbers. *Physics of Fluids*, 18(4):044101, April 2006.

[44] Serhiy Yarusevych, Pierre E. Sullivan, and John G. Kawall. On vortex shedding from an airfoil in low-Reynolds-number flows. *Journal of Fluid Mechanics*, 632:245–271, August 2009.

[45] D. R. Troolin, E. K. Longmire, and W. T. Lai. Time resolved PIV analysis of flow over a NACA 0015 airfoil with Gurney flap. *Experiments in Fluids*, 41(2):241–254, August 2006.

[46] E. Deri, M. Braza, E. Cid, S. Cazin, D. Michaelis, and C. Degouet. Investigation of the three-dimensional turbulent near-wake structure past a flat plate by tomographic PIV at high Reynolds number. *Journal of Fluids and Structures*, 47:21–30, May 2014.

[47] Petre Stoica and Randolph L. Moses. *Spectral analysis of signals*. Pearson/Prentice Hall, Upper Saddle River, N.J, 2005.

[48] Rodolphe Perrin. *Analyse physique et modélisation d'écoulements incompressibles instationnaires turbulents autour d'un cylindre circulaire à grand nombre de Reynolds*. PhD thesis, Toulouse, INPT.

[49] G Berkooz, P Holmes, and J L Lumley. The Proper Orthogonal Decomposition in the Analysis of Turbulent Flows. *Annual Review of Fluid Mechanics*, 25(1):539–575, 1993.

[50] N. Simiriotis, G. Jodin, A. Marouf, P. Elyakime, Y. Hoarau, J. C. R. Hunt, J. F. Rouchon, and M. Braza. Morphing of a supercritical wing by means of trailing edge deformation and vibration at high Reynolds numbers: Experimental and numerical investigation. *Journal of Fluids and Structures*, 91:102676, November 2019.

[51] Abderahmane Marouf. *Analyse physique de concepts du morphing électroactif pour accroître les performances aérodynamiques des ailes du futur par simulation numérique de Haute Fidélité et modélisation de la Turbulence à nombre de Reynolds élevé*. PhD thesis, 2020. Thèse de doctorat dirigée par Hoarau, Yannick et Braza, Marianna, Mécanique Des Fluides, Université de Strasbourg 2020.

[52] Nikolaos Simiriotis. *Numerical study and physical analysis of electroactive morphing wings and hydrodynamic profiles at high Reynolds number turbulent flows*. These de doctorat, Toulouse, INPT, June 2020.

[53] Abderahmane Marouf, Yannick Bmegaptche Tekap, Nikolaos Simiriotis, Jean-Baptiste Tô, Jean-François Rouchon, Yannick Hoarau, and Marianna Braza. Numerical investigation of frequency-amplitude effects of dynamic morphing for a high-lift configuration at high Reynolds number. *International Journal of Numerical Methods for Heat & Fluid Flow*, ahead-of-print(ahead-of-print), January 2019.

[54] G. Jodin, V. Motta, J. Scheller, E. Duhayon, C. Döll, J. F. Rouchon, and M. Braza. Dynamics of a hybrid morphing wing with active open loop vibrating trailing edge by time-resolved PIV and force measures. *Journal of Fluids and Structures*, 74:263–290, October 2017.

[55] Damien Szubert, Fernando Grossi, Antonio Jimenez Garcia, Yannick Hoarau, Julian C. R. Hunt, and Marianna Braza. Shock-vortex shear-layer interaction in the transonic flow around a supercritical airfoil at

high Reynolds number in buffet conditions. *Journal of Fluids and Structures*, 55:276–302, May 2015.

[56] Takashi Kanamaru. Van der pol oscillator. *Scholarpedia*, 2(1):2202, 2007.

[57] Valentina Motta, Philippe Mouyon, and Carsten Döll. Discrete Time Open-Loop and Closed-Loop Flow Control Based on Van der Pol Modeling. In *8th AIAA Flow Control Conference*. American Institute of Aeronautics and Astronautics, 2016.

[58] Muhammad Saif Ullah Khalid, Imran Akhtar, and Naveed Iqbal Durrani. Analysis of Strouhal number based equivalence of pitching and plunging airfoils and wake deflection. *Proceedings of the Institution of Mechanical Engineers, Part G: Journal of Aerospace Engineering*, 229(8):1423–1434, June 2015.

[59] Kurt Hornik, Maxwell Stinchcombe, and Halbert White. Multilayer feedforward networks are universal approximators. *Neural Networks*, 2(5):359–366, January 1989.

[60] Pierre Baldi and Kurt Hornik. Neural networks and principal component analysis: Learning from examples without local minima. *Neural Networks*, 2(1):53–58, January 1989.

[61] I. Grant and X. Pan. An investigation of the performance of multi layer, neural networks applied to the analysis of PIV images. *Experiments in Fluids*, 19(3):159–166, July 1995.

[62] Michele Milano and Petros Koumoutsakos. Neural Network Modeling for Near Wall Turbulent Flow. *Journal of Computational Physics*, 182(1):1–26, October 2002.

[63] A De Carvalho. Module d'Electrotechnique ET2 Circuits magnétiques. page 32, 2010.